1-1-2012

Investigating the Role of Microtubules in Glut4 Vesicle Trafficking and the Kinetics of Membrane Attachment by the Myosin Myo1c

Jennine Dawicki McKenna
University of Pennsylvania, jdawicki@mail.med.upenn.edu

Investigating the Role of Microtubules in Glut4 Vesicle Trafficking and the Kinetics of Membrane Attachment by the Myosin Myo1c

Abstract
The myosin myo1c dynamically localizes to cellular membranes through high affinity phosphoinositide binding and links them to the actin cytoskeleton. Determining the kinetics of membrane attachment will provide insight into the relationship between membrane-attachment and actin-attachment lifetimes, and will also provide details about the regulation of membrane attachment. Stopped-flow spectroscopy was used to measure the binding and dissociation of a recombinant myo1c construct containing the tail and regulatory domains (myo1c$^{IQ\text{-}tail}$) to and from 100 nm diameter large unilamellar vesicles (LUVs). The apparent second-order rate constant for association of myo1c$^{IQ\text{-}tail}$ with LUVs containing 2% phosphatidylinositol 4,5-bisphosphate (PtdIns(4,5)P_2) was approximately diffusion-limited. Myo1c$^{IQ\text{-}tail}$ dissociated from PtdIns(4,5)P_2 at a slower rate (2.0 s^{-1}) than the pleckstrin homology domain of phospholipase C-δ (PLCδ-PH) (13 s^{-1}). The presence of additional anionic phospholipid reduced the myo1c$^{IQ\text{-}tail}$ dissociation rate constant > 50-fold, but marginally changed the dissociation rate of PLCδ-PH, suggesting that additional electrostatic interactions in myo1c$^{IQ\text{-}tail}$ help to stabilize binding. Remarkably, high concentrations of soluble inositol phosphates induce dissociation of myo1c$^{IQ\text{-}tail}$ from LUVs, suggesting that phosphoinositides are able to bind and dissociate from myo1c$^{IQ\text{-}tail}$ as it remains bound to the membrane.

In adipocytes, vesicles containing glucose transporter-4 (GLUT4) redistribute from intracellular stores to the cell periphery in response to insulin. Vesicles then fuse with the plasma membrane, facilitating glucose transport into the cell. To gain insight into the molecular role of microtubules, we examined the spatial organization and dynamics of microtubules in relation to GLUT4 vesicle trafficking in living 3T3-L1 adipocytes using total internal reflection fluorescence (TIRF) microscopy. Insulin stimulated an increase in microtubule density and curvature within the TIRF-illuminated region of the cell. The time course of the density increase precedes that of the increase in intensity of HA-GLUT4-eGFP in this same region. Microtubule disruption delayed and modestly reduced the accumulation of GLUT4 at the plasma membrane. Interestingly, fusion of GLUT4-containing vesicles with the plasma membrane preferentially occur near microtubules, and long-distance vesicle movement along microtubules visible at the cell surface prior to fusion does not appear to account for this proximity. We conclude that microtubules may be important in providing spatial information for fusion events.

Degree Type
Dissertation

Degree Name
Doctor of Philosophy (PhD)

Graduate Group
Cell & Molecular Biology

INVESTIGATING THE ROLE OF MICROTUBULES IN GLUT4 VESICLE TRAFFICKING AND THE KINETICS OF MEMBRANE ATTACHMENT BY THE MYOSIN MYO1C

Jennine M. Dawicki McKenna

A DISSERTATION

in

Cell and Molecular Biology

Presented to the Faculties of the University of Pennsylvania
in Partial Fulfillment of the Requirements for the Degree of Doctor of Philosophy

2012

E. Michael Ostap, Ph.D. Professor of Physiology Supervisor of Dissertation	Daniel S. Kessler, Ph.D. Associate Professor of Cell and Developmental Biology Graduate Group Chairperson

Dissertation Committee
Yale E. Goldman, M.D., Ph.D., Professor of Physiology
Wei Guo, Ph.D., Associate Professor of Biology
Erika L.F. Holzbaur, Ph.D., Professor of Physiology
Paul A. Janmey, Ph.D., Professor of Physiology

ACKNOWLEDGMENTS

It's very appropriate that I should preface this thesis by expressing my gratitude to those who have helped to shape it, or who have helped to shape me. Their support, encouragement, and guidance mean more to me than I let them know or than I can express here.

First, I'd like to thank my advisor, Mike. I have really enjoyed the time that I spent in his lab, with all the ups and downs of research. I value the feedback and encouragement he has given me in my development as a scientist. He made me aware of an undiscovered interest in biochemistry and kinetics, and assured me that it wasn't too late to start exploring them. Mike is an example of how one can successfully integrate a strong commitment to family with a vibrant scientific career, and I very much respect him for that.

I'd also like to thank two additional scientific mentors of mine. Dr. John Tudor was my undergraduate advisor and a large part of the reason I applied to graduate school in the first place. Yale E. Goldman provided me with insight into everything from optics to electronics to data analysis. The time that he sets aside to share his knowledge with others has always impressed me. He remains for me one of the best examples of a person who is simultaneously very remarkable and down-to-earth as well.

Next, I want to recognize how important my family has been to me. I have always been sure of their love and acceptance, regardless of my achievements.

I know that my parents, Francis and Anna, are proud of me, but I want to let them know that I also look up to them. I'm not blind to the sacrifices they've made so that their children could have what they did not. My brother, Andy, my sister, Kathy, and Anna May have been and continue to be a very important part of my life.

So far I've mostly broken down my thanks into my scientific and private life, but this is really a false dichotomy. I want to thank Alli, Ionas, and most recently Jake- co-habitants of our sardine can of an office- who've let me vent so many of my frustrations as well as been among the first to share in my celebrations. They've helped me to laugh and hold on even when I wanted to quit. I value equally what they've taught me about being a scientist and about being a person. In addition, Dave, Joe, John, Tianming, Beth, Michael, Betsy, and Abbey have all made my time in the Ostap lab an enjoyable experience. I want to include Yujie in there, as well.

Last but not least, I must certainly thank my husband, Martin. It would take nearly as many pages of thanks as are in my thesis to do him justice. Suffice it to say, he has been my biggest supporter. And I might as well thank my co-defendant during my thesis, the newest member of our family, Declan Joseph McKenna.

ABSTRACT

INVESTIGATING THE ROLE OF MICROTUBULES IN GLUT4 VESICLE TRAFFICKING

AND

THE KINETICS OF MEMBRANE ATTACHMENT BY THE MYOSIN MYO1C

Jennine M. Dawicki McKenna

Dr. E. Michael Ostap

The myosin myo1c dynamically localizes to cellular membranes through high affinity phosphoinositide binding and links them to the actin cytoskeleton. Determining the kinetics of membrane attachment will provide insight into the relationship between membrane-attachment and actin-attachment lifetimes, and will also provide details about the regulation of membrane attachment. Stopped-flow spectroscopy was used to measure the binding and dissociation of a recombinant myo1c construct containing the tail and regulatory domains (myo1c$^{IQ\text{-}tail}$) to and from 100 nm diameter large unilamellar vesicles (LUVs). The apparent second-order rate constant for association of myo1c$^{IQ\text{-}tail}$ with LUVs containing 2% phosphatidylinositol 4,5-bisphosphate (PtdIns(4,5)P_2) was approximately diffusion-limited. Myo1c$^{IQ\text{-}tail}$ dissociated from PtdIns(4,5)P_2 at a slower rate (2.0 s^{-1}) than the pleckstrin homology domain of phospholipase C-δ (PLCδ-PH) (13 s^{-1}). The presence of additional anionic phospholipid reduced the myo1c$^{IQ\text{-}tail}$ dissociation rate constant > 50-fold, but marginally changed the dissociation rate of

PLCδ-PH, suggesting that additional electrostatic interactions in myo1c$^{IQ\text{-}tail}$ help to stabilize binding. Remarkably, high concentrations of soluble inositol phosphates induce dissociation of myo1c$^{IQ\text{-}tail}$ from LUVs, suggesting that phosphoinositides are able to bind and dissociate from myo1c$^{IQ\text{-}tail}$ as it remains bound to the membrane.

In adipocytes, vesicles containing glucose transporter-4 (GLUT4) redistribute from intracellular stores to the cell periphery in response to insulin. Vesicles then fuse with the plasma membrane, facilitating glucose transport into the cell. To gain insight into the molecular role of microtubules, we examined the spatial organization and dynamics of microtubules in relation to GLUT4 vesicle trafficking in living 3T3-L1 adipocytes using total internal reflection fluorescence (TIRF) microscopy. Insulin stimulated an increase in microtubule density and curvature within the TIRF-illuminated region of the cell. The time course of the density increase precedes that of the increase in intensity of HA-GLUT4-eGFP in this same region. Microtubule disruption delayed and modestly reduced the accumulation of GLUT4 at the plasma membrane. Interestingly, fusion of GLUT4-containing vesicles with the plasma membrane preferentially occur near microtubules, and long-distance vesicle movement along microtubules visible at the cell surface prior to fusion does not appear to account for this proximity. We conclude that microtubules may be important in providing spatial information for fusion events.

TABLE OF CONTENTS

LIST OF TABLES

Chapter 2

Chapter 3

LIST OF FIGURES

Chapter 1

Chapter 2

Chapter 3

LIST OF MOVIES

Chapter 3

Chapter 1. Introduction

1.1 SPECIFIC AIMS

1.1.1 Motivation for Thesis

Molecular motors and the cytoskeletal tracks upon which they move are crucial to cellular function. The cell uses a wide diversity of motors to accomplish tasks ranging from organelle positioning and maintenance of cell shape to membrane rearrangement, motility, and cell division. The vertebrate myosin myo1c is one motor expressed in a wide range of cells (Sherr *et al.*, 1993). Intriguingly, despite the wealth of biochemical information available for myo1c, details of its cellular function remain unknown. The overarching goal of this thesis is to provide needed insight into the molecular role of myo1c in the cell.

1.1.2 Specific Aims

Myo1c is important in several biological processes that require membrane dynamics. For example, myo1c is involved in vesicle trafficking (Bose *et al.*, 2002; Bose *et al.*, 2004), compensatory endocytosis following regulated exocytosis (Sokac *et al.*, 2006), and tensioning of mechano-sensitive ion channels (Holt *et al.*, 2002). However, a molecular understanding of how myo1c functions in these important cell biological processes is missing.

An important recent discovery in the cell biology of myo1c is that it plays a role in the insulin-stimulated trafficking of vesicles containing glucose transporter-4 (GLUT4)

(Bose *et al.*, 2002; Bose *et al.*, 2004). Glucose entry into adipose and muscle tissue requires glucose transporters and is limited by the amount of these proteins in the plasma membrane (Suzuki and Kono, 1980; Cushman and Wardzala, 1980). The major insulin-responsive transporter in these cell types is GLUT4 (James *et al.*, 1988; James *et al.*, 1989). Under basal conditions, the majority of GLUT4 is sequestered within an insulin-sensitive storage compartment in adipose cells. Insulin binding to the insulin receptor initiates a signaling cascade involving the activation of phosphatidylinositol-3-kinase (PI3K) and the serine/threonine kinase Akt (reviewed in (Hou and Pessin, 2007)), resulting in a net increase of GLUT4 at the plasma membrane. Insulin-stimulated GLUT4 trafficking is largely responsible for removal of glucose from circulating blood after a meal and is crucial for glucose homeostasis.

It has been demonstrated in adipocytes that siRNA-mediated knock-down of myo1c inhibits the final steps of GLUT4 translocation to and/or fusion with the plasma membrane, and myo1c over-expression can overcome blockage of vesicle fusion brought about through PI3K inhibition (Bose *et al.*, 2002; Bose *et al.*, 2004). While such experiments establish a role for myo1c at some stage of vesicle delivery or fusion, the details of myo1c involvement are lacking.

In the context of GLUT4 vesicle trafficking in response to insulin, there are several potential models for the involvement of myo1c that are consistent with experimental observations in cells. These include (Figure 1.1):

1. Myo1c is involved in short-range transport of vesicles to the plasma membrane.

2. Myo1c transports GLUT4 membranes that have not formed discrete vesicles. In this case, transport pulls tubulo-vesicular structures into the actin-rich cell cortex.

3. Myo1c anchors vesicles to actin filaments. In this model, the motor activity of myo1c is important not so much for transport but for dynamic tethering of the vesicles. Such anchoring could inhibit microtubule-based motors from translocating vesicles that are already near the cell surface.

4. The interaction of myo1c with GLUT4 vesicles is secondary to its interaction with the plasma membrane and actin to facilitate GLUT4 tethering or fusion. As an example, myo1c could affect the local tension of the plasma membrane through its interaction with actin.

Specific Aim 1. How does membrane phosphoinositide and anionic composition influence myo1c membrane attachment lifetime?

An in depth understanding of the mechanical, structural, ATPase, and membrane-binding properties of myo1c is required to distinguish between mechanisms. Biochemical and biophysical experiments have provided valuable information about the capabilities of myo1c as a motor. One area that requires further exploration is the binding of myo1c to membranes containing phosphoinositides (Hokanson *et al.*, 2006; Hokanson and Ostap, 2006). Steady-state data revealing high affinity myo1c membrane binding is valuable, but it is also important to know the kinetics of the interaction, especially since the association of myo1c with cellular membranes is dynamic (Hokanson *et al.*, 2006). For example, in the models discussed above, myo1c attachment to GLUT4 vesicles could be direct, mediated through the putative pleckstrin homology domain (Figure 1.1, (1) right). Alternatively, myo1c recruitment to GLUT4

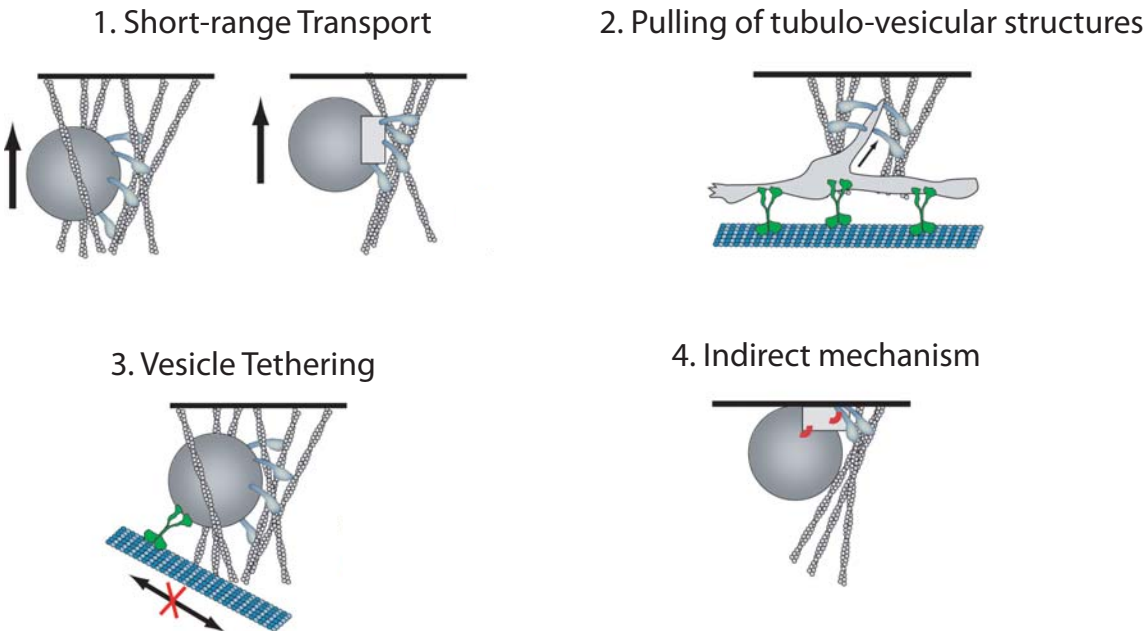

Figure 1.1 Models for myo1c in GLUT4 vesicle trafficking.

(1) Short-range transport. Myo1c transports vesicles towards the barbed ends of actin filaments, which are oriented towards the plasma membrane. Myo1c recruitment to vesicles could be through **(Left)** direct binding of myo1c through its PH domain. Alternatively, **(Right)** the interaction could be mediated through myo1c binding to proteins present on the vesicles, such as RalA.

(2) Pulling of tubulo-vesicular structures. Myo1c binds directly or indirectly to GLUT4 membranes. Myo1c motor activity transports membrane towards the cell surface. Because of anchoring of GLUT4 membranes to other structures, such as microtubules shown here, myo1c in effect pulls tubules towards the barbed-end of actin filaments.

(3) Vesicle tethering. Myo1c motor activity does not result in appreciable transport of vesicles along actin filaments. Instead, motor activity is required for dynamic tethering of vesicles to actin filaments. As a consequence of tethering to the actin cytoskeleton, transport of GLUT4 vesicles along microtubules could be disrupted.

(4) Indirect mechanism. Though evidence exists for myo1c recruitment to GLUT4 vesicles, much of myo1c is localized to the plasma membrane. This model proposes that the plasma membrane is a major site of myo1c action. Myo1c could be affecting membrane tension, for example, through binding simultaneously to the plasma membrane and actin filaments. Membrane tension could in turn influence GLUT4 vesicle fusion with the plasma membrane.

vesicles could occur through association with proteins localized to GLUT4 vesicles (Figure 1.1, (1) left), such as RalA, or some combination of direct and indirect binding.

Knowing more about the myo1c membrane attachment lifetime can provide insight into mechanisms of myo1c recruitment to GLUT4 vesicles. Discovering, for example, that myo1c membrane attachment lifetime is short relative to the time required for myo1c to complete an ATPase cycle would motivate a search to identify and characterize protein-protein interactions that might stabilize myo1c membrane attachment. In addition, GLUT4 vesicles have lipid composition different from that of the plasma membrane. It is important to understand how lipid composition influences the kinetics of myo1c membrane binding since this could potentially provide information about sites of action for myo1c in the absence of protein-protein interactions (Figure 1.1, (4)). Therefore, I have measured myo1c association with and dissociation from membranes of varying phosphoinositide and anionic lipid compositions.

Specific Aim 2. How is the cytoskeleton organized in 3T3-L1 adipocytes and how does cytoskeletal organization relate to GLUT4 vesicle dynamics?

At the same time, distinguishing among these possibilities, not all of which are mutually exclusive, will require a more in-depth understanding of the organization of the actin and microtubule cytoskeletons. Information about GLUT4 vesicle dynamics, motility, and localization relative to cytoskeletal filaments and motors will be important. The consequences of specific myo1c mutations that interfere in known ways with myo1c function must also be considered.

The second chapter of this thesis lays the groundwork for addressing the role of myo1c in part by examining microtubule localization and dynamics in adipocytes and the spatial relationship between microtubules and GLUT4 vesicle fusions with the plasma membrane. For example, in 3T3-L1 adipocytes, the microtubule cytoskeleton occupies a region extending throughout the volume of the cell. Due to the organization of the microtubule cytoskeleton, unrestricted movement along microtubules could lead to the displacement of surface-localized vesicles away from the cell membrane and deeper into the cell. Myo1c could potentially inhibit the inward, microtubule-dependent displacement by tethering the vesicle to cortical actin.

One question is whether we can observe myo1c recruitment to GLUT4 vesicles, and, if so, how recruitment correlates with microtubule-based transport. Alternatively, the recruitment of myo1c to GLUT4 vesicles could be constitutive and myo1c activation or engagement could instead be regulated. In considering these alternatives, it should be kept in mind that we might not observe myo1c localization to GLUT4 vesicles using live-cell TIRF microscopy. This could reflect limitations in our detection due to a transitory myo1c-GLUT4 vesicle interaction, low myo1c recruitment to GLUT4 vesicles compared to the extensive recruitment to the plasma membrane, or the presence of endogenous, non-fluorescent myo1c.

1.2 BACKGROUND INFORMATION

1.2.1 Myo1c

The Myosin Superfamily

Myosins comprise a large superfamily of actin-based motor proteins and are involved in a variety of processes ranging from muscle contraction to vesicle transport. Myosins bind actin and, with the exception of myosin-VI, move towards the barbed end of actin filaments. A feature shared by all myosins is the ability to perform mechanical work using the energy stored in ATP.

Myosins have a common domain structure, which includes motor, regulatory, and tail domains (Figure 1.2). The catalytic motor domain contains the actin-binding region and is the site of ATP binding and hydrolysis. Myosins coordinate the cycle of ATP binding, hydrolysis, and product release (Figure 1.3) with conformational changes in the motor domain that lead to force generation and differences in actin affinity (reviewed in (Geeves *et al.*, 2005)). In the absence of bound nucleotide, myosin (M) binds strongly to actin (A) in what is referred to as the rigor state. ATP binding to the actomyosin (AM) complex decreases the affinity of myosin for actin. Myosin-ATP (M(ATP)) dissociates from the actin filament, and ATP hydrolysis results in a conformational change that primes the myosin for force generation in a step called the reverse power-stroke. Upon myosin rebinding to the actin filament, inorganic phosphate (P_i) is released and myosin begins its power-stroke while strongly bound to the actin filament. Finally, myosin releases ADP, which in some myosins is the second step of a two-step power-stroke (Veigel *et al.*, 1999). Myosin is again in the rigor state and available to bind ATP and repeat the ATPase cycle.

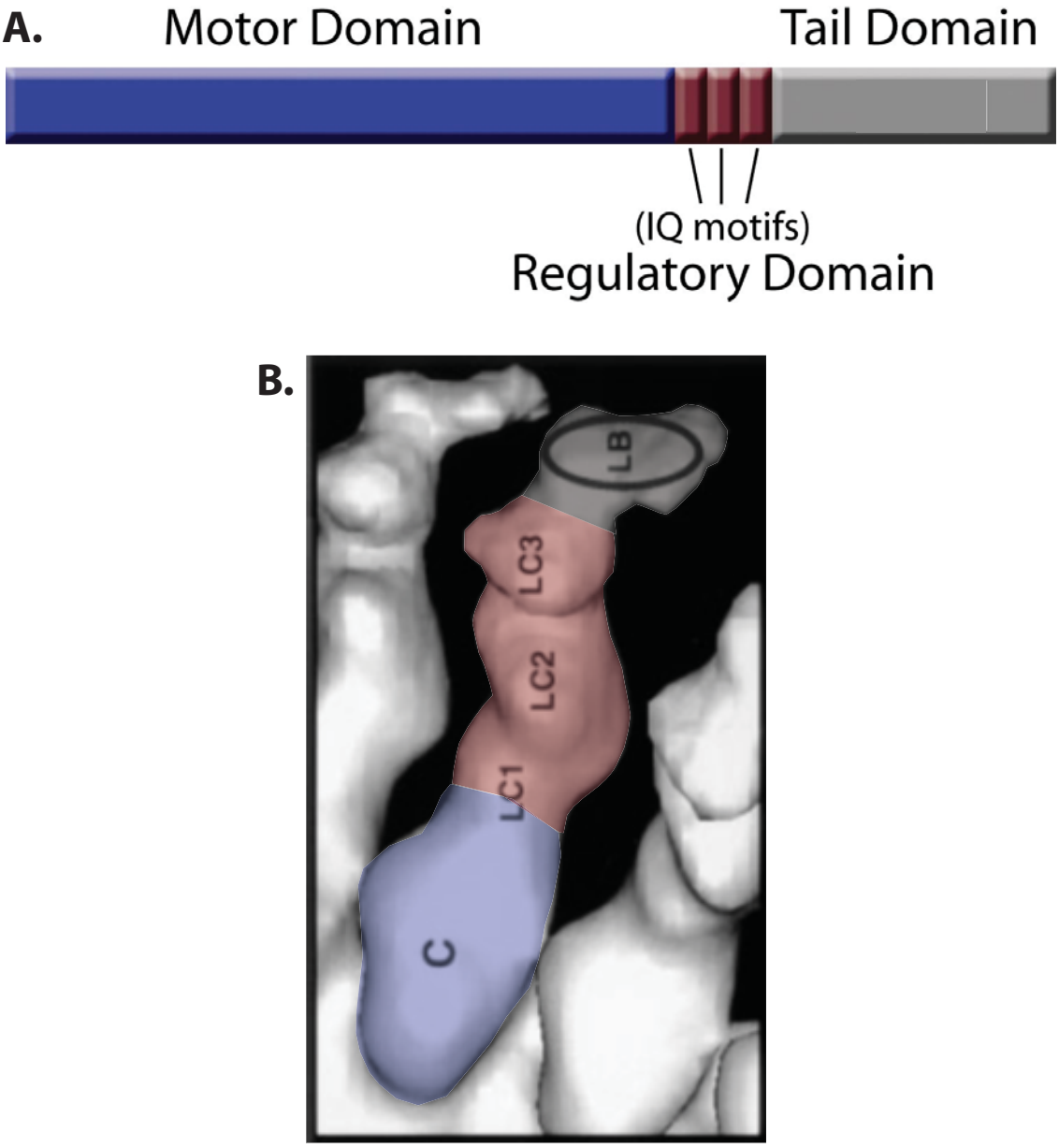

Figure 1.2 Myosin domain structure.

Myosins contain a motor domain (blue) that binds actin and hydrolyzes ATP, a regulatory domain (maroon) that serves as a lever arm and contains a variable number of IQ motifs, and a tail domain (gray) that differs significantly among myosins and may be specialized for protein or lipid interactions or for oligomerization.
(A) Schematic domain structure organization. **(B)** 3D map generated from a cryoelectron micrograph of an actin filament decorated wtih brush border myosin-I. C, catalytic motor domain; LC, light chain bound to IQ motif; LB, lipid-binding tail domain. Figure is modified from (Jontes *et al*. 1998).

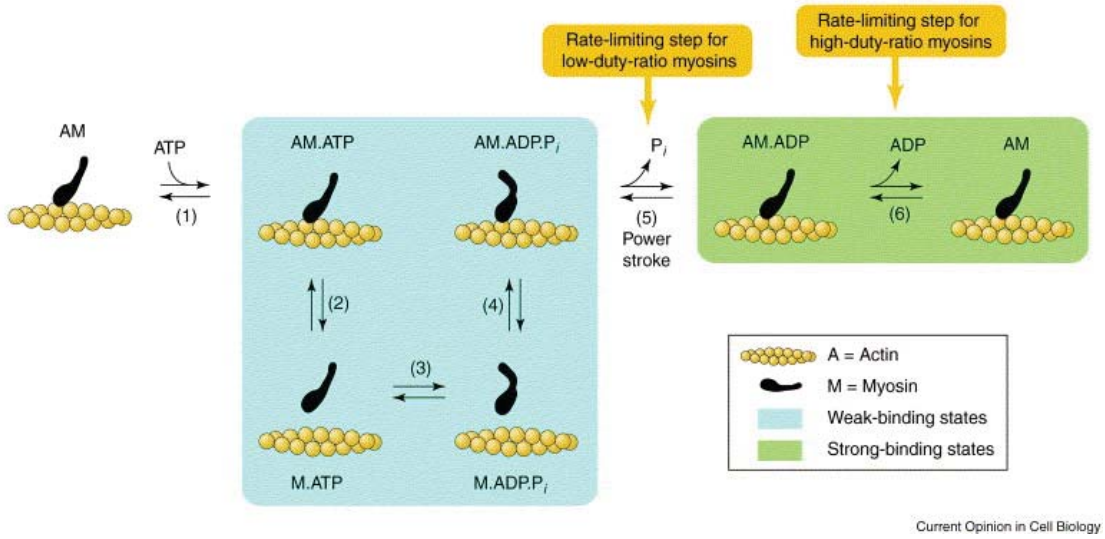

Figure 1.3 Actomyosin ATPase cycle.

(1) ATP binds the actomyosin complex (AM). ATP binding weakens the affinity of myosin (M) for actin (A), resulting in **(2)** myosin detachment from actin. **(3)** Myosin hydrolyzes ATP to ADP and inorganic phosphate (Pi). **(4)** Myosin, which has not yet released its hydrolysis products, rebinds the actin filament. **(5)** Force is generated during the myosin power-stroke, which accompanies Pi release. **(6)** Myosin releases ADP, which in some myosins is the second step of a two-step power-stroke. (Blue) Weak- and (Green) strong-binding states of myosin are indicated. Figure is from (De La Cruz, Ostap 2004).

The regulatory domain of myosin serves as a lever arm, amplifying conformational changes that take place in the motor domain to generate larger displacements (Rayment *et al.*, 1993). Myosin regulatory domains contain one or more IQ motifs, sequences of ~20-25 amino acids that form single α-helices. They are named for the presence of isoleucine (I) and glutamine (Q) at the start of the consensus sequence. Calmodulin and calmodulin-related proteins, which contain calcium-coordinating EF hand motifs, bind the IQ motifs. Binding of calmodulin stiffens the lever arm and is regulated by calcium binding (Manceva *et al.*, 2007).

The tail domain is the most diverse of the domains and provides a number of specializations (Mooseker and Cheney, 1995) that suit myosins to various functions. For example, the tail of myosin-V, a myosin important in vesicle transport, includes a predicted coiled-coil motif (Espreafico *et al.*, 1992) that allows for dimerization of myosin-V motors. The tail of myosin-II is important in the formation of bipolar filaments (Kiehart *et al.*, 1984). In addition, tails of many myosins contain sites for cargo binding, and they frequently contain motifs that mediate interactions with other proteins or with lipids (Mooseker and Cheney, 1995).

Myosin-I Family

Many families of myosins have so far been identified based on sequence analysis of their motor and tail domains (Berg *et al.*, 2001). Historically, myosins have been divided into conventional (i.e., filament-forming myosin-II) and unconventional myosins. Myosin-I is the largest of the unconventional myosin families in humans (Berg *et al.*, 2001). Myosin-Is are low molecular weight myosins that do not dimerize and are,

therefore, referred to as single-headed. They are found in organisms ranging from yeast and amoeba to humans. They are widely expressed in vertebrates, and many tissues express at least one myosin-I isoform (Sherr *et al.*, 1993).

Eight vertebrate myosin-I isoforms have been identified (myo1a – myo1h) (Figure 1.4, left). These can be divided into two subclasses: the short-tailed myosins, of which myo1c is a member, and the long-tailed myosins, which include myo1e and myo1f and have an extended tail domain. The tails of myosin-Is are characterized by the presence of tail homology (TH) domains (Figure 1.4, right). Both short- and long-tailed myosin-Is contain a basic TH1 domain involved in lipid binding. In addition to this domain, long-tailed myosins also possess a TH2 domain rich in glycine, proline, and alanine (GPA) residues and an SH3 interaction motif located in the TH3 domain.

Biochemical Properties

Although they share a common ATPase cycle, myosins differ in their biochemical properties, duration of biochemical intermediates of the ATPase cycle, and the relative amount of time they spend strongly bound to actin. These differences are expected to be important for the specialization of myosins to different cellular processes (reviewed in (De La Cruz and Ostap, 2004)). They can also influence factors such as cellular localization (Tang and Ostap, 2001).

Myosin-I isoforms are excluded from tropomyosin-containing actin filaments (Tang and Ostap, 2001). They are characterized by long-lived biochemical states (De La Cruz and Ostap, 2004) and have low duty ratios (Lewis *et al.*, 2006) (i.e. spend <20% of their ATPase cycle strongly bound to actin). However, at least some myosin-I

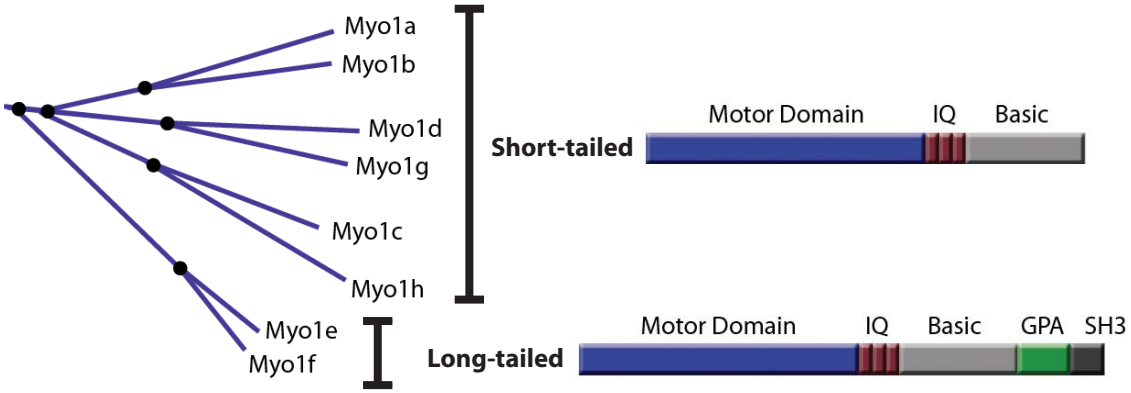

Figure 1.4 Myosin-I subclasses.

(Left) Unrooted phylogenetic tree depicting the relationships among vertebrate myosin-I isoforms.

(Right) Isoforms can be subdivided into long-tailed or short-tailed myosin-Is. Both contain a region of basic residues in the tail (TH1 domain, light gray). In addition, the tails of long-tailed myosin-Is have glycine-proline-alanine (GPA)-rich regions (TH2 domain, green) and an SH3 interaction motif (TH3 domain, dark gray). The number of IQ motifs varies, and alternative splicing of several myosin-Is generates splice isoforms of differing number of IQ motifs even within the same myosin-I.

isoforms can transition to high duty ratio motors under a resisting force. For example, Laakso et al. have demonstrated for the myo1b isoform that duty ratio increases significantly (> 0.9) under low loads (< 2 pN) (Laakso *et al.*, 2008).

Myosin-I membrane binding

Myosin-Is link cell membranes with the actin cytoskeleton and play crucial roles in several processes involving the dynamic reorganization of membrane (Bose *et al.*, 2002; Bose *et al.*, 2004; Holt *et al.*, 2002; Laakso *et al.*, 2008; Novak *et al.*, 1995; Tyska and Mooseker, 2004). For example, myosin-Is are involved in phagocytosis (Voigt *et al.*, 1999), compensatory endocytosis (Sokac *et al.*, 2006), and vesicle trafficking (Bose *et al.*, 2002; Bose *et al.*, 2004). A key property allowing myosin-I isoforms to carry out these functions is that they can simultaneously interact with both actin and lipid membranes. Studies have shown that myosin-I isoforms localize and fractionate with cell membranes (Bose *et al.*, 2002; Ruppert *et al.*, 1995), and biochemical experiments have shown myosin-I isoforms bind directly to lipid membranes (Adams and Pollard, 1989; Miyata *et al.*, 1989; Hayden *et al.*, 1990; Tang *et al.*, 2002).

Lipids of cellular membranes

Eukaryotic plasma membranes are composed of a variety of lipids in addition to transmembrane and peripherally-associated proteins. Of the phospholipids, lipids that contain a phosphate group in addition to fatty acids, phosphatidylcholine (PC) and phosphatidylethanolamine (PE) are the most abundant and account for ~40% - 50% and ~20% - 45% of the total, respectively (Leventis and Grinstein, 2010). Both PC and PE

are neutrally-charged, zwitterionic lipids. Lesser amounts of negatively charged phospholipids such as phosphatidylserine (PS), phosphatidic acid (PA), and phosphatidylinositol (PI) are also present in cellular membranes. Other important lipids present in cellular membranes include phosphoinositides, cholesterol, and sphingolipids such as sphingomyelin. It is worth noting that the lipid composition of different organelles varies greatly within a given cell type, and the composition of the plasma membrane also varies across different cell types (Leventis and Grinstein, 2010).

Though they make up a small percentage of cellular lipids, the phosphoinositides are an important class of phospholipids and are involved in processes including signal transduction and regulation of the actin cytoskeleton. They are also involved in localizing proteins to cellular membranes through binding motifs in the proteins (reviewed in (McLaughlin *et al.*, 2002)). Phosphoinositides are derived from PI, which has an inositol ring as part of its polar headgroup, and are named for the positions on the ring that are phosphorylated. Phosphatidylinositol 4,5-bisphosphate (PtdIns(4,5)P_2) is the most abundant, representing a few percent of the total phospholipid content of the plasma membrane, although local concentrations can be higher. Whereas PS carries an effective charge of -1, these anionic lipids have multiple negative charges per headgroup. The net charge of PtdIns(4,5)P_2, for example, can range from -2 to -4 (reviewed in (McLaughlin *et al.*, 2002)). Lipid kinases and phosphatases are important for the interconversion of the phosphoinositides. For example, PI3K phosphorylates PtdIns(4,5)P_2 on position 3 of the inositol ring to generate phosphatidylinositol 3,4,5-trisphosphate (PtdIns(3,4,5)P_3). In addition, phospholipases can cleave the headgroup to generate soluble inositol phosphates and important lipid second messengers.

Basis of membrane binding of myo1c

High affinity membrane binding is a key feature of myo1c and, along with its actin-binding properties, is one of the major factors that determine its intracellular distribution (Hokanson and Ostap, 2006; Tang and Ostap, 2001; Ruppert *et al.*, 1995). Myo1c is localized to the plasma membrane, the actin-rich cell cortex, as well as specialized membrane structures such as stereocilia and endocytic structures.

Membrane binding by myo1c is mediated through its tail domain, which contains a stretch of ~200 amino acids enriched in basic residues. Within this region a putative pleckstrin homology (PH) domain (Figure 1.5) has been identified that binds PtdIns(4,5)P_2 and other phosphoinositides with high affinity (K_d < 0.5 µM in terms of accessible phosphoinositide concentration) (Hokanson *et al.*, 2006). In addition, myo1c binds with similar affinity to soluble inositol phosphates such as inositol 1,4,5-trisphophate ($InsP_3$), the soluble headgroup of PtdIns(4,5)P_2. Point mutations of amino acids known to be essential for phosphoinositide binding in other PH domains inhibit myo1c binding to PtdIns(4,5)P_2 *in vitro*, and these mutations disrupt membrane localization *in vivo* (Hokanson *et al.*, 2006).

The presence of additional anionic phospholipids in the membrane increases the affinity of myo1c for PtdIns(4,5)P_2-containing membranes. This increased affinity may be due to non-specific electrostatic interactions between the anionic phospholipids and positively charged regions within the myo1c tail or regulatory domain (Hokanson *et al.*, 2006; Swanljung-Collins and Collins, 1994), which is similar to what has been found for the guanine nucleotide exchange factor, ADP-ribosylation factor nucleotide-binding site opener (ARNO) (Macia *et al.*, 2000). However, high-affinity membrane binding via these non-specific electrostatic interactions (i.e., binding in the absence of PtdIns(4,5)P_2)

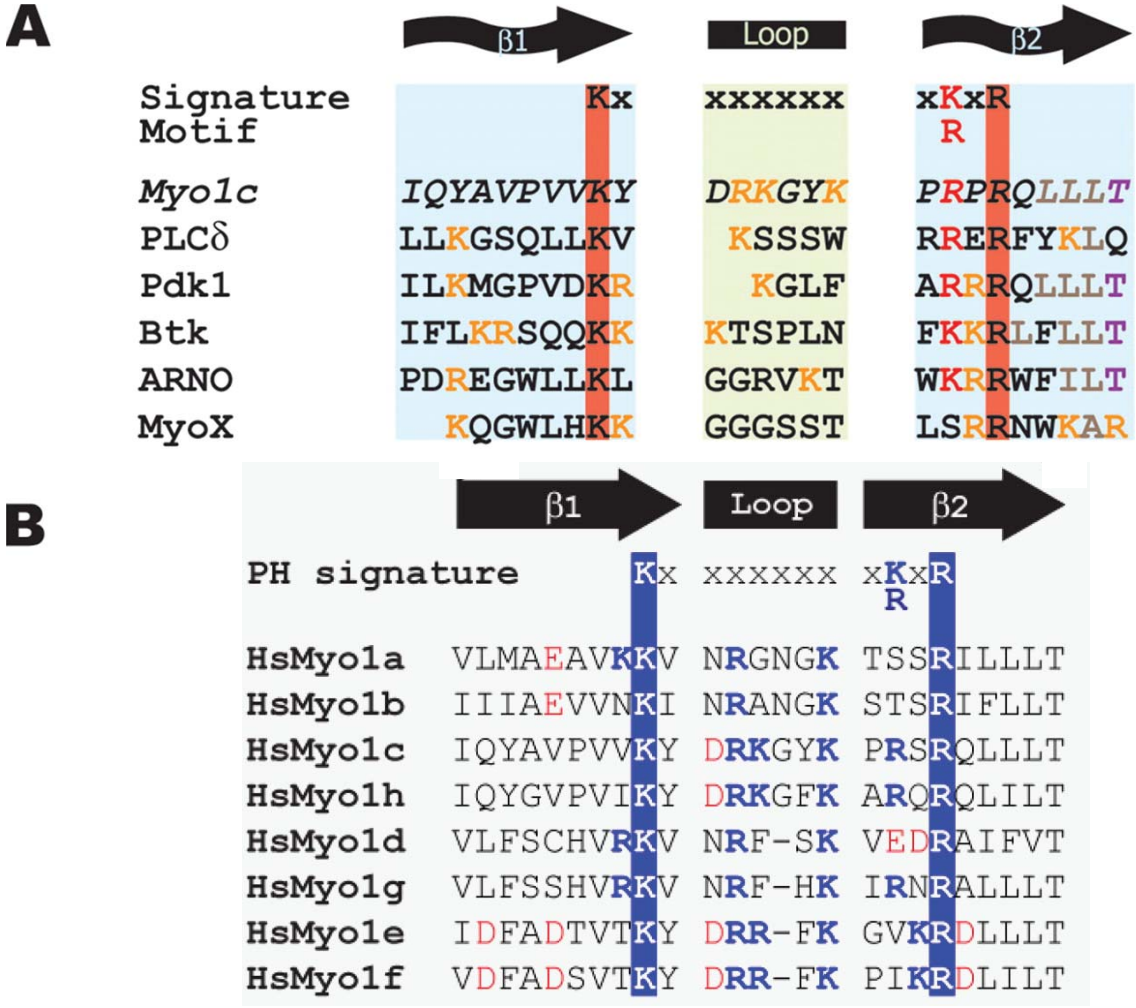

Figure 1.5 β1-loop-β2 motif of PH domains.

(A) Mouse myo1c (residues 884-908) has been aligned with the PH domain signature motif. Conserved basic residues shown in red are critical for membrane binding by PH domains. Other residues are depicted as follows: orange, other basic residues; brown, conserved hydrophobic patch; purple, conserved threonine. Figure is from (Hokanson et al. 2006).

(B) Alignment of other myosin-I isoforms. Conserved lysine and arginine residues are highlighted by the blue bars. Blue, basic residues; red, acidic residues. Figure is from (Feeser et al. 2010).

requires the membrane composition to contain a non-physiological mole fraction (e.g., > 40% phosphatidylserine) of anionic phospholipids (Hokanson *et al.*, 2006; Hokanson and Ostap, 2006).

The mechanisms of myo1c targeting and anchoring to specific regions on cellular membranes are not well understood. However, evidence is building that myo1c targeting requires direct binding of myo1c to phosphoinositides in cell membranes (Hokanson *et al.*, 2006; Hokanson and Ostap, 2006; Huang *et al.*, 2004; Hirono *et al.*, 2004).

Membrane binding by other myosin-Is

Myosin-I isoforms show considerable differences in the way they interact with membrane. For example, while all vertebrate myosin-Is appear by sequence alignment to have a PH domain (Hokanson *et al.*, 2006; Feeser *et al.*, 2010) (Figure 1.5), conserved PH domain residues are not required for membrane binding of all myosin-Is. Mutation of conserved PH domain residues disrupts *in vivo* membrane binding of myo1c, myo1f, myo1g, and myo1b (Hokanson *et al.*, 2006; Patino-Lopez *et al.*, 2010; Olety *et al.*, 2010; Komaba and Coluccio, 2010). However, these residues are not required for myo1e membrane binding *in vivo* or for PtdIns(4,5)P_2 binding *in vitro* (Feeser *et al.*, 2010). Furthermore, myosin-1s differ in their ability to bind membranes containing physiological concentrations of phosphatidylserine. As discussed above, myo1c shows high affinity membrane binding only at high phosphatidylserine concentrations (Hokanson *et al.*, 2006; Hokanson and Ostap, 2006). On the other hand, myo1e shows high affinity binding to membranes that contain physiological concentrations of either

phosphatidylserine or phosphoinositides (Feeser *et al.*, 2010). Electrostatic interaction between the basic tail domain and anionic phospholipids, rather than a stereo-specific interaction of the PH domain with phosphoinositides, appears to be the key feature of myo1e membrane binding. Similar findings have been demonstrated for *Acanthamoeba* myosin-IC (Brzeska *et al.*, 2008).

1.2.2 Glucose transporter-4 vesicle trafficking

Glucose transporter-4

GLUT4 belongs to a family of facilitative transporters, integral membrane proteins that have twelve transmembrane-spanning regions (Mueckler *et al.*, 1985). When embedded in the plasma membrane, they allow sugars to enter the cell down the concentration gradient in an ATP-independent manner. Transporters differ in the sugar for which they are specific and the kinetics of sugar transport (Bell *et al.*, 1993).

What makes GLUT4 unique among glucose transporters is that its intracellular localization and plasma membrane insertion are highly regulated by the peptide hormone insulin (James *et al.*, 1988; James *et al.*, 1989). The regulation of GLUT4 levels at the plasma membrane reflects the importance of GLUT4 in maintaining blood glucose levels. It is highly expressed in fat and muscle, insulin-responsive tissues that play key role in regulating whole body glucose homeostasis.

Under basal conditions (i.e. the absence of insulin signaling), the majority of GLUT4 is sequestered within a specialized, insulin-sensitive storage compartment in the form of vesicles or tubulo-vesicular structures (Slot *et al.*, 1991; Malide *et al.*, 2000). Only a small fraction of GLUT4 is embedded in the plasma membrane (Slot *et al.*, 1991).

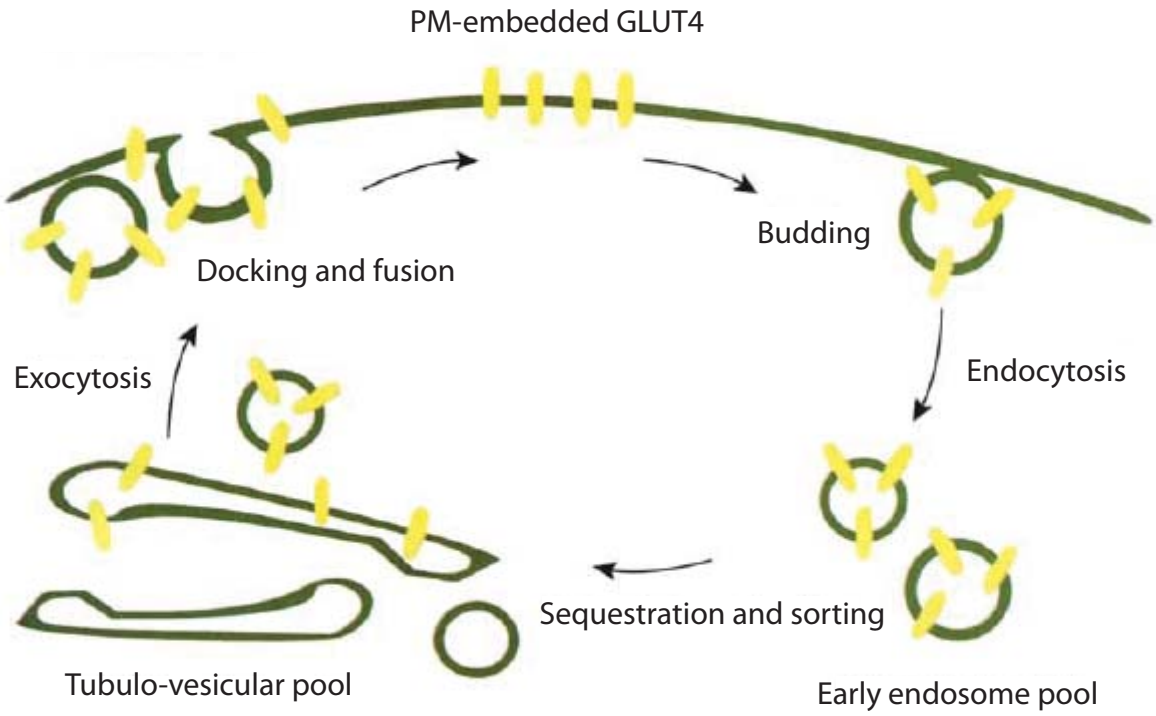

Figure 1.6 GLUT4 trafficking.

GLUT4 (yellow bars) traffics through multiple cellular compartments. Under basal conditions very little GLUT4 is embedded in the plasma membrane. Instead, GLUT4 is found in intracellular vesicle pools. A small fraction of GLUT4 is located within the early endosome pool. This pool includes GLUT4 that has been endocytosed from the plasma membrane. Most of GLUT4 is sorted away from early endosomes and is sequestered in the tubulo-vesicular pool, which serves as a source of GLUT4 for exocytosis in response to insulin. Insulin stimulation greatly increases the amount of GLUT4 embedded in the plasma membrane (PM), mostly by increasing the rate of exocytosis. Figure is adapted from (Holman, Cushman 1994).

The intracellular pool of GLUT4 is dynamic (Figure 1.6), and the basal distribution reflects fast endocytosis from the plasma membrane (Jhun *et al.*, 1992; Yang and Holman, 1993; Satoh *et al.*, 1993) and slow exocytosis of GLUT4-containing vesicles (Jhun *et al.*, 1992; Yang and Holman, 1993; Satoh *et al.*, 1993; Karylowski *et al.*, 2004). Insulin binding to the insulin receptor begins a series of signaling events, which culminate in a substantial increase in the rate of exocytosis (Jhun *et al.*, 1992; Yang and Holman, 1993; Satoh *et al.*, 1993; Karylowski *et al.*, 2004), greatly increasing the level of plasma membrane-inserted GLUT4 (Slot *et al.*, 1991).

Insulin signaling

Insulin binding to the insulin receptor activates the tyrosine kinase activity of the receptor and initiates a signaling cascade (Figure 1.7), which ultimately leads to increased insertion of GLUT4 into the plasma membrane (Hou and Pessin, 2007; Watson and Pessin, 2007; Zaid *et al.*, 2008). Substrates for the activated insulin receptor include important scaffolding proteins such as the insulin receptor substrate proteins IRS1/2. When phosphorylated on certain tyrosine residues, IRS1/2 provide binding sites for downstream effectors including PI3K. PI3K is an important kinase whose substrate is the phosphoinositide PtdIns(4,5)P_2. Once recruited to the cell membrane through binding to phosphorylated IRS1/2, PI3K catalyzes the conversion of PtdIns(4,5)P_2 to PtdIns(3,4,5)P_3. PtdIns(3,4,5)P_3 in turn is important for the binding of pleckstrin homology-domain containing proteins including Akt, a serine/threonine protein kinase. At the cell surface, Akt is activated by phosphorylation of threonine 308 and serine 473.

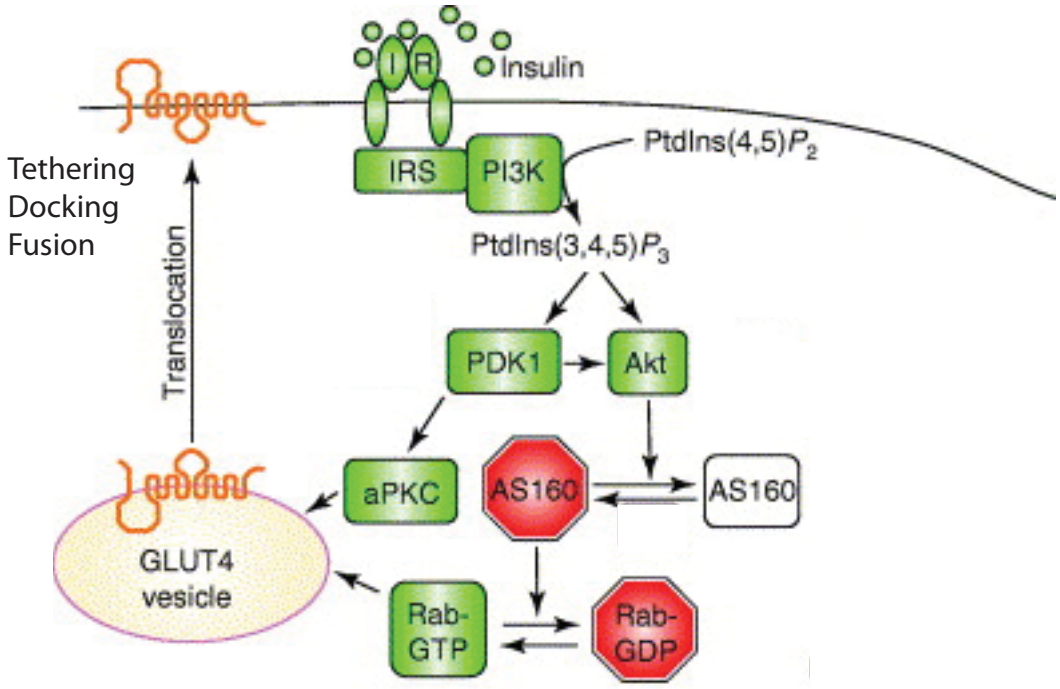

Figure 1.7 Insulin signaling cascade.

The PI3K-dependent signaling pathway begins with insulin binding to the insulin receptor (IR). Phosphorylated IR provides binding sites for the scaffolding protein IRS. PI3K is recruited to the plasma membrane through interaction with IRS. Active PI3K catalyzes the conversion of PtdIns(4,5)P_2 to PtdIns(3,4,5)P_3, which in turn activates the kinases PDK1 and Akt. Phosphorylation by Akt inactivates AS160, a negative regulator of Rab proteins. Activated Rabs (Rab-GTP) are proposed to be important for GLUT4 vesicle translocation. Green, positive regulators leading to translocation of GLUT4 vesicles; Red, negative regulators. Figure is adapted from (Watson, Pessin 2006).

Although the search for Akt substrates is ongoing, one important target that has been identified is Akt substrate of 160 kDa (AS160). AS160 acts as a GTPase activating protein (GAP) for Rab proteins (Figure 1.7) (Miinea *et al.*, 2005), small GTPases important in vesicle motility and fusion (reviewed in (Zerial and McBride, 2001)), present on GLUT4 vesicles. Akt phosphorylation of AS160 is thought to inactivate its Rab GAP activity (Kramer *et al.*, 2006), allowing for Rab activation and effector binding. Proposed effector proteins in GLUT4 trafficking include motors such as dynein and KIF3, a kinesin-II (Huang *et al.*, 2001; Imamura *et al.*, 2003). Identification of the specific Rabs and their effectors targeted by AS160 is ongoing.

Intersection of insulin signaling with GLUT4 vesicle trafficking

A major area of active research in the GLUT4 field remains the identification of the steps in GLUT4 trafficking that are regulated by insulin. Multiple processes have been identified as targets for insulin signaling (Figure 1.8). These include:

1. vesicle budding from GLUT4 storage compartments (Lauritzen *et al.*, February 2008);
2. release of vesicles from a retention mechanism (Bogan *et al.*, 2003);
3. mobilization of vesicles along microtubules (Fletcher *et al.*, 2000; Liu *et al.*, 2003);
4. actin polymerization and actin-dependent processes (Tsakiridis *et al.*, 1994; Tong *et al.*, 2001); and
5. vesicle tethering, docking, or fusion with the plasma membrane (Lizunov *et al.*, 2005; Eyster *et al.*, 2006; Huang *et al.*, 2007; Bai *et al.*, 2007).

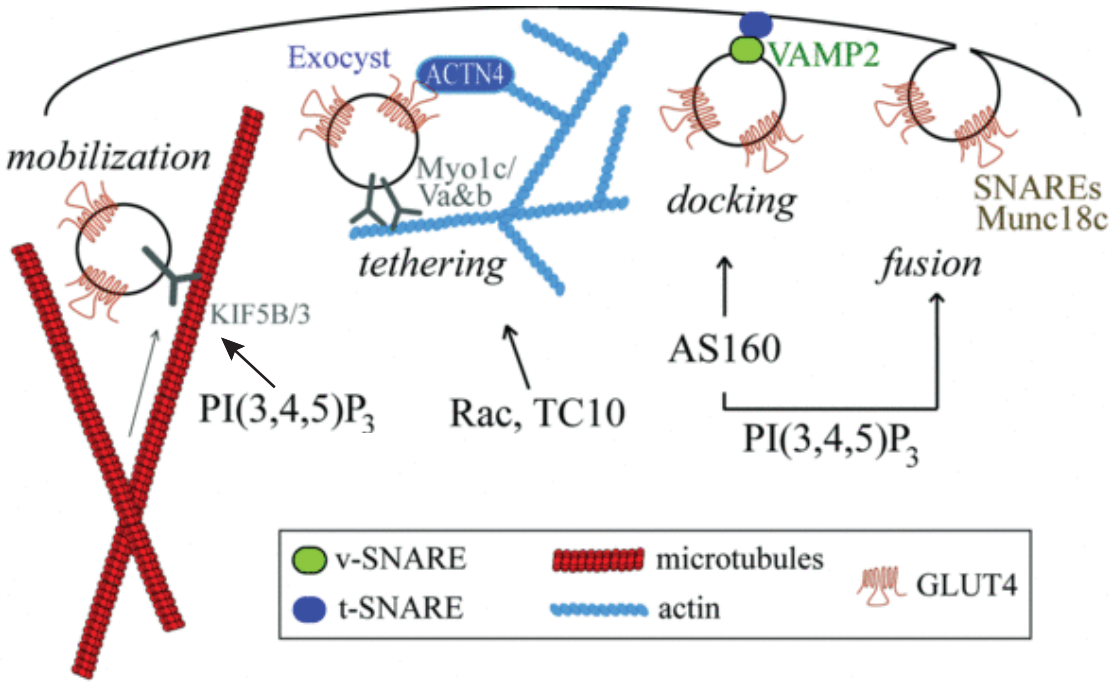

Figure 1.8 Intersection of insulin signaling with GLUT4 vesicle trafficking.

Multiple steps in GLUT4 trafficking have been identified as targets for insulin signaling, including vesicle budding from GLUT4 storage compartments and the release of vesicles from a retention mechanism (not shown). Other proposed targets are: **(left)** motor-dependent mobilization of GLUT4 vesicles along microtubules; **(center)** actin- and myosin-dependent processes such as GLUT4 vesicle anchoring to or transport along actin filaments; and **(right)** exocyst-dependent tethering, docking, and SNARE-dependent fusion of GLUT4 vesicles with the plasma membrane. Potential insulin signaling to these targets is indicated by an arrow. Figure is from (Zaid et al. 2008).

While insulin likely acts at multiple steps of GLUT4 trafficking, events occurring at the plasma membrane are now thought to be sites of primary regulation (Lizunov *et al.*, 2005; Huang *et al.*, 2007; Bai *et al.*, 2007) (reviewed in (Eyster and Olson, 2009)). The insertion of GLUT4 into the plasma membrane occurs through a multi-step process (Figure 1.8). Once vesicles are mobilized to the cell periphery, they tether, dock, and fuse with the plasma membrane (reviewed in (Hou and Pessin, 2007; Watson and Pessin, 2007; Zaid *et al.*, 2008; Thurmond and Pessin, 2001; Huang and Czech, 2007)). Tethering of GLUT4 vesicles, a process that involves the initial interaction of vesicles with the plasma membrane, has been proposed to occur through the exocyst complex (Inoue *et al.*, 2003; Ewart *et al.*, 2005; Lizunov *et al.*, 2009). The exocyst is a conserved complex of multiple proteins discovered because of its importance in polarized secretion in yeast (TerBush and Novick, 1995; TerBush *et al.*, 1996). Exocyst components identified as important in GLUT4 trafficking include Exo70, Sec6, and Sec8 (Inoue *et al.*, 2003; Ewart *et al.*, 2005; Lizunov *et al.*, 2009). GLUT4 vesicle fusion with the plasma membrane is mediated by soluble *N*-ethylmaleimide-sensitive factor attachment protein receptors (SNAREs) (reviewed in (Bryant and Gould, 2011)).

A difficulty in sorting out the specific steps of insulin regulation is that GLUT4-containing structures are not a homogenous population. GLUT4 traffics through multiple compartments in the cell (Figure 1.6). Immunolocalization studies have identified the presence of GLUT4 to varying extents within the trans-Golgi network, in early and late endosomes, in tubulo-vesicular structures, and at the plasma membrane (Slot *et al.*, 1991).

While there is some localization of GLUT4 to the recycling endosomal system, ablation studies in which transferrin receptor (Tf-R)-positive compartments were

destroyed have confirmed that a large proportion of GLUT4 resides in a specialized compartment from which the Tf-R is absent (Livingstone *et al.*, 1996). This second pool provides a source of GLUT4 for exocytosis following insulin stimulation (Livingstone *et al.*, 1996) and is often referred to as the insulin-sensitive compartment. In addition to GLUT4, insulin-responsive vesicles are also enriched for IRAP (Kandror and Pilch, 1994), sortilin (Lin *et al.*, 1997), low density lipoprotein receptor-related protein 1 (LRP1) (Jedrychowski *et al.*, 2010), and the vesicle SNARE (vSNARE) vesicle-associated membrane protein 2 (VAMP2) (Cain *et al.*, 1992; Larance *et al.*, 2005).

Insulin-responsive GLUT4 vesicles are biochemically distinct from vesicles that contain some GLUT4 but belong to the general endocytic pathway and contain proteins such as Tf-R and cellugyrin (Kupriyanova and Kandror, 2000; Kupriyanova *et al.*, 2002). While the insulin-responsive vesicles traffic very efficiently to the plasma membrane in response to insulin, this second pool of vesicles does not. In order to maintain the unique insulin-responsive character of GLUT4 vesicles following sequential rounds of fusion with the plasma membrane, there must be mechanisms in place to efficiently sort GLUT4 from the endocytic pathway so that insulin can efficiently stimulate a response. The lumenal domains of GLUT4, IRAP, sortilin, and LRP1 have been shown to interact, and these interactions are hypothesized to be important for sorting from the donor membrane (reviewed in (Bogan and Kandror, 2010)).

Role of the cytoskeleton in GLUT4 externalization

There is an increasing appreciation that both the actin and microtubule cytoskeletons participate in GLUT4 vesicle trafficking in response to insulin (reviewed in (Zaid *et al.*, 2008; Eyster and Olson, 2009) and discussed below) (Figure 1.8).

Microtubules and kinesins are thought to be involved in a pre-fusion step, and disruption of the microtubule cytoskeleton decreases the fraction of surface-localized GLUT4 by ~40% (Karylowski *et al.*, 2004; Fletcher *et al.*, 2000). Meanwhile, actin (Lopez *et al.*, 2009), myosin-I (Bose *et al.*, 2002; Bose *et al.*, 2004; Toyoda *et al.*, 2011), myosin-V (Yoshizaki *et al.*, 2007; Ishikura and Klip, 2008), and myosin-II (Fulcher *et al.*, 2008; Chung le *et al.*, 2010) likely act at the final steps of GLUT4 trafficking occurring at the plasma membrane, as discussed below.

Role of Actin Cytoskeleton

Much research has been dedicated to identifying the insulin-regulated signaling events involved in GLUT4 trafficking. Interestingly, several pathways impact the dynamics of cortical actin through the regulation of small GTPases (Chiu *et al.*, 2010) such as TC10 (Kanzaki *et al.*, 2002; Jiang *et al.*, 2002). There is an increase in the cortical actin meshwork in response to insulin (Tsakiridis *et al.*, 1994; Tong *et al.*, 2001; Kanzaki and Pessin, 2001), and it has been demonstrated that dynamic cortical actin is crucial to the proper trafficking of GLUT4. Disruption of the actin network with actin monomer sequestering or actin destabilizing compounds decreases GLUT4 plasma membrane insertion (Tsakiridis *et al.*, 1994; Lopez *et al.*, 2009; Kanzaki and Pessin, 2001) without affecting GLUT4 accumulation at the plasma membrane (Lopez *et al.*, 2009).

It is not clear how actin dynamics contribute to GLUT4 translocation. There is evidence that actin plays a role in organizing insulin signaling (Eyster *et al.*, 2005), but dynamic actin filaments could also be important structurally as tracks or sites of

attachment for actin-based myosin motors recruited to GLUT4-containing vesicles, as proposed in section 1.1 [Specific Aims] (Figure 1.1). In support of a structural role for actin, several myosins have been implicated in GLUT4 trafficking, among them myo1c, myoVa, and myosin IIA (Bose *et al.*, 2002; Bose *et al.*, 2004; Yoshizaki *et al.*, 2007; Ishikura and Klip, 2008; Fulcher *et al.*, 2008; Steimle *et al.*, 2005; Yip *et al.*, 2008). siRNA-mediated knock-down of myoVa inhibits GLUT4 translocation to the plasma membrane (Yoshizaki *et al.*, 2007). siRNA-mediated knock-down of myo1c or myosin IIA inhibits the plasma membrane insertion of GLUT4, and myo1c over-expression can overcome blockage of vesicle fusion brought about through PI3K inhibition (Bose *et al.*, 2002; Bose *et al.*, 2004; Fulcher *et al.*, 2008; Chung le *et al.*, 2010).

Role of Microtubules

Tracking and mobility analysis examining the movements of individual GLUT4 vesicles in live cells has provided further evidence for a role of microtubules in GLUT4 trafficking. However, in many cases, the studies do not directly distinguish individual GLUT4 vesicles that ultimately fuse with the plasma membrane in response to insulin from those that do not. GLUT4-containing vesicles move laterally distances greater than 1 µm (Fletcher *et al.*, 2000; Lizunov *et al.*, 2005; Semiz *et al.*, 2003; Chen *et al.*, 2008; Fujita *et al.*, 2010), the movements co-localize with microtubules (Lizunov *et al.*, 2005; Semiz *et al.*, 2003), and long-distance movement requires intact microtubules (Fletcher *et al.*, 2000; Semiz *et al.*, 2003; Chen *et al.*, 2008). Analyses to assess the mobility of GLUT4 vesicles, for example fluorescence recovery after photobleaching, reveal that vesicles are mobile in the basal state and microtubule disruption reduces basal mobility (Eyster *et al.*, 2006).

Several microtubule motors have been identified that could mediate GLUT4 vesicle movement along microtubules. Rab5, Rab4, and the scaffolding protein Daxx present on GLUT4 vesicles have been identified as insulin-sensitive interacting partners for dynein, a kinesin II (KIF3), and kinesin I (KIF5B), respectively (Huang *et al.*, 2001; Imamura *et al.*, 2003; Lalioti *et al.*, 2009). Disruption of the plus-end directed motors KIF3 through antibody injection (Imamura *et al.*, 2003) or conventional kinesin through over-expression of a dominant-negative mutant of conventional kinesin light chain (Semiz *et al.*, 2003) decreases GLUT4 translocation in response to insulin.

Chapter 2. Kinetics of the interaction of myo1c with phosphoinositides

This research was originally published in the Journal of Biological Chemistry. Portions of the manuscript appear in or have been adapted for this thesis.

Dawicki McKenna, Jennine M. and E. Michael Ostap. Kinetics of the interaction of myo1c with phosphoinositides. *J Biol Chem*. 2009 Oct 16; 284(42):28650-9.

2.1 SUMMARY

Myo1c is a member of a class of myosins (myosin-I) that dynamically localize to cellular membranes and link them to the actin cytoskeleton. These myosins are present in most eukaryotic cells and play important roles in cellular processes that involve membrane reorganization. Since phosphoinositide binding is important for the cellular localization and function of myo1c (Hokanson *et al.*, 2006), understanding how myo1c interacts with lipid membranes is essential. A putative pleckstrin homology domain has been identified in the myo1c tail that binds phosphoinositides and soluble inositol phosphates with high affinity. However, the kinetics of association and dissociation and the influence of phospholipid composition on the kinetics have not been determined. Determining the kinetics of membrane attachment will provide insight into the relationship between membrane-attachment and actin-attachment lifetimes, and will also provide details about the role of anionic lipids in regulating membrane attachment.

Stopped-flow spectroscopy was used to measure the binding and dissociation of a recombinant myo1c construct containing the tail and regulatory domains (myo1c$^{IQ\text{-}tail}$) to and from 100 nm diameter large unilamellar vesicles (LUVs). We found the time course of association of myo1c$^{IQ\text{-}tail}$ with LUVs containing 2% phosphatidylinositol 4,5-bisphosphate (PtdIns(4,5)P_2) followed a 2-exponential time-course, and the rate of the predominant, fast-phase depended linearly upon the total lipid concentration. The apparent second-order rate constant was approximately diffusion-limited. Increasing the molar ratio of anionic phospholipid by adding phosphatidylserine, additional PtdIns(4,5)P_2, or by situating PtdIns(4,5)P_2 in a more physiologically relevant lipid background increased the apparent association rate constant less than 2-fold. Myo1c$^{IQ\text{-}tail}$ dissociated from PtdIns(4,5)P_2 at a slower rate (2.0 s^{-1}) than the pleckstrin homology

domain of phospholipase C-δ (PLCδ-PH) (13 s^{-1}). The presence of additional anionic phospholipid reduced the myo1c$^{IQ\text{-}tail}$ dissociation rate constant > 50-fold, but marginally changed the dissociation rate of PLCδ-PH, suggesting that additional electrostatic interactions in myo1c$^{IQ\text{-}tail}$ help to stabilize binding. Remarkably, high concentrations of soluble inositol phosphates induce dissociation of myo1c$^{IQ\text{-}tail}$ from LUVs, suggesting that phosphoinositides are able to bind and dissociate from myo1c$^{IQ\text{-}tail}$ as it remains bound to the membrane.

2.2 MATERIALS AND METHODS

2.2.1 Reagents

$InsP_3$ was from Calbiochem. Phytic acid ($InsP_6$) was from Sigma. The following lipids were from Avanti: 1-Palmitoyl-2-Oleoyl-*sn*-Glycero-3-Phosphocholine (POPC), 1-Palmitoyl-2-Oleoyl-*sn*-Glycero-3-Phosphoethanolamine (POPE), 1-Palmitoyl-2-Oleoyl-*sn*-Glycero-3-[Phospho-L-Serine] (POPS), L-α-Phosphatidylinositol (PI), Sphingomyelin (SM), L-α-Phosphatidylinositol-4,5-bisphosphate ($PtdIns(4,5)P_2$), 1,2-Dioleoyl-*sn*-Glycero-3-Phosphocholine (DOPC), 1,2-Dioleoyl-*sn*-Glycero-3-[Phospho-L-Serine] (DOPS), and 1,2-Dioleoyl-*sn*-Glycero-3-Phosphoinositol-3,4,5-trisphosphate ($PtdIns(3,4,5)P_3$).

2.2.2 Protein Expression Constructs

A construct ($myo1c^{IQ\text{-}tail}$) (Figure 2.1) that contains the tail and regulatory domains of mouse myo1c (residues 690-1028) and an N-terminal poly-His tag has been described previously (Tang *et al.*, 2002). A bacterial construct of the PH domain of phospholipase-Cδ (PLCδ-PH) was a gift from Dr. M. Lemmon (University of Pennsylvania) and has been described previously (Lemmon *et al.*, 1995).

2.2.3 Myo1c Expression and Purification

$Myo1c^{IQ\text{-}tail}$ was co-expressed with calmodulin in *Sf*9 cells using a Baculovirus expression system and purified as previously described (Hokanson and Ostap, 2006; Tang *et al.*, 2002). Briefly, insect cells were co-infected with viruses containing the constructs for $myo1c^{IQ\text{-}tail}$ and calmodulin. Cells were harvested, lysed in Lysis Buffer (25 mM Tris, pH 7.5, 20 mM imidazole, 300 mM NaCl, 0.5 mM EGTA, 0.5% Igepal, 1 mM β-

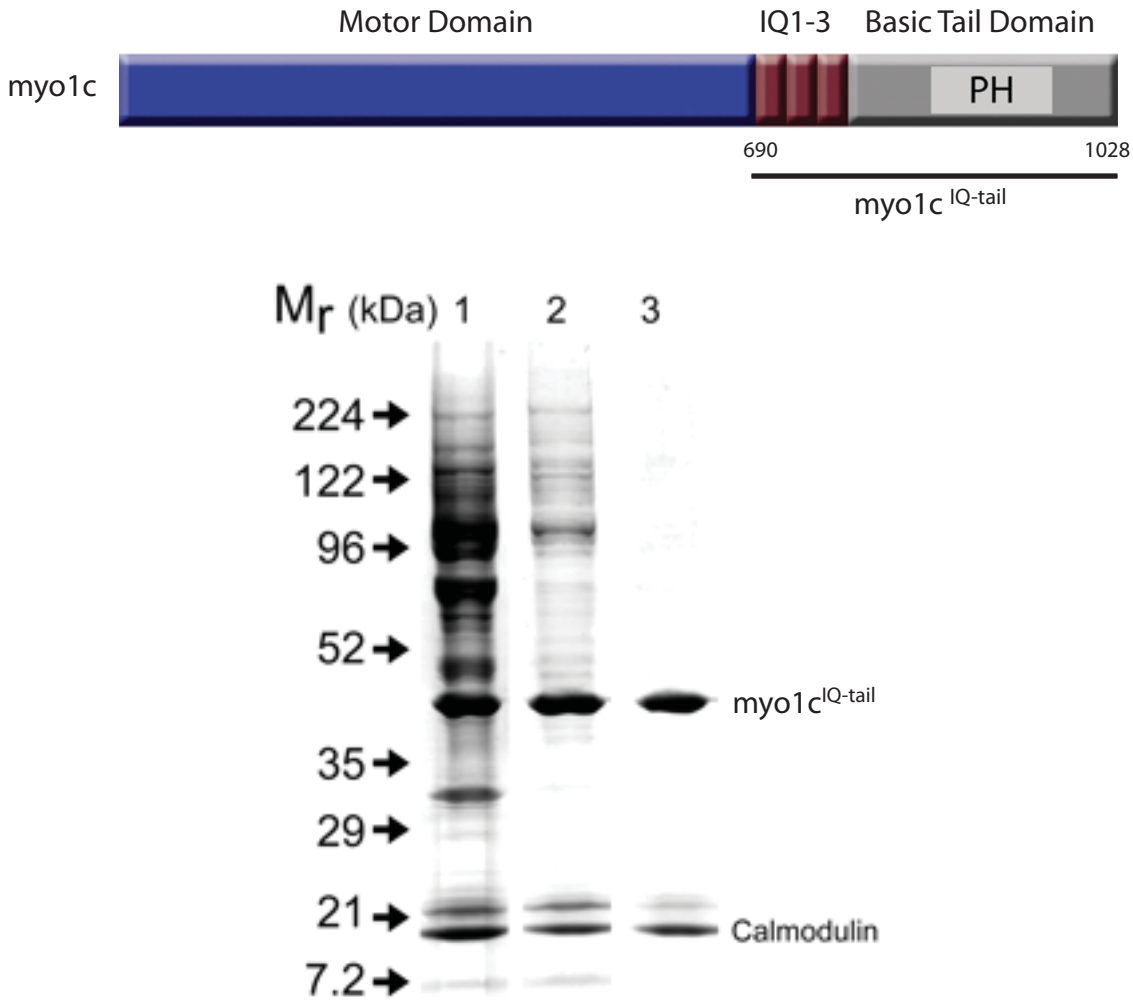

Figure 2.1 myo1c$^{IQ\text{-}tail}$ construct and purification.

(Top) Schematic of myo1c illustrating the residues (690-1028) included in the expressed protein myo1c$^{IQ\text{-}tail}$. The expressed protein also has an N-terminal poly-His tag (not shown).

(Bottom) The SDS-polyacrylamide gel stained with Coomassie shows intermediates in the myo1c$^{IQ\text{-}tail}$ purification process: 1) elution from the nickel-nitrilotriacetic acid column; 2) mono-S elution; 3) mono-Q elution. The calculated molecular mass of myo1c$^{IQ\text{-}tail}$ is 39 kDa. The myosin light chain calmodulin co-purifies with myo1c$^{IQ\text{-}tail}$. SDS-PAGE gel is from (Tang, Ostap 2001).

mercaptoethanol, 1 mM PMSF, 0.01 mg/mL aprotinin, and 0.01 mg/mL leupeptin), and homogenized with a Dounce homogenizer. Lysed cells were centrifuged, and the supernatant, to which DNase and RNase had been added, was sonicated. Lysate was loaded onto a Ni-NTA column (Qiagen) and eluted with 125 mM imidazole. Myo1c$^{IQ\text{-}tail}$ was further purified using MonoS and MonoQ FPLC columns (Amersham Biosciences). Purified myo1c$^{IQ\text{-}tail}$ was dialyzed overnight against HNa100 (10 mM HEPES, pH7, 100 mM NaCl, 1 mM EGTA, and 1 mM DTT).

2.2.4 PLCδ-PH Purification and IAEDANS Labeling

BL21(DE3)PLysS cells were transformed with PLCδ-PH domain plasmid DNA, and protein was expressed and purified as described (Ferguson *et al.*, 1994) with slight modifications. Cells were lysed in Lysis Buffer (100 mM NaCl, 10 mM D-glucose, 5 mM DTT, 1mM PMSF, and 25 mM MES, pH6). The lysate was sonicated and centrifuged. Supernatant was loaded onto a DEAE-cellulose (Sigma-Aldrich) column, which was pre-equilibrated with Buffer A (50 mM NaCl, 1 mM DTT and 25 mM MES, pH 6). The column was washed with Buffer A plus 1mM PMSF. The flow-through, which contained the PLCδ-PH domain, and wash was then loaded onto an SP Sepharose Fast Flow (Sigma-Aldrich) column pre-equilibrated with Buffer B (Buffer A without NaCl). The SP column was washed, and protein was eluted in Buffer B with a 0 mM – 500 mM NaCl gradient. Protein-containing fractions were ammonium sulfate precipitated. After centrifugation, the pellet was resuspended in labeling buffer (20 mM Tris, pH 7.5, 150 mM NaCl, 1 mM EGTA) and loaded onto a pre-equilibrated Superdex 200 10/300 GL (Amersham Biosciences) column. PLCδ-PH containing fractions were pooled and labeled with five-fold molar excess of the thiol-reactive dye, 5-((((2-iodoacetyl)amino)ethyl)amino)naphthalene-1-sulfonic acid (IAEDANS) in labeling buffer

at RT for 6 hours. To remove free dye, labeled protein was passed over a G25 Fine column pre-equilibrated with HNa100. The efficiency of labeling was 80% as calculated assuming ε_{280} =18,470 $M^{-1}cm^{-1}$ for PLCδ-PH and ε_{336} = 5700 $M^{-1}cm^{-1}$ for IAEDANS.

2.2.5 Preparation of LUVs

LUVs were prepared as previously described (Hokanson and Ostap, 2006). Briefly, lipids were combined in the molar ratios indicated in Table 2.1. Solvent was evaporated under a stream of nitrogen. For LUVs composed of complex lipid mixtures, solvent was removed in a rotovap following pre-equilibration at 30°C to ensure a uniform lipid distribution (Gambhir *et al.*, 2004). Dried lipid films were resuspended in HNa100 and briefly vortexed. Lipids underwent five cycles of freeze-thaw before brief bath sonication and eleven passes through 100 nm pore-size nitrocellulose membranes (Whatman) in an extruder (Avanti Polar Lipids).

Hydrodynamic radii of LUVs were measured using Dynamic Light Scattering (DLS; Table 2.1) (Dynamics v5.26.37). Radii determined by DLS were used to calculate estimated molecular weights (Table 2.1) of the LUVs as described (Lu and Nelsestuen, 1996).

2.2.6 Stopped-Flow Measurements

All measurements were performed in 10 mM HEPES, pH7, 100 mM NaCl, 1 mM EGTA, and 1 mM DTT at 22 ± 0.1 °C. Experiments with myo1c$^{IQ\text{-}tail}$ included 1 µM free calmodulin. Association and dissociation transients were acquired using a stopped-flow instrument equipped with removable polarization optics (Applied Photophysics, Spectra Kinetic Workstation v4.54). Light scattering measurements were performed in an L-format with an excitation wavelength of 340 nm and a 320 nm long-pass emission filter.

Table 2.1: Phospholipid Composition of LUVs

LUV	Lipid Mole Fraction						LUV Radius[a] (nm)	Estimated Molecular Weight[c]
	DOPC	**DOPS**	**PtdIns(4,5)P_2**	**PtdIns(3,4,5)P_3**				
0.5% PtdIns(4,5)P_2	0.995	0	0.0050	0			N.D.	N.D.
2% PtdIns(4,5)P_2	0.980	0	0.0200	0			42 ± 0.60	5.7 x 10^7
8% PtdIns(4,5)P_2	0.920	0	0.0800	0			48 ± 4.0	8.0 x 10^7
2% PtdIns(4,5)P_2 + 20% DOPS	0.780	0.200	0.0200	0			49 ± 4.7	8.8 x 10^7
2% PtdIns(3,4,5)P_3	0.980	0	0	0.0200			35 ± 4.1	3.9 x 10^7
LUV	**POPE**	**POPC**	**POPS**	**PI**	**SM**	**PtdIns(4,5)P_2**		
0.5% PtdIns(4,5)P_2 + Lipid Mix[b]	0.474	0.199	0.184	0.0920	0.0460	0.0050	N.D.	N.D.
2% PtdIns(4,5)P_2 + Lipid Mix[b]	0.474	0.184	0.184	0.0920	0.0460	0.0200	52 ± 0.55	8.7 x 10^7

[a]Determined from dynamic light scattering measurements. Errors are standard deviations from 3 – 4 independent measurements.

[b]From reference (Corbin et al. 2004).

[c]Calculated as in reference (Lu, Nelsestuen 1996).

N.D. Not determined.

A small mixing artifact that was due to light scattering by LUVs was subtracted from transients before fitting. An additional artifact was observed when high concentrations of inositol phosphates (i.e., concentrations > 1 mM) were mixed with LUVs. Therefore, in $InsP_6$-induced dissociation experiments, no more than 1 mM $InsP_6$ was used, and a blank acquired in the absence of myo1c$^{IQ\text{-}tail}$ at each $InsP_6$ concentration was subtracted from transients. Stopped-flow anisotropy measurements were carried out in a T-format spectrometer with an excitation wavelength of 336 nm and a 475 nm long-pass emission filter. Anisotropy was calculated as described (Lakowicz, 1999).

The rate of myo1c$^{IQ\text{-}tail}$ binding to LUVs at each lipid concentration was determined in each experiment by averaging 2 - 6 individual traces and fitting to a two-exponential function ($y = A_{fast} (1 – e^{-kfast \cdot t}) + A_{slow} (1 – e^{-kslow \cdot t})$. Rates reported for each total lipid concentration were from 1 – 4 experiments. A minimum of five lipid concentrations were assayed for each LUV composition, and the final myo1c$^{IQ\text{-}tail}$ concentration was 1000-fold below the total lipid concentration. Association transients were acquired under pseudo-first-order conditions to obtain apparent second-order rate constants from the slope of a plot of k_{fast} versus lipid concentration. Association rate constants are reported as a function of total lipid ($k_{a\text{-}total}$) or LUV concentration ($k_{a\text{-}LUV}$). Reported uncertainties are the standard errors of the fits.

Dissociation rates and amplitudes were obtained by averaging the individual traces from each experiment and fitting to a single-exponential function ($y = A_{dis} (1 – e^{-kdis \cdot t})$), where A_{dis} = final amplitude - initial amplitude. Average rates and standard deviations from multiple experiments (n = 2 -7) are reported (Table 2.2). For experiments that require large quantities of soluble inositol phosphates (Figures 2.2 and 2.6), myo1c$^{IQ\text{-}tail}$ -LUV complexes were mixed with $InsP_6$ to induce dissociation. $InsP_6$

and $InsP_3$ bind myo1c$^{IQ\text{-}tail}$ with similar affinity (Hokanson *et al.*, 2006), and $InsP_6$ is substantially less expensive than $InsP_3$.

2.3 RESULTS

2.3.1 Light scattering linearly reports the concentration of myo1c$^{IQ\text{-}tail}$ bound to LUVs.

Hokanson et al. demonstrated that myo1c$^{IQ\text{-}tail}$ binds to phosphoinositide-containing LUVs at steady-state (Hokanson *et al.*, 2006; Hokanson and Ostap, 2006). However, the kinetics of association and dissociation were not known. We measured the rate of dissociation of myo1c$^{IQ\text{-}tail}$ from phosphoinositide-containing LUVs by monitoring changes in light scattering upon rapid mixing with high concentrations of $InsP_3$ or $InsP_6$. Myo1c$^{IQ\text{-}tail}$ binds $InsP_3$, $InsP_6$, and PtdIns(4,5)P_2-containing LUVs with similar affinities (Hokanson *et al.*, 2006), and these soluble inositol phosphates compete with phosphoinositide-containing LUVs for binding to myo1c$^{IQ\text{-}tail}$. Myo1c$^{IQ\text{-}tail}$ that has dissociated from an LUV has a greater probability of binding to an inositol phosphate than rebinding to a phosphoinositide-containing LUV, resulting in decreased light scattering.

When PtdIns(4,5)P_2-containing LUVs (115 µM total lipid) pre-equilibrated with myo1c$^{IQ\text{-}tail}$ (58 – 460 nM) were rapidly mixed with 58 µM $InsP_6$, the amplitude change in light scattering upon dissociation increased linearly as a function of myo1c$^{IQ\text{-}tail}$ concentration (Figure 2.2). Below 58 nM myo1c$^{IQ\text{-}tail}$, transients were difficult to resolve. Steady-state measurements of the fraction of myo1c bound to LUVs, performed using sedimentation of sucrose-loaded vesicles, showed that inositol phosphates completely displace myo1c from PtdIns(4,5)P_2-containing LUVs at the concentrations used in our light scattering experiments (Hokanson *et al.*, 2006). Therefore, we conclude that light scattering linearly reports the concentration of myo1c$^{IQ\text{-}tail}$ bound to LUVs.

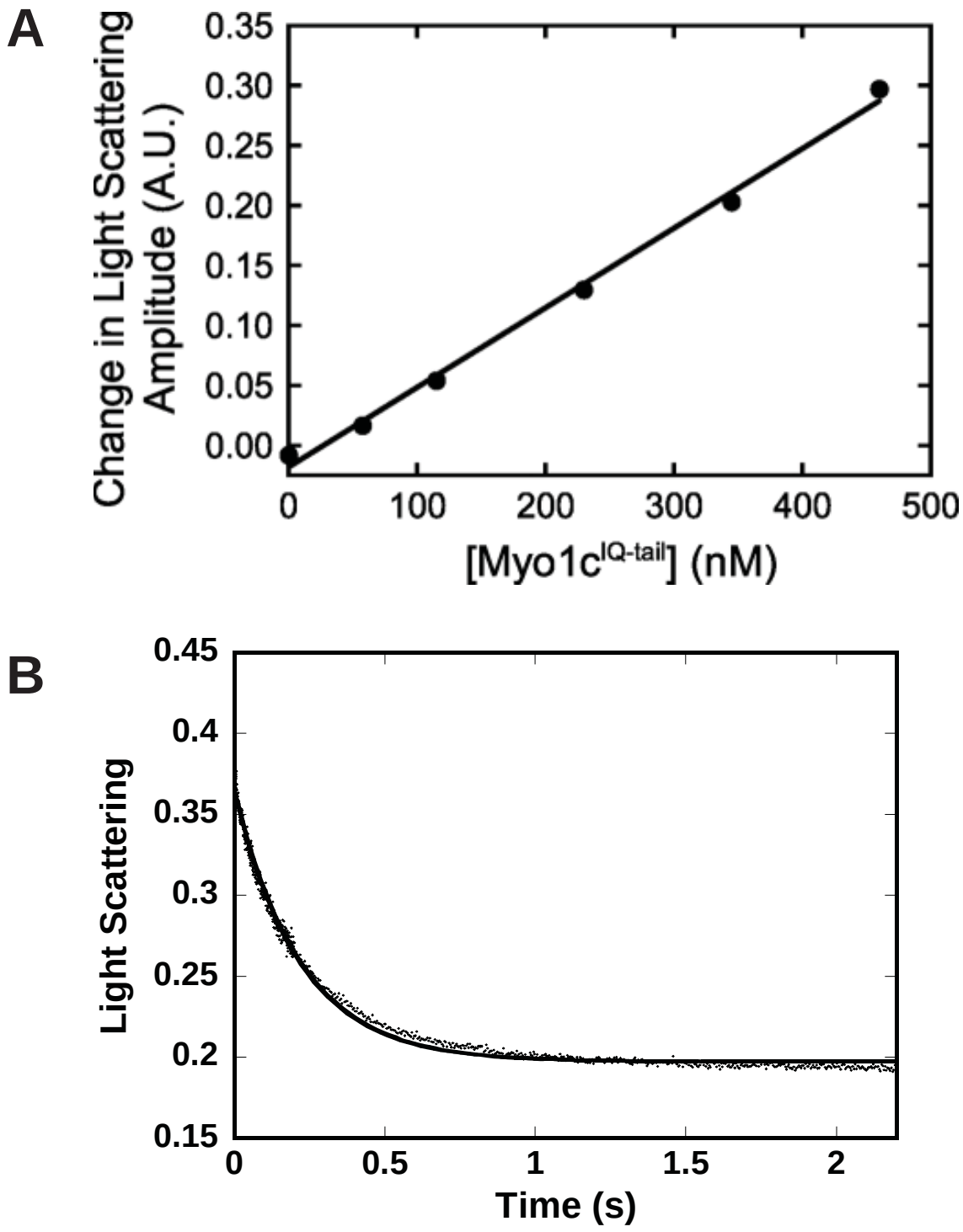

Figure 2.2 Amplitude change of light scattering of LUVs increases linearly with myo1c$^{IQ\text{-}tail}$ concentrations.

Figure 2.2 Amplitude change of light scattering of LUVs increases linearly with myo1c$^{IQ\text{-}tail}$ concentrations.

(A) LUVs containing 2% PtdIns(4,5)P_2 (115 μM total lipid) were pre-equilibrated with increasing concentrations of myo1c$^{IQ\text{-}tail}$ and mixed with either buffer alone or 58 μM InsP_6. Blank-subtracted transients were fit to a single exponential function and the amplitudes of the fits are plotted as a function of the myo1c$^{IQ\text{-}tail}$ concentration. The solid line represents a linear fit to the data. Concentrations are after mixing.

(B) LUVs containing 2% PtdIns(4,5)P_2 (115 μM total lipid) were pre-equilibrated with 230 nM myo1c$^{IQ\text{-}tail}$ and mixed with 58 μM InsP_6. Experimental time-course (dots) is a blank-subtracted average of 5 traces. The solid line is the best fit to a single exponential function. Concentrations are after mixing.

Steady-state measurements show that myo1c$^{IQ\text{-}tail}$ does not bind LUVs composed exclusively of DOPC (Hokanson and Ostap, 2006), the neutrally-charged lipid of which the LUVs are predominantly composed (Table 2.1). In keeping with this finding, control stopped-flow experiments showed that there is no significant change in light scattering when 50 µM 100% DOPC LUVs pre-equilibrated with myo1c$^{IQ\text{-}tail}$ were mixed with $InsP_3$ (Figure 2.3).

2.3.2 Dissociation of myo1c$^{IQ\text{-}tail}$ from PtdIns(4,5)P_2-containing LUVs is slowed by the presence of additional anionic charge.

The time course for dissociation of 100 nM myo1c$^{IQ\text{-}tail}$ from 50 µM 2% PtdIns(4,5)P_2 LUVs was obtained by mixing with 25 µM $InsP_3$ (50-fold molar excess relative to the accessible phosphoinositide concentration). The decrease in light scattering was best fit with a single exponential function with a rate of k_{dis} = 2.0 ± 0.30 s^{-1} (Figure 2.4, Table 2.2).

High affinity binding of myo1c$^{IQ\text{-}tail}$ to LUVs is achieved with 2% PtdIns(4,5)P_2; however, affinity increases ~5-fold when 20% DOPS, a negatively charged lipid, is included in LUVs containing 2% PtdIns(4,5)P_2 (Hokanson *et al.*, 2006). To address whether additional negative charge affects the kinetics of dissociation, dissociation rates were measured from LUVs with the lipid compositions indicated in Table 2.1. The dissociation rate was 8.5-fold faster when the mole percentage of PtdIns(4,5)P_2 was decreased to 0.5% (k_{dis} = 17 ± 0.38 s^{-1}) and was 12-fold slower when the mole percentage of PtdIns(4,5)P_2 was increased to 8% (k_{dis} = 0.16 ± 0.020 s^{-1}; Table 2.2). The dissociation rate decreased 23-fold (k_{dis} = 0.087 ± 0.020 s^{-1}) when 20% DOPS was

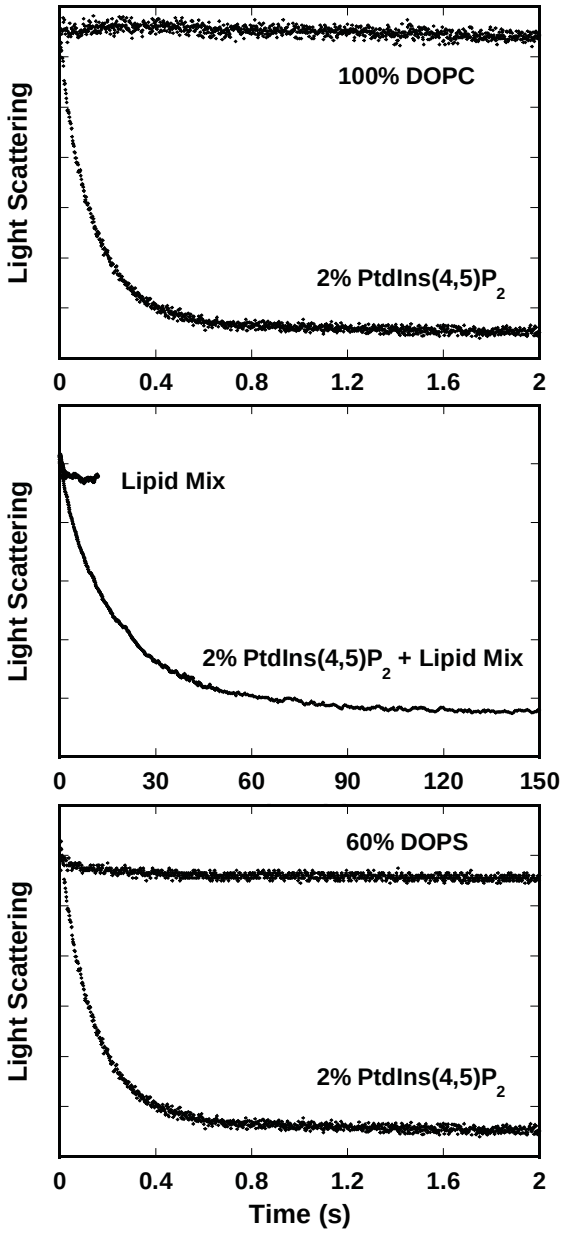

Figure 2.3 No change in light scattering upon mixing with $InsP_3$.

Pre-equilibrated solutions of 100 nM myo1c$^{IQ\text{-}tail}$ and LUVs (50 μM total lipid) were rapidly mixed with 25 μM $InsP_3$, and dissociation was measured as a decrease in light scattering. LUVs were composed of **(Top)** DOPC ± 2% PtdIns(4,5)P_2, **(Center)** Lipid Mix ± 2% PtdIns(4,5)P_2, and **(Bottom)** 60% DOPS or 2% PtdIns(4,5)P_2. See Table 2.1 for LUV compositions. Experimental time-courses (dots) are blank-subtracted averages of 3-8 traces. Concentrations are after mixing.

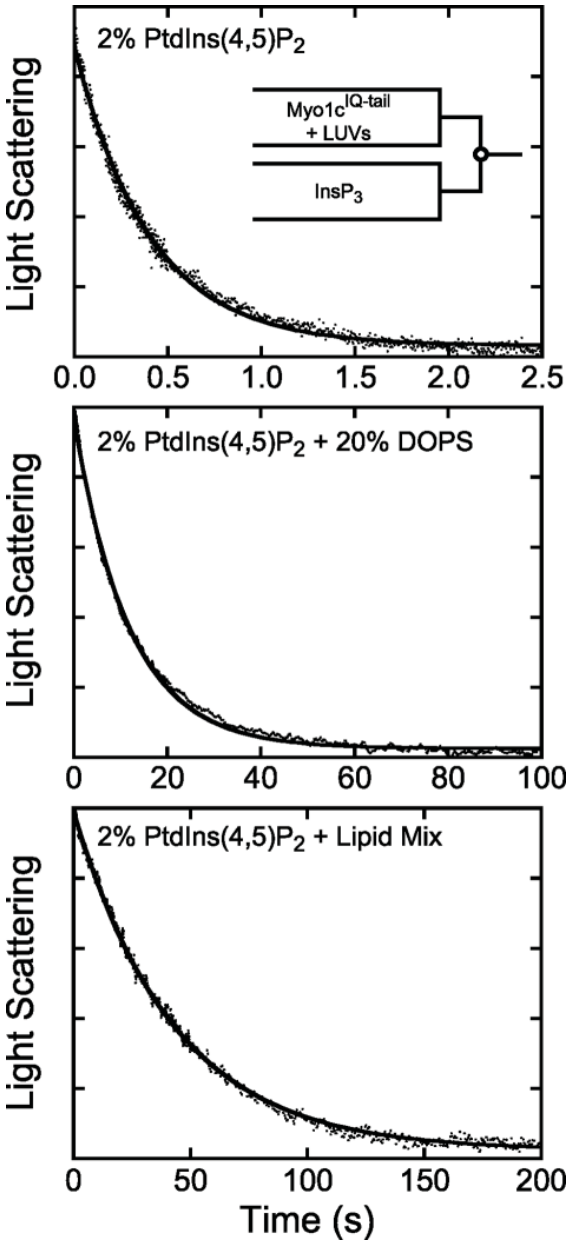

Figure 2.4 Dissociation of myo1c$^{IQ\text{-}tail}$ from phosphoinositide-containing LUVs.

Pre-equilibrated solutions of 100 nM myo1c$^{IQ\text{-}tail}$ and LUVs (50 μM total lipid) were rapidly mixed with 25 μM $InsP_3$, and dissociation was measured as a decrease in light scattering. LUVs were composed of **(Top)** 2% PtdIns(4,5)P_2, **(Center)** 2% PtdIns(4,5)P_2 + 20% DOPS, and **(Bottom)** 2% PtdIns(4,5)P_2 + Lipid Mix (Table 2.1). Experimental time-courses (dots) are blank-subtracted averages of 2-8 traces. The solid line is the best fit of the data to a single exponential function. Concentrations are after mixing.

Table 2.2: Myo1c$^{IQ\text{-}tail}$ and PLCδ-PH Dissociation Rate Constants[a]

LUV Composition	Myo1c$^{IQ\text{-}tail}$ k_{dis} (s^{-1})	AEDANS-PLCδ-PH k_{dis} (s^{-1})
2% PtdIns(4,5)P_2	2.0 ± 0.3 (7)	13 ± 0.65 (3)
2% PtdIns(4,5)P_2 + 1 mM Mg^{2+}	5.8 ± 0.1 (2)	-
8% PtdIns(4,5)P_2	0.16 ± 0.020 (3)	-
2% PtdIns(4,5)P_2 + 20% PS	0.087 ± 0.020 (4)	6.2 ± 0.070 (2)
2% PtdIns(3,4,5)P_3	2.8 ± 1.0 (6)	-
2% PtdIns(3,4,5)P_3 + 1 mM Mg^{2+}	9.1 ± 5.1 (3)	-
2% PtdIns(4,5)P_2 + Lipid Mix	0.025 ± 0.0030 (3)	8.3 ± 0.72 (2)

[a]10 mM HEPES, pH 7.0, 100 mM NaCl, 1 mM EGTA, 1 mM DTT, 22 ± 0.10 °C. Experiments with myo1c$^{IQ\text{-}tail}$ included 1 μM calmodulin, and dissociation time courses were initiated by mixing with 25 μM $InsP_3$ (100 μM $InsP_3$ for 8% PtdIns(4,5)P_2 LUVs). Errors are the standard deviations. The numbers in parentheses indicate the number of averaged experiments.

included with 2% PtdIns(4,5)P_2 (Figure 2.4), and placement of 2% PtdIns(4,5)P_2 in a physiological lipid mix (Corbin *et al.*, 2004) that contained POPS, PI, POPE, POPC, and SM (2% PtdIns(4,5)P_2 + Lipid Mix) resulted in an even slower rate of myo1c$^{IQ\text{-}tail}$ dissociation (k_{dis} = 0.025 ± 0.0030 s^{-1}; Figure 2.4).

The large decrease in the rate of myo1c$^{IQ\text{-}tail}$ dissociation is striking especially considering that myo1c$^{IQ\text{-}tail}$ does not appreciably bind LUVs composed of Lipid Mix in the absence of PtdIns(4,5)P_2 (Figure 2.3). Likewise, the affinity of myo1c$^{IQ\text{-}tail}$ for LUVs composed of < 40% DOPS (no PtdIns(4,5)P_2) is low (Hokanson and Ostap, 2006). While myo1c$^{IQ\text{-}tail}$ does bind 60% DOPS LUVs (no PtdIns(4,5)P_2) (Hokanson *et al.*, 2006; Hokanson and Ostap, 2006), InsP_3 does not induce dissociation from these LUVs (Figure 2.3). Taken together, these results support a model in which myo1c membrane binding is mediated through two membrane binding sites within the myo1c$^{IQ\text{-}tail}$ (Hokanson *et al.*, 2006; Hokanson and Ostap, 2006) (Figure 2.9). The putative PH domain comprises the primary binding site and is phosphoinositide-specific. A secondary site binds anionic phospholipids via delocalized electrostatic interactions.

2.3.3 Dissociation of PLCδ-PH from PtdIns(4,5)P_2-containing LUVs is less affected than myo1c$^{IQ\text{-}tail}$ by the presence of additional anionic charge.

We compared the kinetics of myo1c$^{IQ\text{-}tail}$ dissociation from 2% PtdIns(4,5)P_2 LUVs with the kinetics of the well characterized phospholipase-C delta (PLCδ) PH domain (Lemmon *et al.*, 1995; Lemmon and Ferguson, 2001; Lemmon and Ferguson, 2001; Ferguson *et al.*, 1995). Because of the small size of this protein, dissociation of PLCδ-PH from 2% PtdIns(4,5)P_2 LUVs did not result in a large enough light scattering change

to be detected in our stopped-flow experiments (data not shown). Instead, we measured changes in fluorescence anisotropy of PLCδ-PH labeled with IAEDANS (AEDANS-PLCδ-PH) upon LUV dissociation.

The two reactive cysteine residues in PLCδ-PH were labeled with the fluorescent probe IAEDANS to yield approximately 0.9 probes per PLCδ-PH. AEDANS-PLCδ-PH unbound to LUVs are free to rotate in solution. Binding of AEDANS-PLCδ-PH to PtdIns(4,5)P_2 LUVs limits their rotation, resulting in an increased anisotropy when excited with polarized light.

Dissociation of AEDANS-PLCδ-PH from 2% PtdIns(4,5)P_2 LUVs followed a single-exponential time course (Figure 2.5, top) with a rate (13.0 $\pm$ 0.65 s^{-1}) that was faster than measured for myo1c$^{IQ\text{-}tail}$ (Table 2.2). Addition of 20% DOPS to 2% PtdIns(4,5)P_2 LUVs decreased the dissociation rate 2-fold (6.2 ± 0.070 s^{-1}), and placement of 2% PtdIns(4,5)P_2 in a physiological lipid mix slowed dissociation only 1.5-fold (8.3 ± 0.72 s^{-1}; Figure 2.5, Table 2.2). Thus, the effect of additional anionic charge on the AEDANS-PLCδ-PH dissociation rate was substantially smaller than observed for myo1c$^{IQ\text{-}tail}$, which is consistent with a single phosphoinositide-specific binding site (Ferguson *et al.*, 1995). Measurements of the kinetics of AEDANS-PLCδ-PH association with 2% PtdIns(4,5)P_2 LUVs could not be determined due to the fast dissociation of AEDANS-PLCδ-PH from the LUVs.

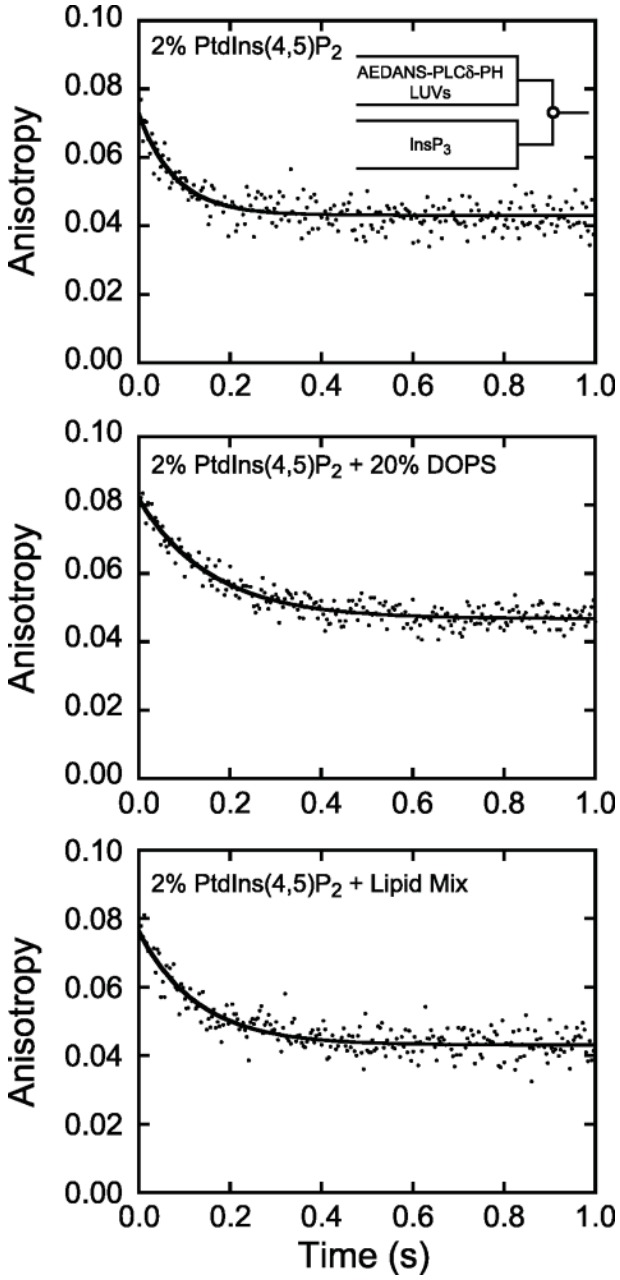

Figure 2.5 Dissociation of AEDANS-PLCδ-PH from LUVs.

AEDANS-PLCδ-PH (5 μM) pre-equilibrated with LUVs (1 mM total lipid) was rapidly mixed with 250 μM $InsP_3$, and dissociation was measured as a decrease in fluorescence anisotropy. LUVs were composed of **(Top)** 2% PtdIns(4,5)P_2, **(Center)** 2% PtdIns(4,5)P_2 + 20% DOPS, and **(Bottom)** 2% PtdIns(4,5)P_2 + Lipid Mix (Table 2.1). Experimental time-courses (dots) are the average of 2 - 3 individual traces. Solid lines are fits to a single exponential function. Concentrations are after mixing.

2.3.4 Soluble inositol phosphates induce myo1c$^{IQ\text{-}tail}$ dissociation from PtdIns(4,5)P_2-containing LUVs.

Control experiments to verify that increasing the soluble inositol phosphate concentration did not result in an increased amplitude change in light scattering, which would indicate incomplete dissociation of myo1c$^{IQ\text{-}tail}$ from LUVs, yielded a surprising result. As predicted by steady-state competition measurements (Hokanson *et al.*, 2006), the amplitudes of the dissociation transients show that > 6.3 µM InsP_6 completely displaces 100 nM myo1c$^{IQ\text{-}tail}$ from 50 µM 2% PtdIns(4,5)P_2 LUVs (Figure 2.6, top). Unexpectedly, however, the dissociation rates increased hyperbolically with increasing InsP_6 concentrations (Figure 2.6, top). Under these experimental conditions, this finding is inconsistent with a simple competitive binding mechanism, in which myo1c$^{IQ\text{-}tail}$ must first dissociate from phosphoinositide-containing LUVs prior to binding to InsP_6 (Scheme 1):

Scheme 1

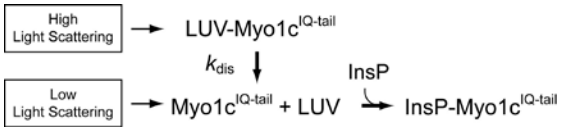

where, k_{dis} is a rate-limiting dissociation step.

We obtain the same results with InsP_3: the time courses of dissociation are similar for 6.3 – 25 µM InsP_3 compared with the same concentrations of InsP_6 (data not shown). We also performed control experiments to determine whether the increased dissociation rates were the result of increased ionic strength resulting from higher inositol phosphate concentrations. Additional sodium chloride was added so that the

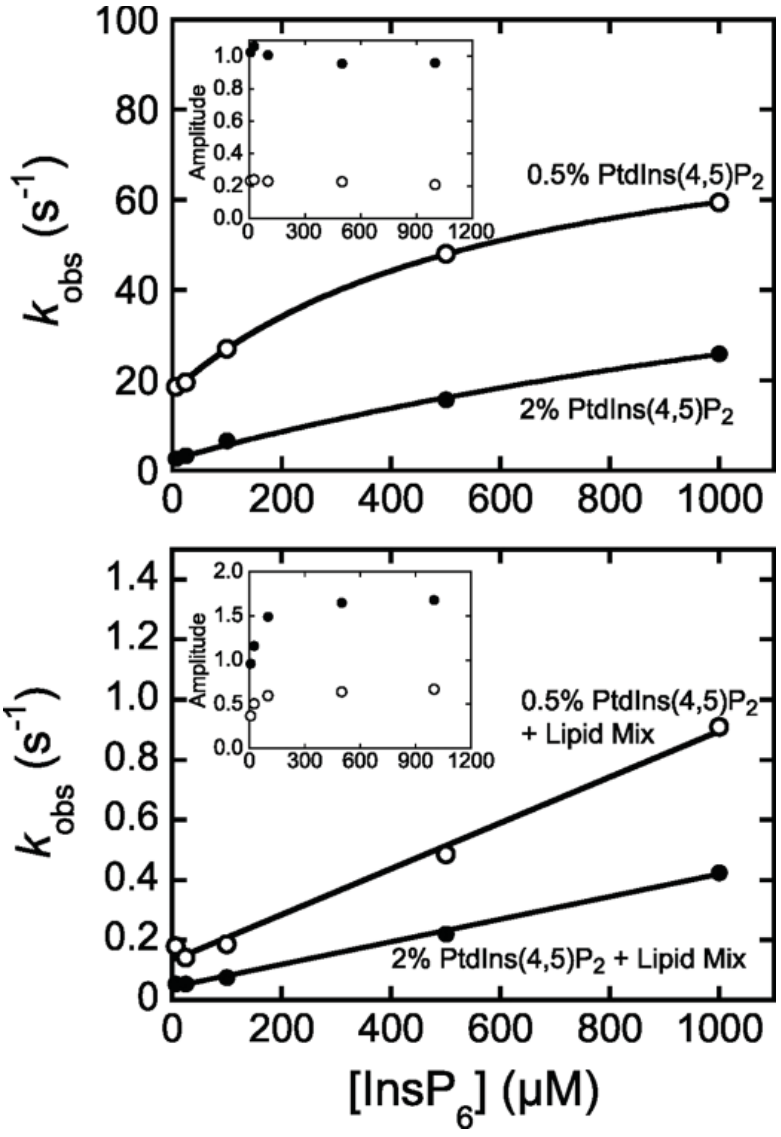

Figure 2.6 InsP_6-induced dissociation of myo1c$^{IQ\text{-}tail}$ from phosphoinositide-containing LUVs.

Pre-equilibrated solutions of myo1cIQ-tail and LUVs (50 μM total lipid) were rapidly mixed with 6.3 - 1000 μM InsP_6, and dissociation was measured as a decrease in light scattering. Myo1c$^{IQ\text{-}tail}$ concentration was 100 nM for 2% PtdIns(4,5)P_2 LUVs and 625 nM for all other LUVs. Points are the observed rates and **(insets)** amplitudes of the transients obtained by fitting to a single exponential function. LUVs were composed of (open symbols) 0.5% PtdIns(4,5)P_2 or (closed symbols) 2% PtdIns(4,5)P_2 in the **(Top)** absence or **(Bottom)** presence of Lipid Mix (Table 2.1). Each data point represents the average of 1 - 2 experiments (each the average of 3 - 5 transients). The solid lines are the best fits of the data to **(Top)** Eq.1 or **(Bottom)** a straight line with parameters reported in Table 1.4. Concentrations are after mixing.

calculated ionic strength at all inositol phosphate concentrations was the same. These control experiments indicate that the inositol-phosphate-induced rate increases are not the result of increases in ionic strength caused by the addition of $InsP_3$ or $InsP_6$ (data not shown).

Since the simplest model for dissociation of myo1c$^{IQ\text{-}tail}$ from 2% PtdIns(4,5)P_2 LUVs, the competitive binding mechanism shown in Scheme 1, was insufficient to account for the observed hyperbolic increase in the dissociation rate, we next considered a model in which myo1c$^{IQ\text{-}tail}$ dissociation occurs in two steps. A two-step dissociation may result from the two membrane-binding sites in the myo1c$^{IQ\text{-}tail}$. One of those sites is a putative pleckstrin homology domain that specifically binds certain phosphoinositides while the other site interacts with anionic phospholipids through non-specific electrostatic interactions (Hokanson *et al.*, 2006).

We therefore asked how dissociation of myo1c$^{IQ\text{-}tail}$ from PtdIns(4,5)P_2-containing LUVs was affected under conditions where the number of phosphoinositides bound to myo1c$^{IQ\text{-}tail}$ via non-specific electrostatic interactions was minimized. At a high myo1c$^{IQ\text{-}tail}$ to accessible PtdIns(4,5)P_2 ratio (5:1), $InsP_6$ completely displaces 0.63 µM myo1c$^{IQ\text{-}tail}$ from 50 µM 0.5% PtdIns(4,5)P_2 LUVs, as indicted by the amplitudes of the dissociation transients (Figure 2.6, top). Notably, the dissociation rates increase hyperbolically with the $InsP_6$ concentration substantially faster than measured in experiments using 2% PtdIns(4,5)P_2 LUVs (Figure 2.6, top).

We modeled the dissociation reaction according to a two-step dissociation model:

Scheme 2

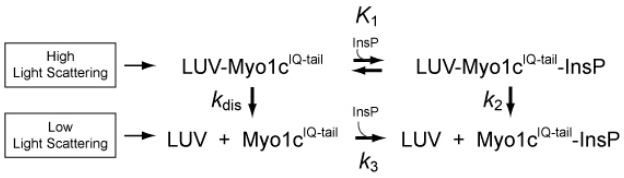

where, K_1 is the equilibrium constant for the binding of $InsP_6$ to LUV-bound myo1c$^{IQ\text{-}tail}$, k_2 is the rate of the $InsP_6$-induced dissociation step, k_3 is rapid $InsP_6$ binding to myo1c$^{IQ\text{-}tail}$, and k_{dis} is the rate of $InsP_6$-independent dissociation. Assuming K_1 is a rapid equilibrium step, and k_2, k_3, and k_{dis} are effectively irreversible in the presence of high concentrations of $InsP_6$, we fit the observed rates to:

Equation 1

$$k_{obs} = \frac{k_2[InsP_6]}{\frac{1}{K_1} + [InsP_6]} + k_{dis}$$

where k_{dis} is given by the *y*-intercept of the plot of k_{obs} vs. $InsP_6$ concentration (Figure 2.6). The K_1 values obtained by fitting the 2% PtdIns(4,5)P_2 dissociation data (K_1 = 420 ± 120 M^{-1}) is 4-fold smaller than found for 0.5% PtdIns(4,5)P_2 (K_1 = 1600 ± 170 M^{-1}), indicating that higher mole fractions of PtdIns(4,5)P_2 makes $InsP_6$ binding less favorable (Table 2.3). The k_2 values from 2% PtdIns(4,5)P_2 (k_2 = 79 ± 26 s^{-1}) and 0.5% PtdIns(4,5)P_2 (k_2 = 68 ± 2.9 s^{-1}), indicate that dissociation occurs rapidly upon $InsP_6$ binding (Table 2.3). The apparent second-order rate constant for $InsP_6$-induced dissociation is given by K_1k_2 and is 1.1 x 10^5 $M^{-1}s^{-1}$ for 0.5% PtdIns(4,5)P_2 and 3.3 x 10^4

Table 2.3: $InsP_6$-Induced-Dissociation Rate and Equilibrium Constants[a]

LUV Composition	K_1 (M^{-1})	k_2 (s^{-1})	k_{dis} (s^{-1})
0.5% PtdIns(4,5)P_2	1600 ± 170	68 ± 2.9	17 ± 0.40
2% PtdIns(4,5)P_2	420 ± 120	79 ± 26	2.8 ± 0.46
	K_1k_2 ($M^{-1}s^{-1}$)		
0.5% PtdIns(4,5)P_2 + Lipid Mix[b]	7.6×10^2		0.13
2% PtdIns(4,5)P_2 + Lipid Mix[c]	3.8×10^2		0.044

[a]10 mM HEPES, pH 7.0, 100 mM NaCl, 1 mM EGTA, 1 mM DTT, 1 μM calmodulin, 22 ± 0.10 °C.

Errors are the standard errors of the fits.

[b]Correlation coefficient for the linear fit equals 0.996.

[c]Correlation coefficient for the linear fit equals 0.999.

$M^{-1}s^{-1}$ for 2% PtdIns(4,5)P_2. The InsP_6-independent dissociation rates from 2% PtdIns(4,5)P_2 (k_{dis} = 2.8 ± 0.46 s^{-1}) and 0.5% PtdIns(4,5)P_2 (k_{dis} = 17 ± 0.40 s^{-1}) are consistent with the steady-state LUV affinities and association rate constants (see below).

We also measured the InsP_6-dependence of myo1c$^{IQ\text{-}tail}$ dissociation from LUVs that contained 0.5% and 2% PtdIns(4,5)P_2 in a physiological lipid mix (Figure 2.6, bottom). Slightly higher concentrations of InsP_6 were required to fully dissociate myo1c$^{IQ\text{-}tail}$ from the 2% PtdIns(4,5)P_2 + Lipid Mix LUVs (Figure 2.6, bottom), which is consistent with the higher affinity of myo1c$^{IQ\text{-}tail}$ for LUVs that contain additional anionic phospholipids (Hokanson *et al.*, 2006). Myo1c$^{IQ\text{-}tail}$ did not bind to LUVs + Lipid Mix when PtdIns(4,5)P_2 was omitted (F). Dissociation rates increased linearly with the InsP_6 concentration with no sign of a plateau. We were not able to experimentally achieve InsP_6 concentrations high enough to provide a good fit of the data to Equation 1. Rather, linear fits to the data give apparent second-order rate constants for InsP_6-induced dissociation for 2% PtdIns(4,5)P_2 + Lipid Mix (K_1k_2 = 3.8 x 10^2 $M^{-1}s^{-1}$) and 0.5% PtdIns(4,5)P_2 + Lipid Mix (K_1k_2 = 7.6 x 10^2 $M^{-1}s^{-1}$). If we assume that k_2 is similar to the value obtained above for 2% PtdIns(4,5)P_2 (Table 2.3), the values for K_1 in the presence of Lipid Mix are < 1 M^{-1}. The InsP_6-independent dissociation rates obtained from the *y*-intercepts for 2% PtdIns(4,5)P_2 + Lipid Mix (k_{dis} = 0.044 s^{-1}) and 0.5% PtdIns(4,5)P_2 + Lipid Mix (k_{dis} = 0.13 s^{-1}) are substantially slower than in the absence of Lipid Mix (Table 2.3).

2.3.5 Association of myo1c$^{IQ\text{-}tail}$ to PtdIns(4,5)P_2-containing LUVs is fast and relatively independent of additional anionic charge.

The time course of association of myo1c$^{IQ\text{-}tail}$ with 2% PtdIns(4,5)P_2 LUVs was obtained by monitoring changes in light scattering upon rapid mixing. The resulting transient increases in light scattering (Figure 2.7, top left) were best fit to a two-exponential function. The average amplitude of the faster of the two phases made up > 70% of the total amplitude change. The rates of the fast phase (k_{fast}) increased linearly with the lipid concentration (50 – 300 μM), and there was no evidence of a plateau (Figure 2.7). The rates of the slow phase (k_{slow} = 0.8 - 5.1 s^{-1}) were much less sensitive to the lipid concentration (Figure 2.7). Control experiments in which of myo1c$^{IQ\text{-}tail}$ was mixed with 100% DOPC LUVs did not show a transient change in light scattering (Figure 2.3).

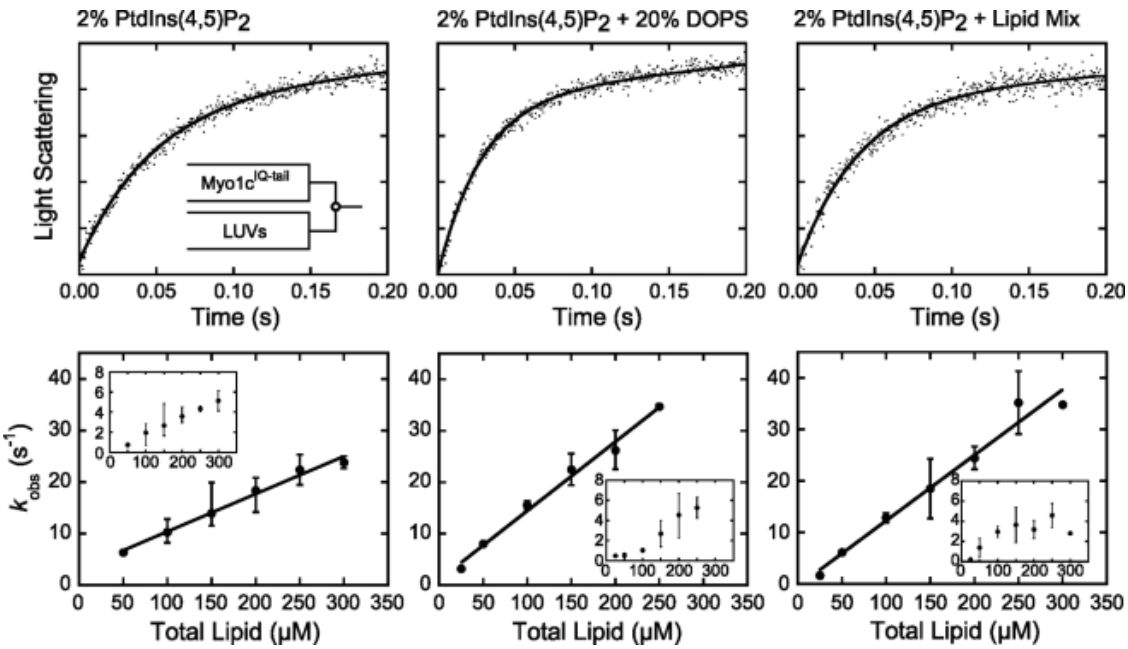

Figure 2.7 Association of myo1c$^{IQ\text{-}tail}$ with LUVs.

Myo1c$^{IQ\text{-}tail}$ was rapidly mixed with LUVs composed of **(Left)** 2% PtdIns(4,5)P_2, **(Center)** 2% PtdIns(4,5)P_2 + 20% DOPS, and **(Right)** 2% PtdIns(4,5)P_2 + Lipid Mix (Table 2.1). **(Top)** Experimental time-courses of light scattering changes after mixing myo1c$^{IQ\text{-}tail}$ with LUVs. Time courses (dots) are blank-subtracted averages of traces at final reaction concentrations of 250 nM myo1c$^{IQ\text{-}tail}$ and 250 μM total lipids. Solid lines are the best fits of the data to a two-exponential function. **(Bottom)** The rates of k_{fast} (closed symbols) and k_{slow} **(inset)** are plotted as a function of total lipid concentration. Each data point represents the average of 1 - 4 experiments (each the average of 2 – 6 transients), and the error bars report the range of values. The solid lines represent linear fits to the data.

The apparent second-order rate constant for myo1c$^{IQ\text{-}tail}$ binding to LUVs was determined by plotting the rates of the fast phase (k_{fast}) as a function of total lipid concentration (Figure 2.7) by assuming the mechanism in Scheme 3:

Scheme 3

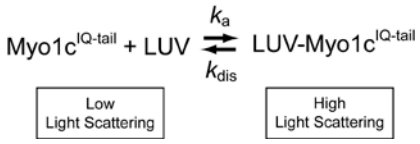

where, k_a and k_{dis} are the association and dissociation rate constants, respectively.

A linear fit to the data (Figure 2.7, bottom left) yields an association rate constant $k_{a\text{-}total}$ = 7.3 (±0.90) x 10^4 $M^{-1}s^{-1}$ in terms of total lipid concentration and $k_{a\text{-}LUV}$ = 5.2 (±0.70) x 10^9 $M^{-1}s^{-1}$ in terms of total LUV concentration. The calculated k_{dis}, given by the *y*-intercept (3.0 ± 1.7 s^{-1}; Table 2.4), is consistent with the $InsP_6$-independent dissociation rate measured above (Table 2.3). Increasing the mole percentage of PtdIns(4,5)P_2 from 2% to 8%, adding 20% PS, or placing 2% PtdIns(4,5)P_2 in a physiological lipid mix increased association rate constants less than 2-fold (Figure 2.7, Table 2.4). Increasing the negative charge in the LUVs also resulted in decreased values of the *y*-intercept, consistent with the dissociation measurements above (Table 2.4). This further supports our finding that the dissociation of myo1c$^{IQ\text{-}tail}$ from PtdIns(4,5)P_2-containing LUVs is slowed by the presence of additional anionic charge.

2.3.6 Dissociation of $InsP_3$ from myo1c$^{IQ\text{-}tail}$

Myo1c binds $InsP_3$ with high affinity (Hokanson *et al.*, 2006). To measure the rate of $InsP_3$ dissociation from myo1c$^{IQ\text{-}tail}$ we rapidly mixed 2% PtdIns(4,5)P_2 LUVs (0.6

Table 2.4: Myo1c$^{IQ\text{-}tail}$ Association Rate Constants[a]

LUV Composition	$k_{a\text{-}total}$ (x 10^4 $M^{-1}s^{-1}$)	$k_{a\text{-}LUV}$ (x 10^9 $M^{-1}s^{-1}$)	*y*-intercept (s^{-1})
2% PtdIns(4,5)P_2	7.3 ± 0.90	5.2 ± 0.70	3.0 ± 1.7
2% PtdIns(4,5)P_2 + 1 mM Mg^{2+}	3.0 ± 1.1	2.2 ± 0.90	6.9 ± 2.1
8% PtdIns(4,5)P_2	13 ± 2.2	13 ± 2.1	-0.65 ± 4.2
2% PtdIns(4,5)P_2 + 20% PS	13 ± 0.90	14 ± 1.0	1.5 ± 1.5
2% PtdIns(3,4,5)P_3	10 ± 1.0	4.9 ± 0.50	2.03 ± 1.73
2% PtdIns(3,4,5)P_3 + 1 mM Mg^{2+}	7.0 ± 1.3	3.5 ± 0.60	4.0 ± 2.8
2% PtdIns(4,5)P_2 + Lipid Mix	13 ± 1.5	15 ± 1.7	-0.64 ± 2.58

[a]10 mM HEPES, pH 7.0, 100 mM NaCl, 1 mM EGTA, 1 mM DTT, 1 μM calmodulin, 22 ± 0.10 °C. Errors are standard errors of the fits.

mM total lipid) with 0.25 µM myo1c$^{IQ\text{-}tail}$ pre-incubated with 0.5 µM $InsP_3$. Since $InsP_3$ and PtdIns(4,5)P_2 compete for a binding site on myo1c$^{IQ\text{-}tail}$ (Hokanson *et al.*, 2006), the rate of myo1c$^{IQ\text{-}tail}$ binding to 2% PtdIns(4,5)P_2 LUVs as determined by the transient increase in light scattering should be limited by the rate of $InsP_3$ dissociation at high LUV concentrations as shown in Scheme 4:

Scheme 4.

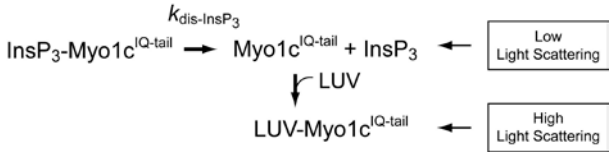

where $k_{dis\text{-}InsP3}$ is the rate constant for dissociation of $InsP_3$ from myo1c$^{IQ\text{-}tail}$.

The very high lipid concentration resulted in variable light scattering artifacts in the early time points, so points below 150 ms were not included in the fits. We resolved a transient increase in light scattering that was best fit to a single exponential function with a rate of 2.2 ± 0.029 s^{-1} (Figure 2.8), which is 20-fold slower than expected for direct binding of myo1c$^{IQ\text{-}tail}$ to 0.6 mM 2% PtdIns(4,5)P_2 LUVs (Table 2.4). Rather, we propose that the association rate is limited by $k_{dis\text{-}InsP3}$ (Scheme 4). A similar rate was also observed when myo1c$^{IQ\text{-}tail}$ was pre-incubated with $InsP_3$ and mixed with LUVs containing 2% PtdIns(4,5)P_2 + Lipid Mix ($k_{dis\text{-}InsP3}$ = 2.3 ± 0.031 s^{-1}; see Figure 2.8).

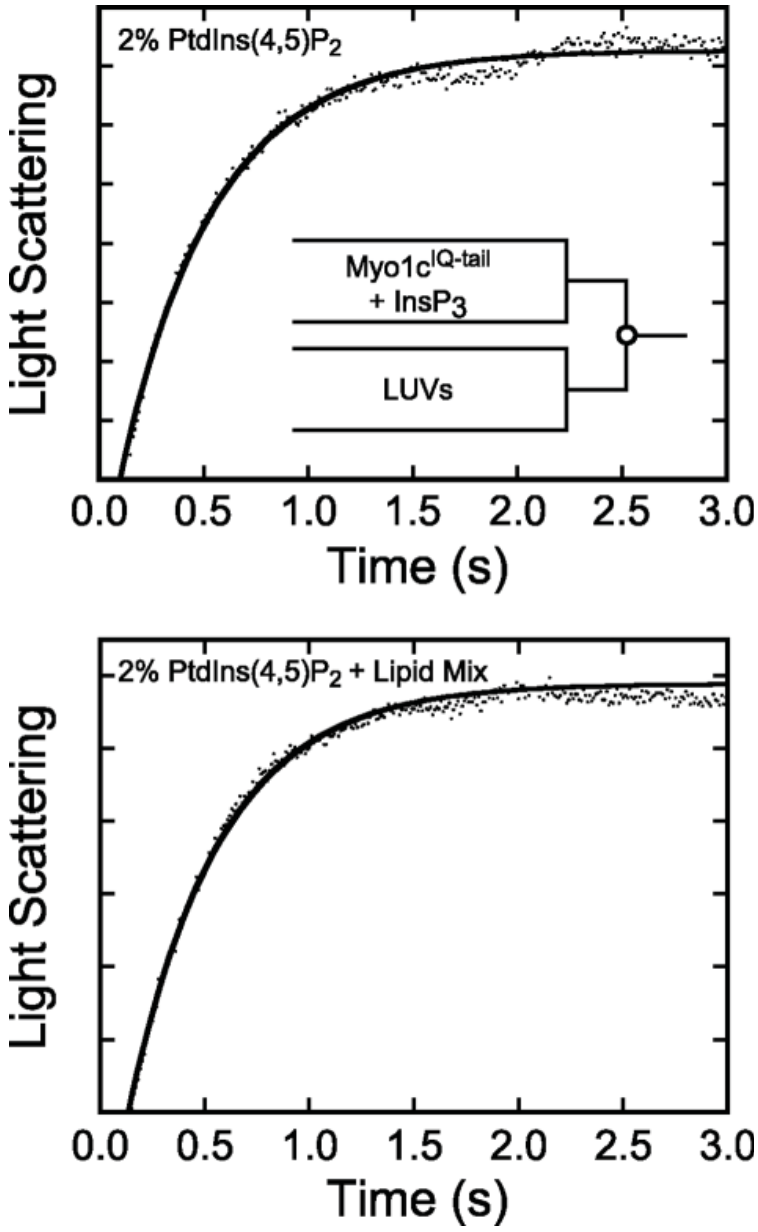

Figure 2.8 Dissociation of $InsP_3$ from myo1c$^{IQ\text{-}tail}$.

Myo1c$^{IQ\text{-}tail}$ (250 nM) pre-equilibrated with 500 nM $InsP_3$ was rapidly mixed with LUVs (600 μM total lipid) composed of **(Top)** 2% PtdIns(4,5)P_2, and **(Bottom)** 2% PtdIns(4,5)P_2 + Lipid Mix (Table 2.1). Myo1c$^{IQ\text{-}tail}$ association with LUVs was measured by light scattering. The first 150 ms of the time courses are not shown due to the presence of a mixing artifact. Experimental time-courses (dots) are the average of 3 - 4 blank-subtracted traces. Solid lines are fits to a single exponential function. Concentrations are after mixing.

2.3.7 Myo1c$^{IQ\text{-}tail}$ association and dissociation rates do not significantly differ for 2% PtdIns(4,5)P_2 and 2% PI(3,4,5)P_3 LUVs.

Hokanson et al. found that the myo1c$^{IQ\text{-}tail}$ is able to bind several different soluble inositol phosphates with high affinity, including the soluble headgroup of PtdIns(3,4,5)P_3 (Hokanson *et al.*, 2006). PtdIns(3,4,5)P_3 is an important signaling lipid and contains an additional phosphate, which could add to the energy of binding. Therefore, we measured the kinetics of the association of myo1c$^{IQ\text{-}tail}$ with PtdIns(3,4,5)P_3. We found that myo1c$^{IQ\text{-}tail}$ associates with 2% PtdIns(3,4,5)P_3 LUVs with a similar association rate constant as to 2% PtdIns(4,5)P_2 LUVs (Table 2.2). In addition, the rate of dissociation of myo1c$^{IQ\text{-}tail}$ from 2% PtdIns(3,4,5)P_3 LUVs (k_{dis} = 2.8 ± 1.0 s^{-1}) was similar to 2% PtdIns(4,5)P_2 LUVs (Table 2.4). Therefore, the phosphate on the 3 position of the inositol ring does not affect the myo1c$^{IQ\text{-}tail}$ binding, which is consistent with the results of steady-state measurements of binding to soluble inositol phosphates (Hokanson *et al.*, 2006).

Magnesium binds PtdIns(4,5)P_2 in DOPC vesicles (Toner *et al.*, 1988), and it has been shown to affect the binding of polyphosphoinositide-specific proteins (Dove *et al.*, 2004). Therefore, we measured myo1c$^{IQ\text{-}tail}$ dissociation and association in the presence of 1 mM Mg^{2+} and found that it slightly increases the rate of myo1c$^{IQ\text{-}tail}$ dissociation from 2% PtdIns(4,5)P_2 and 2% PtdIns(3,4,5)P_3 LUVs. Magnesium also slightly decreases the rate of association (Tables 2.4).

2.4 DISCUSSION

2.4.1 Positive charges in myo1c$^{IQ\text{-}tail}$ contribute to membrane binding and slow dissociation in the presence of anionic lipids

Myo1c$^{IQ\text{-}tail}$ dissociates from 2% PtdIns(4,5)P_2 LUVs at a rate that is 6.5-fold slower than AEDANS-PLCδ-PH. Additionally, the dissociation rate of myo1c$^{IQ\text{-}tail}$ decreases up to 80-fold when the mole fraction of anionic phospholipid in the LUVs is increased, which is not the case for AEDANS-PLCδ-PH dissociation (Table 2.2) or the dissociation of the glycine-rich protein 1 (GRP1) PH domain from PtdIns(3,4,5)P_3 (Corbin *et al.*, 2004). The lipid-dependent kinetic differences between myo1c$^{IQ\text{-}tail}$ and these other PH domains are likely due to membrane-binding regions outside of the myo1c PH domain. Specifically, previous work has suggested that the positively charged myo1c regulatory domain binds to anionic phospholipids as a secondary membrane attachment site (Hokanson *et al.*, 2006; Hirono *et al.*, 2004; Collins and Swanljung-Collins, 1992). The binding affinity of the regulatory domain interaction for anionic phospholipids does not appear to be high enough to drive membrane binding or confer phosphoinositide specificity (Hokanson *et al.*, 2006; Hokanson and Ostap, 2006). However, once myo1c is bound to the membrane via the phosphoinositide binding site, the secondary membrane binding site substantially increases the lifetime of membrane attachment (Table 2.2). It is an intriguing possibility that once myo1c is bound to the membrane, it remains attached via the secondary binding site, allowing PtdIns(4,5)P_2 to dynamically bind and detach from the myo1c PH domain (see below).

2.4.2 Soluble inositol phosphates induce membrane dissociation of myo1c$^{IQ\text{-}tail}$

Three independent measurements for the basal rate of dissociation of myo1c from 2% PtdIns(4,5)P_2 LUVs produced consistent values, supporting our assertion that k_{dis} in Scheme 2 reflects InsP_6-independent dissociation of myo1c$^{IQ\text{-}tail}$ and that inositol phosphates induce dissociation. First, knowing the steady-state dissociation constant (K_d = 23 μM; (Hokanson *et al.*, 2006)) and the association rate constant ($k_{a\text{-}total}$ = 7.3 x10^4 $M^{-1}s^{-1}$; Table 2.4) for the interaction of myo1c$^{IQ\text{-}tail}$ with 2% PtdIns(4,5)P_2 LUVs, the dissociation rate can be calculated (k_{dis} = 1.7 s^{-1}). This rate is consistent with the basal dissociation rates obtained from the *y*-intercepts of a plot of the observed association rate as a function of lipid concentration (k_{dis} = 3.0 ± 1.7 s^{-1}; Figure 2.7, bottom left; Table 2.4) and of a plot of the observed rate of dissociation as a function of inositol phosphate concentration (k_{dis} = 2.8 ± 0.46 s^{-1}; Figure 2.6, top; Table 2.3). Therefore, in the absence of inositol-phosphate-induced dissociation, the basal detachment rate from 2% PtdIns(4,5)P_2 LUVs is ~ 2 s^{-1}. The basal detachment rates are highly dependent on the overall charge of the LUVs, with dissociation rates > 50-fold slower in the presence of additional anionic membranes (Tables 2.2 and 2.3).

Increasing the InsP_6 concentration hyperbolically increases the dissociation rate of myo1c$^{IQ\text{-}tail}$ from LUVs above the basal rate in LUVs that contain phosphoinositides. The simplest model that describes both the enhanced dissociation rate and the hyperbolic dependence is given in Scheme 2 and Equation 1. The equilibrium constant, K_1, describes the accessibility of the InsP_6 binding site. K_1 is modeled as a rapid equilibrium step, meaning that k_{+1} and k_{-1} are much greater than k_2. If K_1 was not a rapid equilibrium step, light scattering time courses would follow a two-exponential rate

process. Strikingly, increased mole percentages of anionic phospholipid result in decreased values of K_1, which range from 1600 M^{-1} with LUVs that contain 0.5% PtdIns(4,5)P_2 to < 1 M^{-1} with LUVs that contain PtdIns(4,5)P_2 plus Lipid Mix. Despite this large range, the key conclusion that phosphoinositides are able to bind and unbind to myo1c^{IQ}-tail while the protein remains associated with the membrane has important functional implications (see below).

2.4.3 Association of myo1c$^{IQ\text{-}tail}$ with lipid vesicles is fast and approaches diffusion-limited conditions

The apparent second-order rate constant for membrane association is fast and increases less than 2-fold in the presence of additional anionic phospholipids (Table 2.4). The rate of binding approaches the diffusion-limit when calculated in terms of LUV concentration (Table 2.4), which is consistent with previous measurements of binding to LUVs composed of only DOPC and DOPS (Tang and Ostap, 2001). It should be noted that this result is different from kinetic measurements of the binding of the PH domain from GRP1 to PtdIns(3,4,5)P_3, which has ~6-fold increase in its association rate upon inclusion of additional anionic phospholipids (Corbin *et al.*, 2004). It was proposed for the PH domain from GRP1 that non-specific electrostatic interactions between the PH domain and additional anionic phospholipids facilitate the binding of the PH domain to phosphoinositides (Corbin *et al.*, 2004). It is possible that myo1c follows a similar two-step pathway, except that non-specific electrostatic interactions between the regulatory domain and anionic phospholipids, including phosphoinositides, facilitate binding to the PH domain.

The slow phase of the myo1c$^{IQ\text{-}tail}$ association transients makes < 30% of the total amplitude change. The origin of the slow transition is not known, but it is possible that k_{slow} reports the rate of a conformational change in the myo1c$^{IQ\text{-}tail}$-LUV complex after binding. It is also possible that this slow kinetic phase is the result of restricted access of myo1c$^{IQ\text{-}tail}$ to LUVs already occupied with protein. Further spectroscopic experiments are required to resolve this issue.

2.4.4 Magnesium affects myo1c$^{IQ\text{-}tail}$ dissociation and association kinetics

The presence of 1 mM Mg^{2+} decreases the association and increases the dissociation rate constants of myo1c$^{IQ\text{-}tail}$ – LUV interactions (Tables 2.2 and 2.4), but it does not do so in a manner that results in increased specificity for either 2% PtdIns(4,5)P_2 or 2% PtdIns(3,4,5)P_3. It has been shown that Mg^{2+} binds weakly to the head group of PtdIns(4,5)P_2 (Toner *et al.*, 1988). Thus, Mg^{2+} likely competes with myo1c$^{IQ\text{-}tail}$ for LUV binding, resulting in decreased apparent association rate constants (Table 2.4). The 3-fold increased rates of dissociation are likely due to the binding of Mg^{2+} to the phosphoinositides that are not bound to myo1c$^{IQ\text{-}tail}$, reducing the electrostatic interaction between these lipids and positive charges outside of the myo1c PH domain. It is unlikely that the effect of Mg^{2+} is due to its binding to calmodulin. Although Mg^{2+} binds weakly to calmodulin, this binding has little effect on the overall structure of calmodulin, as determined through nuclear magnetic resonance, since Mg^{2+} does not bind critical residues in the EF-loop (Ohki *et al.*, 1997; Gifford *et al.*, 2007). Furthermore, if Mg^{2+} binding to calmodulin exposed the positively-charged residues of the myo1c$^{IQ\text{-}tail}$ IQ motifs, the affinity of the myo1c$^{IQ\text{-}tail}$ for LUVs would likely increase. An

increase in affinity would result from an increase in the association rate, a decrease in the dissociation rate, or both.

2.4.5 Relationship of myo1c$^{IQ\text{-}tail}$ membrane binding kinetics to the biochemical properties of the motor

When considering the mechanical activity of myo1c when bound to lipid membranes, it is important to consider how the rate of membrane dissociation relates to the actin attachment time during ATPase cycling. Under unloaded conditions, the maximum actin-activated ATPase rate of myo1c is ~3 s^{-1} (Manceva *et al.*, 2007) which is similar to the basal rate of dissociation from 2% PtdIns(4,5)P_2 LUVs (k_{dis} = 2.0 ± 0.30 s^{-1}). Thus, there is a significant probability that myo1c would dissociate from a membrane of this composition before completing a catalytic cycle. However, the dissociation rate from membranes containing a more physiological lipid mix is substantially slower than the catalytic cycle, and myo1c could undergo multiple catalytic cycles before dissociating. It is important to point out that multiple proteins have recently been identified that bind myo1c, including RalA (Chen *et al.*, 2007), pleckstrin homology domain retinal protein 1 (PHR1) (Etournay *et al.*, 2005), NF-κB essential modulator (NEMO) (Nakamori *et al.*, 2006), calcium-binding protein 1 (CaBP1) (Tang *et al.*, 2007), and calcium- and integrin-binding protein 1 (CIB1) (Tang *et al.*, 2007), and these proteins may play a role in increasing the lifetime of the attachment of myo1c to the membrane and may anchor myo1c for force generation.

2.4.6 Cellular implications of myo1c$^{IQ\text{-}tail}$'s membrane binding kinetics

Phosphoinositide binding via the putative PH domain in the tail appears to be crucial for the membrane localization of myo1c in certain epithelial cell lines (Hokanson *et al.*, 2006), and may also be important for its localization in other cell types (Hirono *et al.*, 2004). It is not known if phosphoinositide binding has cellular roles distinct from the spatial regulation of myo1c localization. However, an intriguing possibility is that once bound to phosphoinositides, myo1c concentrates these lipids to regions of high actin concentration, similar to the lateral sequestration of PtdIns(4,5)P_2 by the myristoylated alanine-rich protein kinase C substrate (MARCKS) protein (McLaughlin and Murray, 2005). While there are other proteins in the cell that bind phosphoinositides, high local concentrations of myo1c could sequester PtdIns(4,5)P_2 in a given region of the cell since PtdIns(4,5)P_2 that has dissociated from one myo1c molecule could bind to a nearby myo1c.

Given the high concentrations of soluble inositol phosphates required to accelerate dissociation (Figure 2.6), it is unlikely that soluble inositol-phosphate-induced dissociation is a physiologically relevant dissociation mechanism. Rather, this experimental phenomenon suggests that the phosphoinositide binding site on myo1c$^{IQ\text{-}tail}$ is transiently unoccupied while the protein is membrane bound. Therefore, myo1c may remain attached to the membrane via the secondary binding site, while phosphoinositides are free to dissociate from its PH domain and interact with and activate other phosphoinositide binding proteins. Thus, actin-bound myo1c may act as a "pipmodulin" (Gambhir *et al.*, 2004; McLaughlin and Murray, 2005; Laux *et al.*, 2000), in that it may spatially control the amount of free PtdIns(4,5)P_2 available for phosphoinositide-activated proteins. Given the predicted importance of

phosphoinositides in regulating the formation and dynamics of actin-rich structures (Insall and Weiner, 2001; Yin and Janmey, 2003; T. *et al.*, 2007; Kolsch *et al.*, 2008), it will be important to further examine the cellular and mechanical consequences of the myo1c-phosphoinositide interaction.

2.5 CONCLUDING REMARKS

2.5.1 Model for myo1c binding to phosphoinositide-containing membranes

Myo1c binds to anionic membranes containing PtdIns(4,5)P_2 through more than one binding site (Figure 2.9). This claim is supported by the finding that the observed dissociation rate of myo1c$^{IQ\text{-}tail}$ from PtdIns(4,5)P_2-containing LUVs is hyperbolically dependent upon the concentration of soluble inositol phosphates (Figure 2.6), as discussed in section 2.4.2 [Soluble inositol phosphates induce membrane dissociation of myo1c$^{IQ\text{-}tail}$]. In contrast to the PtdIns(4,5)P_2-binding domain of PLCδ, myo1c$^{IQ\text{-}tail}$ dissociation from PtdIns(4,5)P_2-containing LUVs is dramatically slowed by the presence of additional anionic lipids (Figure 2.4, Table 2.2) (Figure 2.9).

The primary binding site is the putative PH domain previously identified in the tail of myo1c (Hokanson *et al.*, 2006). Rather than mediating a purely electrostatic interaction with negatively-charged lipids, this site confers specificity for phosphoinositides with phosphates at the 4- or 5-positions in the inositol ring (Hokanson *et al.*, 2006). Notably, mutation of either of two important basic residues (K892 or R903) to alanine disrupts myo1c binding to PtdIns(4,5)P_2-containing LUVs *in vitro* and the plasma membrane *in vivo* (Hokanson *et al.*, 2006).

The secondary binding site interacts electrostatically with anionic phospholipids, including phosphoinositides. It does not, however, confer specificity for phosphoinositides, nor is it sufficient for the initial binding of myo1c to membrane (Hokanson *et al.*, 2006). This secondary site contributes substantially to the affinity of the myo1c-membrane interaction (steady-state data, (Hokanson *et al.*, 2006)), which is

primarily mediated through the putative PH domain, and dramatically increases the lifetime of membrane attachment (kinetic data, Figure 2.4, Table 2.2). Importantly, this secondary site could allow myo1c to remain bound to membrane while phosphoinositides in the membrane bind to and dissociate from the putative PH domain.

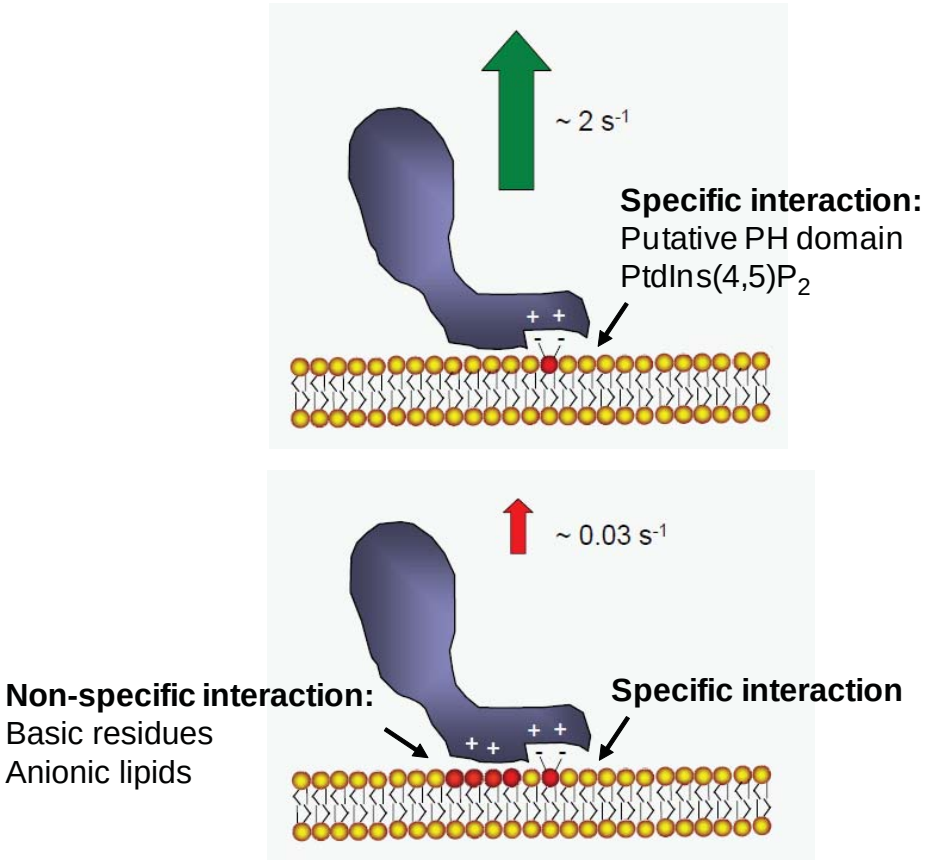

Figure 2.9 Positive charges in myo1c contribute to membrane binding and slow dissociation in the presence of anionic lipids.

(Top) The putative PH domain in the tail of myo1c binds phosphoinositides such as PtdIns(4,5)P_2 (red headgroup with negative charges). This interaction is sufficient for myo1c membrane association.

(Bottom) However, additional electrostatic interactions between positive charges in myo1c with anionic lipids (red headgroups) dramatically slow myo1c membrane dissociation (indicated by arrows). In addition, this secondary interaction site may allow the myo1c putative PH domain to bind and unbind phosphoinositides while myo1c remains associated with membrane.

2.5.2 Acknowledgments

We thank Dr. Paul Janmey for assistance with DLS measurements and Dr. Mark Lemmon for the PLCδ-PH domain construct. We are especially grateful to Dr. Serapion Pyrpassopoulos for helpful discussions and Tianming Lin for technical assistance. EMO was supported by a grant from the NIH (GM057247). JMDM was supported by a training grant from the NIH (GM07229) and from an American Heart Association predoctoral fellowship.

Chapter 3. Sites of glucose transporter-4 vesicle fusion with the plasma membrane correlate spatially with microtubules

A manuscript of this research is currently in preparation.

Dawicki McKenna JM, Goldman YE, Ostap EM. Sites of glucose transporter-4 vesicle fusion with the plasma membrane correlate spatially with microtubules.

3.1 BACKGROUND AND SUMMARY

The localization of glucose transporter-4 (GLUT4) to the plasma membrane is important for the insulin-stimulated uptake of glucose into fat and muscle. In adipocytes, vesicles containing GLUT4 (GLUT4 vesicles) redistribute from intracellular stores to the cell periphery in response to insulin stimulation. Vesicles then fuse with the plasma membrane, facilitating glucose transport into the cell. While the cytoskeleton is known to be involved in this important process, the role microtubules play is not understood at a mechanistic level. This chapter of my thesis focuses on the role of microtubules in the accumulation of GLUT4-containing vesicles at and fusion with the plasma membrane.

3.1.1 Specific Aims

While it is clear that microtubules are involved in GLUT4 vesicle motility, it is not clear if microtubule-based GLUT4 vesicle movement is required for the insulin-induced GLUT4 redistribution to the plasma membrane. Insulin may regulate GLUT4 vesicle engagement or movement along microtubules as suggested by work in 3T3-L1 adipocytes, in which the fraction of mobile vesicles and vesicle speed increased upon insulin stimulation (Fujita *et al.*, 2010). However, others observe a halting of vesicle trafficking along microtubules in response to insulin in primary rat adipocytes (Lizunov *et al.*, 2005). An absolute requirement for an insulin-stimulated increase in GLUT4 mobilization along microtubules has been challenged by experiments showing that expression of constitutively active Akt is sufficient even in the absence of an intact microtubule cytoskeleton to redistribute GLUT4 in response to insulin (Eyster *et al.*,

2006). Therefore, an understanding of the role of microtubules in this important process requires further investigation.

Specific Aim 1. How are microtubules organized in 3T3-L1 adipocytes and what are their dynamics?

Microtubules have been proposed to serve as tracks along which GLUT4 vesicles are transported to the surface in response to insulin. In addition, microtubules could influence the actin cytoskeleton, which is known to play a role in GLUT4 trafficking, through the localization of actin regulatory proteins such as the regulators of small GTPases, for example (Basu and Chang, 2007). It will be important, therefore, to determine the organization and dynamics of microtubules. This area has received surprisingly little investigation, even in studies analyzing GLUT4 vesicle motility. Most often, the locations of microtubules are presumed by the trajectories of GLUT4 vesicles moving long distances, with little information provided about the total population of microtubules or how their localization or dynamics might be affected by insulin. I address this question by examining the localization and dynamics of microtubules in 3T3-L1 adipocytes, the effect of insulin on microtubule distribution, and the temporal relationship between the effects of insulin on the microtubule cytoskeleton and on GLUT4 redistribution to the plasma membrane.

Specific Aim 2. How are microtubules, GLUT4 vesicles, and sites of fusion spatially and temporally related?

A greater understanding of how microtubules and microtubule motors influence GLUT4 mobilization, vesicle dynamics, and fusion is also required. In particular, the spatial relationship between microtubules, GLUT4 vesicles, and sites of fusion with the plasma membrane in living cells over time has not been adequately explored. Simultaneous imaging of microtubules and GLUT4 vesicle dynamics in live cells will provide important information about potential mechanisms for microtubules in GLUT4 trafficking. I have, therefore, examined the time course and extent of GLUT4 redistribution to the plasma membrane following microtubule disruption and the spatial relationship between microtubules, mobile GLUT4 vesicles, and sites of GLUT4 vesicle fusion with the plasma membrane.

3.1.2 Summary

To gain insight into the molecular role of microtubules in GLUT4 vesicle trafficking in response to insulin stimulation, we examined the spatial organization and dynamics of microtubules in relation to GLUT4 vesicle trafficking at the attached surface of 3T3-L1 adipocytes using total internal reflection fluorescence (TIRF) microscopy. We found that insulin stimulation increased the density of microtubules within the TIRF-illuminated region of the cell. The time course of the density increase preceded that of the increase in intensity of HA-GLUT4-eGFP in this same region. In addition, portions of the microtubules are highly curved and are pulled closer to the cell cortex, as confirmed by Parallax microscopy (Sun *et al.*, 2009). Nocodazole treatment to disrupt microtubules modestly reduced the insulin-stimulated increase in HA-GLUT4-eGFP intensity and

delayed the accumulation of GLUT4 at the plasma membrane, suggesting an impaired efficiency of GLUT4 translocation in the absence of microtubules. We detected fusion events and determined their spatial relationship to microtubules using a pH-sensitive GFP variant (pHluorin) fused to insulin-regulated aminopeptidase (IRAP), a protein that co-traffics with GLUT4. Interestingly, quantitative analysis revealed that fusions of GLUT4-containing vesicles with the plasma membrane preferentially occur near microtubules, and long-distance vesicle movement along microtubules visible at the cell surface prior to fusion does not appear to account for this proximity. We conclude that microtubules may be important in providing spatial information for fusion events, although they are not required for GLUT4 vesicle fusion.

3.2 MATERIALS AND METHODS

3.2.1 Reagents

Tissue culture reagents were from Gibco, except fetal bovine serum (FBS) and recombinant, human insulin, which were from Sigma. Nocodazole, cytochalasin D, and latrunculin B were obtained from both A.G. Scientific and Sigma. Radioimmuno assay-grade bovine serum albumin (RIA-BSA) (Calbiochem) was used for serum starvation.

3.2.2 Cloning and Constructs

For a schematic illustration of GLUT4 and IRAP constructs used see Figure 3.1. mCherry-IRAP-pHluorin (pJDM19) was constructed by inserting mCherry (Dr. R. Tsien (Shaner *et al.*, 2004)) prior to the N-terminal 393-bp fragment of IRAP in the IRAP-pHluorin construct (Dr. D. James (Jiang *et al.*, 2008)) using Nhe I and Bgl II restriction sites. PCR primers were used to generate restriction sites flanking mCherry lacking a stop codon: 5'- GAAGCTAGCGACCATGGTGAGCAAGGGCGAGGAGG -3'; 5'-TGCAAGATCTTCTTGTACAGCTCGTCCATGCC -3'. Site-directed mutagenesis was then used to correct a base insertion in the reverse primer: 5'-GACGAGCTGTACAAGAGATCTCGAGCCACC -3'; 5'-GGTGGCTCGAGATCTCTTGTACAGCTCGTC -3'. Sequences were confirmed using the dideoxy method.

HA-GLUT4-mCherry (pJDM12) was constructed by substituting mCherry for eGFP in the HA-GLUT4-eGFP construct (Dr. S. Cushman (Dawson *et al.*, 2001)) using KpnI and XbaI restriction sites. PCR primers were used to generate restriction sites

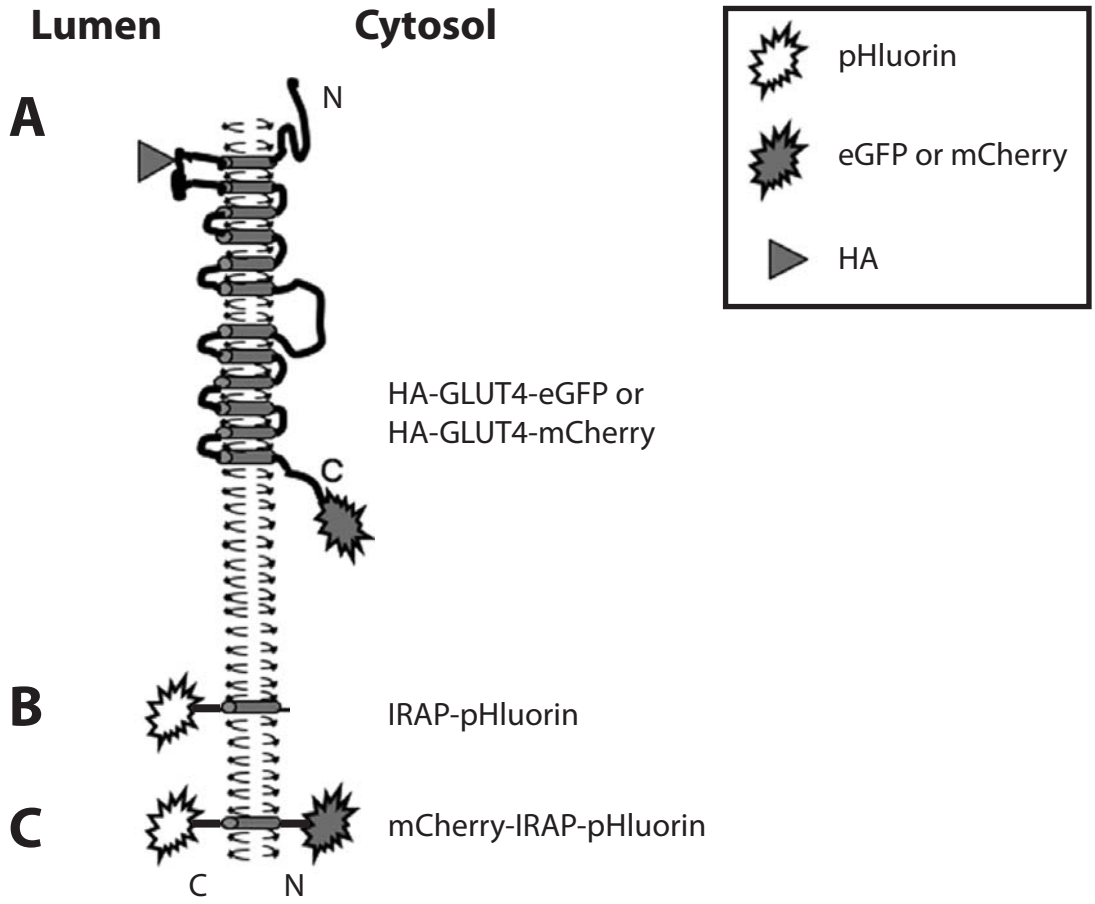

Figure 3.1 GLUT4 and IRAP constructs.

(A) GLUT4 constructs have a hemagglutinin epitope tag (HA) inserted between amino acids 67 and 68 in the first exofacial loop of human GLUT4. Either eGFP (Dawson et al. 2001) or mCherry has been fused to the C-terminus, which is cytosolic. N- and C-termini are indicated.

(B) To better detect GLUT4 vesicle fusions, the pH-sensitive fluorescent protein pHluorin has been fused to the C-terminus of amino acids 1-393 of IRAP (Jiang et al. 2008). pHluorin fluorescence is low in the acidic lumen of GLUT4 vesicles. When exposed to the neutral pH of the extracellular environment following vesicle fusion with the plasma membrane, pHluorin fluorescence increases. N- and C-termini are oriented as in **(C)**.

(C) mCherry has been fused to the N-terminus of IRAP-pHluorin **(B)** so that GLUT4 vesicles can be detected prior to fusion. N- and C-termini are indicated. Figure is adapted from (Shi, Huang & Kandror 2008).

flanking mCherry: 5'- GGGGTACCGCAATGGTGAGCAAGGGCGAGG -3'; 5'-GCACTCTAGATTACTTGTACAGCTCGTCCATGC -3'. Sequencing was confirmed using the dideoxy method.

3.2.3 Cell Culture, Transfection, and Live-cell Imaging

Mouse 3T3-L1fibroblasts (source: Dr. M. Birnbaum, University of Pennsylvania) were cultured in growth medium (high glucose (4.5 g/L) DMEM + 10% FBS supplemented with antibiotics) in a 37 °C, 5% CO_2 incubator. Fibroblasts were differentiated into adipocytes in differentiation medium (DMEM, 10% FBS, 0.5 mM isobutylmethylxanthine, 400 ng/mL dexamethasone, 400 nM insulin, and 10 µg/mL troglitazone) essentially as described (Garza and Birnbaum, 2000). Adipocytes were used at 6 – 10 days post-differentiation for live cell imaging or 7 – 14 days for fixed cell imaging. Morphologically, we considered cells with prominent lipid droplets to be adipocytes. These cells were generally more rounded than cells lacking lipid droplets, although adipocytes were somewhat less rounded following replating of the cells for imaging.

For transient transfection, 3T3-L1 adipocytes were trypsinized (0.25% trypsin-EDTA), washed twice, and resuspended in PBS without Ca^{2+} or Mg^{2+}. DNA and cells were added to a 0.4 cm electroporation cuvette in a final volume of ~700 µL. Cells were electroporated at 200 V, 950 µF and re-plated onto acid-washed coverslips. The amount of DNA used per transfection varied by construct: HA-GLUT4-eGFP, 80 µg; IRAP-pHluorin, 20 – 25 µg; eGFP-human-α-tubulin (Clontech), 40 µg; mCherry-human-α-tubulin (Dr. R. Tsien (Shaner *et al.*, 2004)), 40 µg; 3xGFP-EMTB (ensconsin

microtubule-binding domain) (Dr. C. Bulinski (Faire *et al.*, 1999)), 5 µg; mCherry-IRAP-pHluorin, 10 µg; GFP-CC1 $p150^{Glued}$ (Dr. E. Holzbaur (Mentlik *et al.*, 2010)), 60 µg. Cells were imaged 24 – 48 hours following transfection.

Prior to live-cell imaging, adipocytes were serum-starved for a minimum of 2 hours in either Krebs Ringer Phosphate buffer (136 mM NaCl, 4.7 mM KCl, 10 mM $NaPO_4$, pH 7.4, 0.49 mM $MgCl_2$, and 0.9 mM $CaCl_2$) + 0.2% RIA-BSA or high glucose DMEM + 0.5% RIA-BSA. Where indicated, cells were pre-treated with 10 µM nocodazole for a minimum of 20 minutes. Coverslips were then transferred to an enclosed Bioptechs chamber (Butler, PA), and the temperature was controlled at 37°C.

3.2.4 TIRF, Two-wavelength imaging, and Parallax microscopies

Live-cell imaging was conducted on one of two microscopes using total internal reflection fluorescence (TIRF) microscopy. For single wavelength imaging, a Leica DM IRB microscope was used with a Nikon 60x, Plan-apochromat 1.45 NA oil immersion objective and a Hamamatsu C4742-95 camera. A Melles Griot (Albuquerque, NM) 43 Series Ion Laser was used to excite the fluorophore at 488 or 514 nm. Imaging of two-wavelengths and 3-dimensional spatial imaging using Parallax microscopy (Sun *et al.*, 2009) were conducted on an inverted Nikon TE-2000U microscope with a Nikon 100x, Plan-achromat 1.49 NA oil immersion objective and a Photometrics Cascade-512B camera. Solid state 488-nm (Sapphire 488 LP, Coherent, Santa Clara, CA) and 561-nm (CrystaLaser, Reno, NV) lasers were used to excite eGFP and mCherry, respectively. Spectral separation of the emission was accomplished using a Dual-View (Photometrics, Tucson, AZ) system with an insert containing 565 dichroic, 580 LP, and 515/30 BP filters from Chroma (Bellows Falls, VT).

3.2.5 Live-cell Image Analysis

HA-GLUT4-eGFP and IRAP time courses

Differentiated cells transfected with HA-GLUT4-eGFP or IRAP-pHluorin were stimulated with starvation medium alone or starvation medium + 100 nM insulin. TIRF images were acquired at 1 frame per 10 s. Intensity within the initial cell footprint was measured at each time point, and measurements were background-subtracted. For evaluation of transient intensity changes, measurements were binned in 0.5 min intervals and intensity changes were calculated by dividing by the average intensity prior to insulin stimulation. The graph of intensity was normalized from 0, the average intensity prior to insulin addition, to 1, the average of the last minute of the plot. Cells scored as responding to insulin (fluorescence intensity increased by at least 10%) were averaged together, and the 95% confidence interval was calculated.

Microtubule curvature and density time course

Differentiated cells transfected with GFP-tubulin, mCherry-tubulin, or 3xGFP-EMTB were stimulated by the addition of 100 nM insulin. TIRF images were acquired at 1 frame per 10 s. A subset of cells was co-transfected with HA-GLUT4-eGFP and mCherry-tubulin for temporal correlation analysis, and a dual-view insert was used to spectrally separate the fluorescence emissions. For quantification of microtubule density (Figures 3.4B and 3.5A), images were background-subtracted in ImageJ (version 1.44c), and the intensity was thresholded to create a binary image of the microtubules. Density was measured by dividing the microtubule area determined from the binary image by the total cell area. For each trace, measurements were binned in 0.5 min intervals. Density

was normalized as described for HA-GLUT4-eGFP intensity, except that the average of the last 8 minutes was used for the final density value. Cells responding to insulin with a visible microtubule density increase were averaged together, and the 95% confidence interval was calculated.

For visualization and quantification of microtubule curvature (Figures 3.2 and 3.6A), images were background-subtracted, and microtubule contours were outlined by hand using a spline fit in ImageJ. The cosine correlation function was calculated for each contour at least 3 µm in length.

Cosine correlation function

To calculate the cosine correlation function, the microtubule was first divided into segments of length s (µm), and the angle theta (θ, rad) relative to the x-axis was determined for each segment. Any two segments are separated by a distance x (µm) along the contour of the microtubule. Their angles differ by a value delta $\theta = \theta_{Sn+x} - \theta_{Sn}$. Segments close to each other (i.e., x is small) will have similar values for theta, and the cosine of delta θ will be close to 1. However, when the contour distance between segments increases, the correlation between the two angles decreases.

When all values for $\cos(\theta_{Sn+x} - \theta_{Sn})$ for segments separated by a given distance x are averaged and plotted against x, the resulting cosine correlation function (CCF) decays with increasing x. How the CCF decays depends on the microtubule curvature. For a relatively straight microtubule (red), the CCF is nearly flat. For the curved microtubule (blue), $\langle\cos(\theta_{Sn+x} - \theta_{Sn})\rangle$ decays relatively rapidly toward 0. Calculations of $\langle\cos(\theta_{Sn+x} - \theta_{Sn})\rangle$ were limited to contour lengths of 0.45 times the filament length since

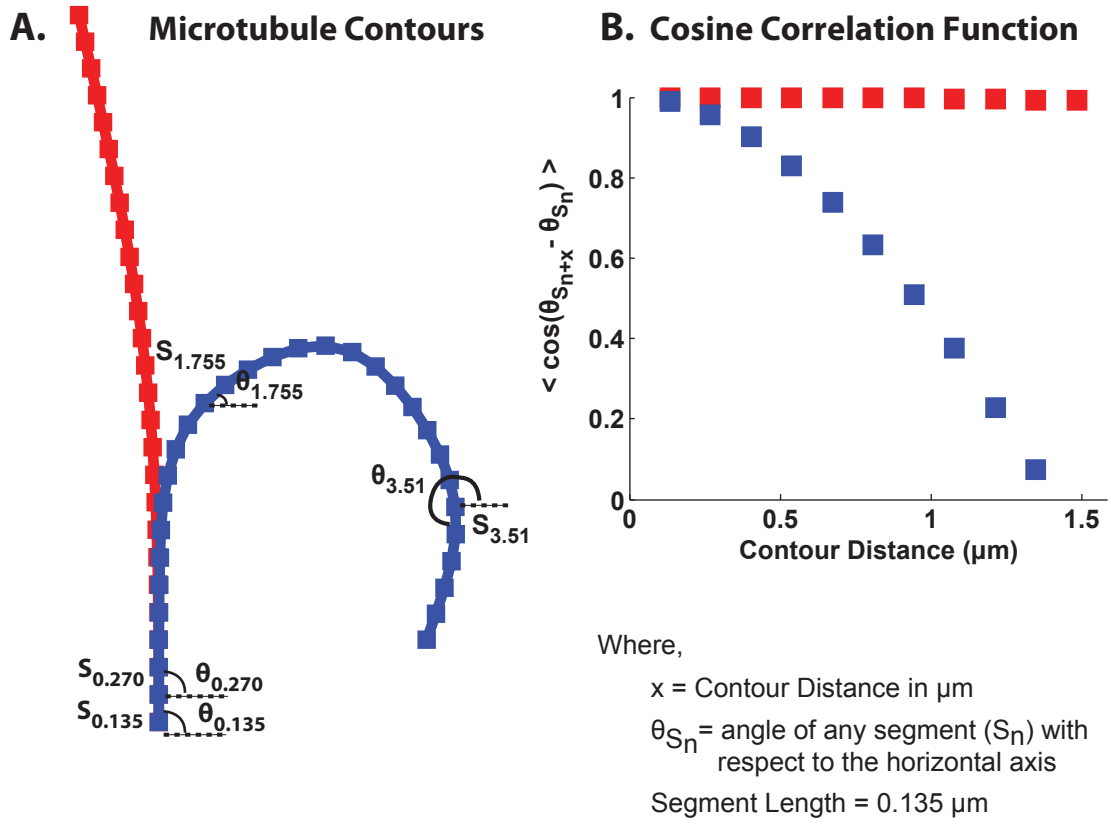

Figure 3.2 Microtubule contours and cosine correlation function.

(A) Contours for a straight **(red)** and curved **(blue)** microtubule from Figure 2.9 were replotted to share the same origin and initial orientation. Segments along the contour of the microtubule (s_n) make an angle (θ_{S_n}) with respect to the horizontal axis.

(B) Cosine correlation function for microtubule contours shown in **(A)**. $Cos(\theta_{S_{n+x}} - \theta_{S_n})$ was calculated for each pair of segments separated by contour distance x (μm), and values for all pairs were averaged.

the largest contour distances represent the average of just a few pairs of segments. See Figure 3.2.

Parallax and 3-dimensional imaging of microtubule

Differentiated cells were transfected with 3xGFP-EMTB. TIRF images were acquired at 1 frame per 10 s using Parallax microscopy (Sun *et al.*, 2009). Microtubule contours for each pair of images were obtained using NeuronJ (Meijering *et al.*, 2004) (Figure 3.9). Contours were divided into discrete segments, and the z-coordinate was calculated for each segment.

To calculate the z-coordinate, the effective z calibration factor, which relates the separation in y of a pair of images to the relative distance in z, was obtained as described (Sun *et al.*, 2009). Briefly, Invitrogen 540/560 beads were tracked while an oscillation was applied to the stage in the z-dimension. The change in separation in y between pairs of bead images was plotted against the stage position in z. The slope of the line yields the apparent calibration factor, which is multiplied by a focal shift ratio to get the effective z calibration factor.

To generate the Parallax movie (Movie 7), the z-coordinate for each segment of the microtubule contour was calculated for each of the 21 frames of the acquisition. To aid in visualization of the final movie, microtubule contours were interpolated in time so that between each pair of frames calculated from acquired images are inserted two frames of interpolated data.

Correlation of fusion locations with microtubules

Differentiated cells were co-transfected with IRAP-pHluorin and either mCherry-tubulin for quantification or 3xGFP-EMTB for visualization and stimulated with 100 nM insulin. TIRF images were acquired several minutes following insulin addition at 20 Hz, and a dual-view insert was used to spectrally separate the fluorescence emissions. IRAP-pHluorin fluorescence was scored as a fusion event if the fluorescence appeared during acquisition of the video sequence and dispersed within the plane of the membrane during subsequent frames. Microtubule intensity was thresholded as described above and skeletonized in ImageJ to create a 1-pixel line locating the microtubules. Fusion location was determined, and the distance of the fusion to the nearest microtubule location was calculated. Due to photobleaching, analysis was limited to the first ~15 s of the acquisition. To compare the distribution of fusion sites to a random distribution, 'mock' fusion locations (i.e., random locations) were randomly chosen within the area of the cell. Distance of the random location to the nearest microtubule location was calculated (n = 100 repetitions). Microtubule density was calculated by dividing the number of positive pixels in the binary image by the cell area. Cells were grouped according to microtubule density, and a cumulative distribution and histogram of the fraction of events occurring within a given distance from a microtubule were generated. Error bars for fusions represent the standard deviation resulting from bootstrapping (n = 100 repetitions) the data.

Vesicle movement prior to fusion

Differentiated cells transfected with mCherry-IRAP-pHluorin were stimulated with 100 nM insulin. TIRF images were acquired as described for the preceding section. Vesicle movements prior to fusion were scored as long-distance if the vesicle moved ~1 µm or more. Otherwise, vesicle movements were scored as not long-distance. Sometimes vesicles appeared to change velocity and direction repeatedly and rapidly, but these movements remained following nocodazole treatment, were less than 1 µm, and were judged not to be long-distance movements. When a fusion event could be detected but nearby vesicle density was too high, or mCherry fluorescence intensity was too dim, vesicle movements were scored as unknown.

Attempted disruption of microtubule dynamics

Differentiated cells transfected with GFP-tubulin or mCherry-tubulin were treated with 2 µM nocodazole during imaging or pre-treated with 1 µM cytoD or 20 µM latB for a minimum of 20 minutes prior to imaging. Alternatively, differentiated cells were co-transfected with mCherry-tubulin and GFP-CC1 $p150^{Glued}$. TIRF images were collected.

3.2.6 Immunofluorescence

The following primary antibodies were used for immunofluorescence of fixed cells: mouse monoclonal anti-tubulin clone DM1A, mouse monoclonal anti-acetylated tubulin antibody clone 6-11B-1, and pan-specific sheep anti-tubulin antibody (Cytoskeleton). Secondary antibodies were conjugated to Alexa 488 or Alexa 594 (Invitrogen/Molecular Probes).

For anti-α-tubulin staining (clone DM1A), cells were fixed in methanol + 1 mM EGTA pre-chilled to -20 °C for 10 minutes and permeabilized in PBS + 0.1% Igepal for 30 minutes at room temperature. For dual-staining of tubulin (pan-specific) and acetylated tubulin, cells were fixed in 4% paraformaldehyde in PBS for 15 minutes at room temperature and permeabilized in PBS + 0.1% Triton X-100 for 5 minutes at room temperature. Cells were blocked in PBS + 3% BSA. All antibodies were diluted in blocking buffer. Antibody incubations for anti-α-tubulin were 1 µg/mL for 1 hour at 37 °C for the primary and 1:500 for 1 hour at room temp for the Alexa 488-conjugated secondary. For dual-staining, primary antibodies were incubated sequentially first with anti-tubulin (1:100) overnight at 4 °C followed by anti-acetylated-tubulin (1:100) for 30 minutes at 37 °C. Secondary antibodies were used at 1:300 and incubated for 30 minutes at 37 °C. Samples were mounted in ProLong Gold Antifade Reagent (Invitrogen) and imaged using TIRF (anti-α-tubulin) or epifluorescence (dual-staining) microscopies.

3.2.7 MATLAB Routines Developed for Data Analysis

In this section I briefly describe the MATLAB scripts I developed for data analysis and presentation.

1. Time courses (Figures 3.3 - 3.5).

   MATLAB scripts to generate intensity time course data involved: defining the initial cell footprint through segmentation of images; calculating the cell intensity within this region for each frame; calculating background intensity of each frame and subtracting this from raw cell intensity. MATLAB scripts to process intensity and microtubule density time course data involved: binning in time; calculating fold

changes in intensity or density; normalizing time courses; averaging time courses. This semi-automated method of analyzing the data provided flexibility in processing large data sets.

2. Replotting microtubule contours for visualization (Figures 3.2 and 3.6).

   The MATLAB script involved calculating and applying a transform to the x,y-coordinates of the microtubule contours so that they share an origin and initial orientation.

3. Cosine correlation function (Figures 3.2 and 3.6).

   MATLAB scripts involved: dividing the microtubule contour into discrete segments of defined length; calculating the angle each segment makes with the x-axis; calculating cos(delta θ) for segments separated by a given contour length and averaging the values together; plotting <cos(delta θ)> as a function of contour length up to 0.45 the total contour length of the microtubule.

4. Parallax movie (Figure 3.9 and Movie 7).

   MATLAB scripts involved: calculating the effective z calibration factor from the positions of beads in pairs of images acquired during stage oscillation; calculating x,y,z-coordinates for discrete segments of a microtubule at each frame; generating a 3-dimensional color-coded plot for each frame; interpolating in time between frames to generate the final movie.

5. Fusion and microtubule correlation analysis (Figure 3.12).

   MATLAB scripts involved: calculating the distance of the center of fusion events to the nearest microtubule location in a binary image; randomly generating locations within the cell footprint for comparison of fusion locations to a random distribution of

locations; binning the calculated distances and generating a histogram of the data; calculating microtubule density.

3.3 RESULTS

3.3.1 3T3-L1 adipocytes redistribute GLUT4 in response to insulin

TIRF microscopy revealed a striking insulin-dependent movement of HA-GLUT4-eGFP from internal compartments to the coverslip-attached surface of adipocytes (Figure 3.3A; Movie 1). The average fluorescence intensity from cells that exhibited a > 10% enhancement (Figure 3.3B, inset) reached a plateau with a half-time ($t_{1/2}$) of 6.3 min (Table 3.1), which is similar to previously observed time courses (Huang *et al.*, 2007; Tengholm *et al.*, 2003; Gonzalez and McGraw, 2006). Control experiments, exchanging media without insulin, confirm that the fluorescence change is the result of the addition of insulin (Figure 3.4A).

3.3.2 Microtubule density increases in response to insulin stimulation in 3T3-L1 adipocytes

The density of microtubules within the TIRF illumination zone increased substantially upon insulin stimulation, as detected by the localization of mCherry-tubulin, GFP-tubulin, or 3xGFP-EMTB, the microtubule-binding domain of ensconsin (Figures 3.5A and 3.6A, Table 3.1, Movie 2). This intensity increase occurred with a half-time ($t_{1/2}$ = 2.5 min) that was 2.5-fold faster than the HA-GLUT4-eGFP intensity increase ($t_{1/2}$ = 6.3 min; Figure 3.5A; Table 3.1). The insulin-stimulated increase of microtubule density was also observed in cells co-expressing HA-GLUT4-eGFP and mCherry-tubulin (Figure 3.4B).

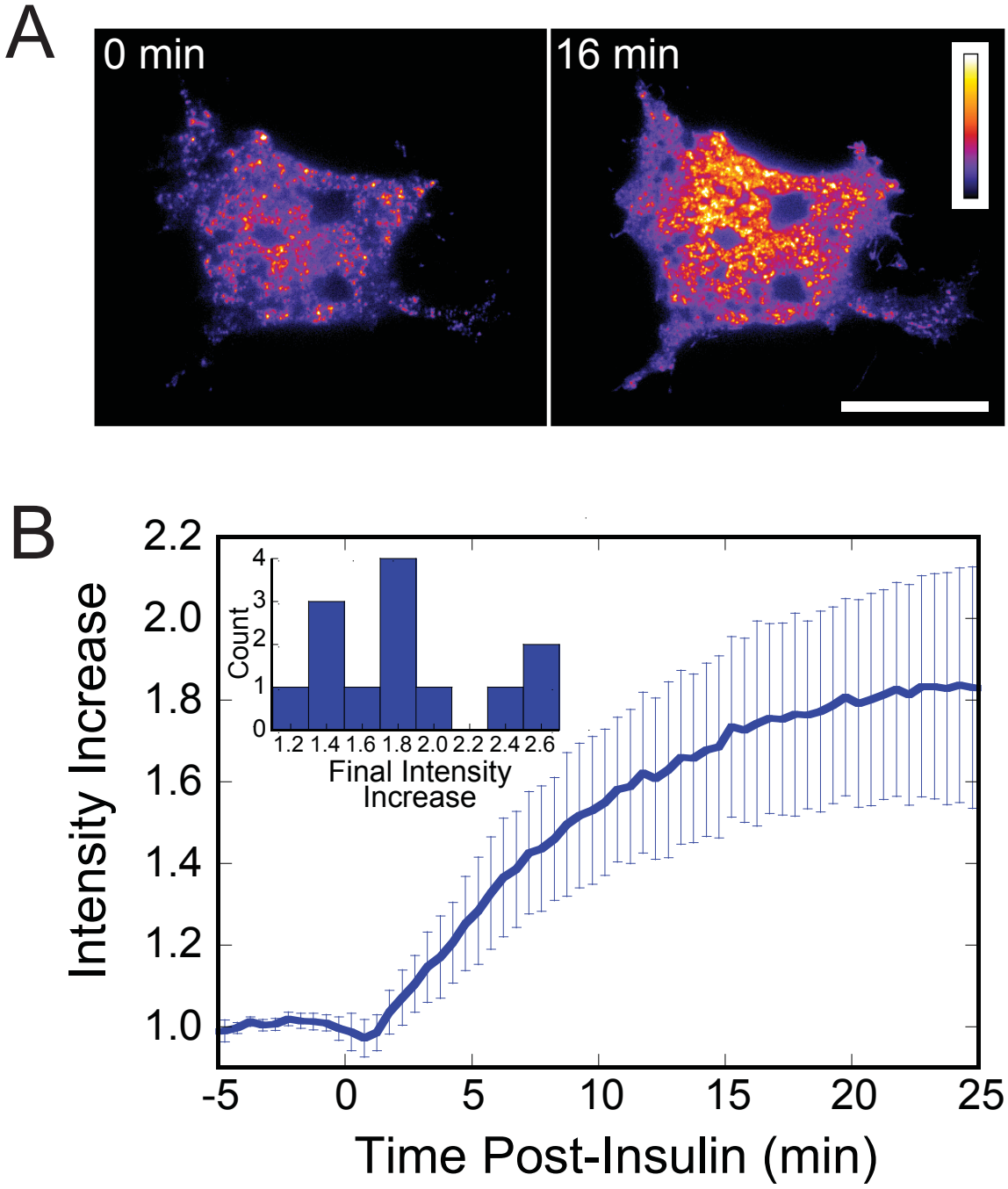

Figure 3.3 Insulin stimulation increases the intensity of HA-GLUT4-eGFP within the TIRF illumination zone.

Figure 3.3 Insulin stimulation increases the intensity of HA-GLUT4-eGFP within the TIRF illumination zone.

Adipocytes transfected with HA-GLUT4-eGFP were serum-starved prior to stimulation with 100 nM insulin at t = 0 min. Images were acquired using TIRF microscopy at 1 frame per 10 s.

(A) Pseudocolor of HA-GLUT4-eGFP intensity before and after insulin stimulation. Elapsed time from insulin addition is indicated. Scale bar is 20 μm. See Movie 1.

(B) Time course of the increase in fluorescence intensity in response to insulin. Fold intensity increase relative to the average intensity prior to insulin addition was calculated for each cell. Plotted is the mean ± 95% confidence interval (n = 13 cells). **(Inset)** Histogram of the fold intensity change at plateau.

Table 3.1 Time course parameters

CONDITION	Max fold ± 95% CI[a]	$t_{1/2}$ (min)	t_{lag} (min)	n[b]
HA-GLUT4-eGFP, 0 µM Noc	1.8 ± 0.3	6.3	0.8	13
HA-GLUT4-eGFP, 10 µM Noc	1.6 ± 0.3	9.8	3.5	7
IRAP-pHluorin, 0 µM Noc	2.8 ± 1.1	7.0	1.4	8
IRAP-pHluorin, 10 µM Noc	2.1 ± 0.5	8.5	1.7	12
Microtubule density	1.4 ± 0.1	2.5	0.7	18

Time course parameters are calculated from Figures 3.3, 3.5, and 3.13.
[a]Max fold intensity or density increase relative to baseline. CI, confidence interval.
[b]Number of cells per condition.

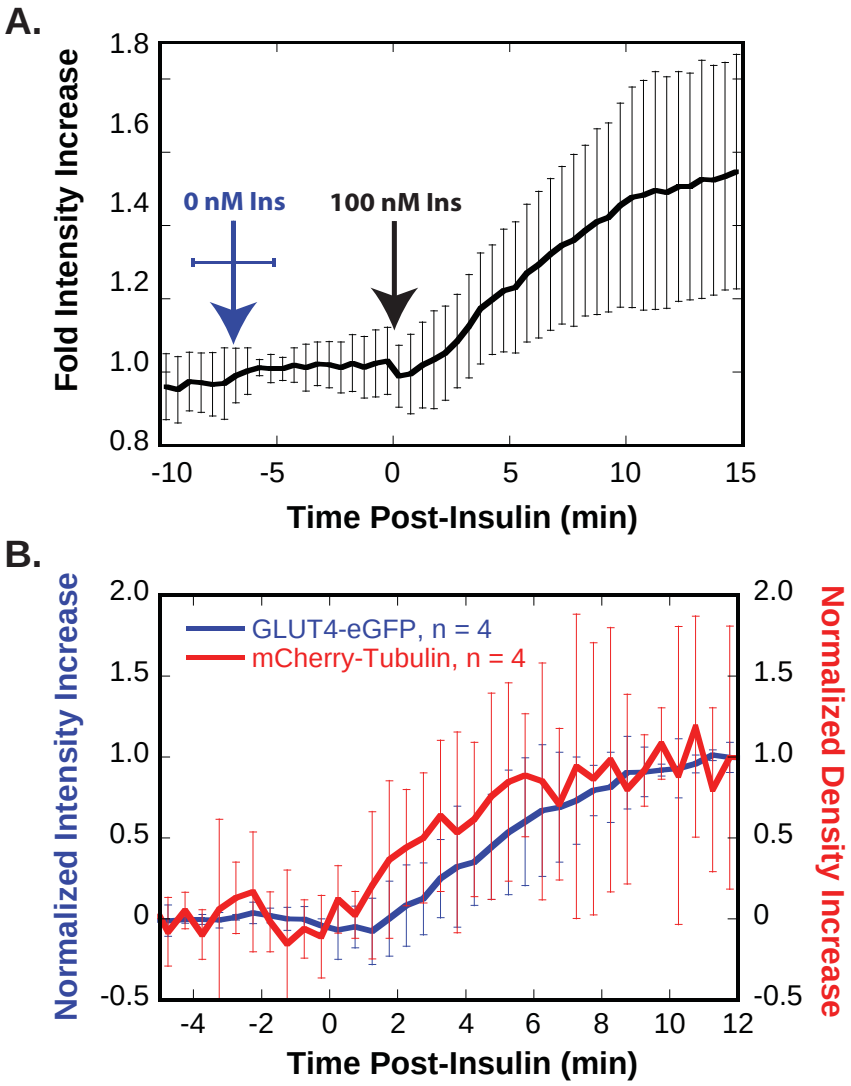

Figure 3.4 Time courses of HA-GLUT4-eGFP intensity and microtubule density increase.

(A) Addition of 100 nM insulin (black arrow) results in the increase in HA-GLUT4-eGFP in the TIRF illumination zone. Addition of starvation medium 5-10 min before addition of insulin (blue arrow) does not result in a fluorescence increase. Plotted is the mean ± 95% confidence interval (n = 8 cells).

(B) In cells co-transfected with mCherry-tubulin and HA-GLUT4-eGFP, the time course of the microtubule density increase in the TIRF illumination zone precedes the increase in the intensity of HA-GLUT4-eGFP. Intensity or density increases for each cell were normalized from 0 to 1 as in Figure 3.5A. Insulin (100 nM) was added at t = 0 min. Plotted is the mean ± 95% confidence interval (n = 4 cells). **(A and B)** Images were acquired using TIRF microscopy at 1 frame per 10 s.

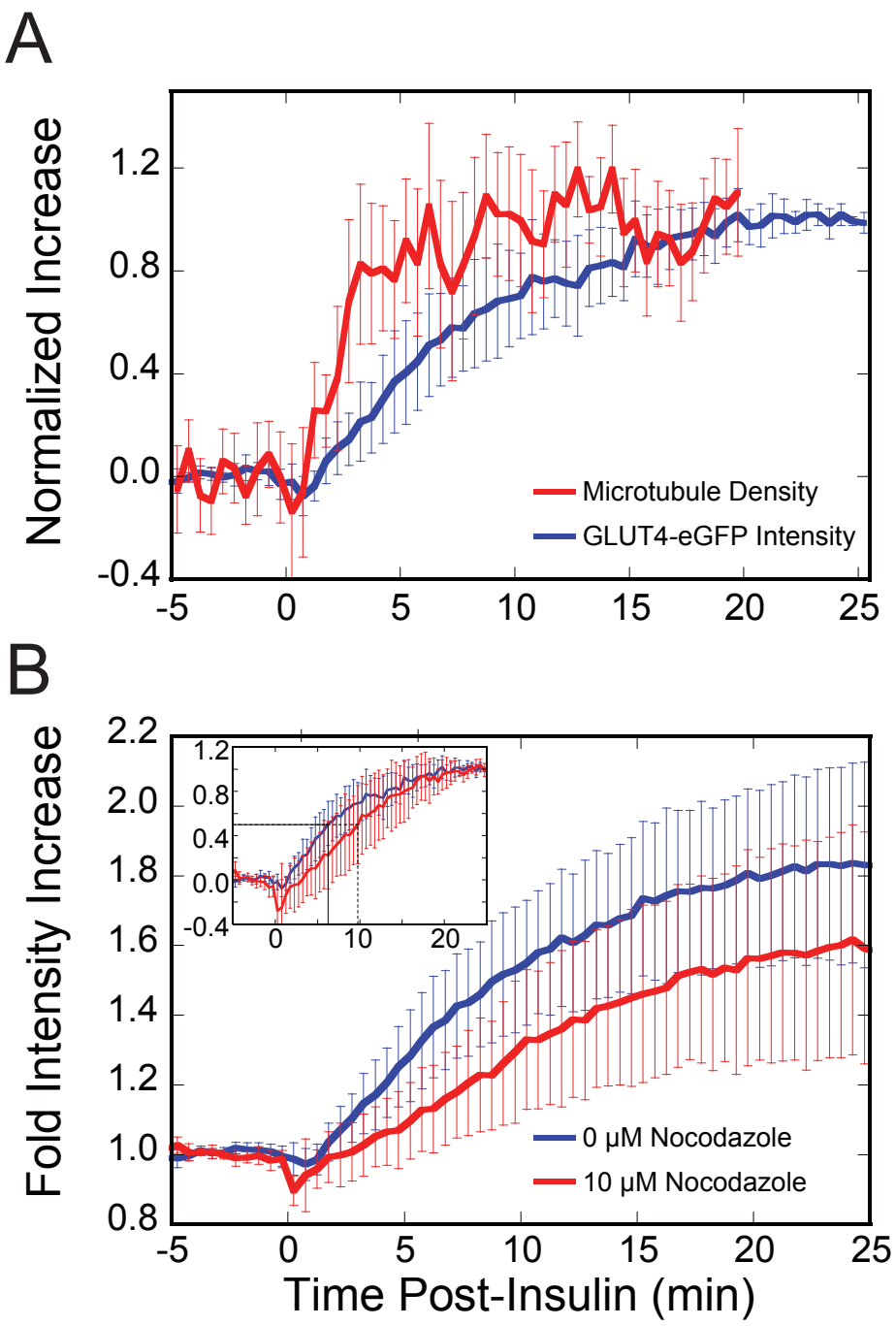

Figure 3.5 Time courses of HA-GLUT4-eGFP intensity and microtubule density increase.

Figure 3.5 Time courses of HA-GLUT4-eGFP intensity and microtubule density increase.

(A) Insulin increases microtubule density in the region of the cell illuminated by TIRF microscopy. Adipocytes transfected with constructs either to visualize the GLUT4 or microtubule time course were serum-starved prior to stimulation with 100 nM insulin at t = 0 min. Images were acquired using TIRF microscopy at 1 frame per 10 s. Intensity or density increase for each cell was normalized from 0 (average intensity or density prior to insulin addition) to 1 (intensity at last 1 minute or density at last 8 minutes of time course). Plotted is the mean ± 95% confidence interval for each point (HA-GLUT4-eGFP, n = 13 cells; mCherry-tubulin, n = 18 cells).

(B) Nocodazole pre-treatment decreases the fold change in GLUT4 intensity in response to insulin. Adipocytes expressing HA-GLUT4-eGFP were serum-starved and pre-treated with 0 μM (blue, n = 13 cells) or 10 μM (red, n = 7 cells) nocodazole for a minimum of 20 min prior to stimulation with 100 nM insulin at t = 0 min. Images were acquired using TIRF microscopy at 1 frame per 10 s. Plotted is the time course of the mean fold intensity increase ± 95% confidence interval. **(Inset)** Time course of the intensity increase normalized from 0 (average intensity prior to insulin addition) to 1 (intensity at last minute of time course). Plotted is the mean ± 95% confidence interval. Half-times are plotted (0 μM Noc, $t_{1/2}$ = 6.3 min, solid black line; 10 μM Noc, $t_{1/2}$ = 9.8 min, dashed black line).

Treatment of cells with 10 µM nocodazole for 20 min, which results in large-scale depolymerization of the microtubule cytoskeleton (Figure 3.7), reduced the insulin-stimulated increase in HA-GLUT4-eGFP intensity to 1.6-fold (Figure 3.5B, Table 3.I). Nocodazole treatment also introduced a time-lag (t_{lag} = 3.5 min), defined as the intercept with the baseline of a line drawn through and having a slope determined at the inflection point, and slowed the kinetics of the fluorescence increase ($t_{1/2}$ = 9.8 min) in the TIRF-zone (Figure 3.5B inset).

3.3.3 Insulin-stimulation induces microtubule curvature

Strikingly, a population of highly curved microtubules is detected in the TIRF-illumination zone of adipocytes. Curvature is detected by immunofluorescence of endogenous microtubules as well as by live-cell imaging of adipocytes transfected with GFP-tubulin, mCherry-tubulin, or 3xGFP-EMTB (Figures 3.6A and 3.8A, Movie 2). When plotted so that the coordinates of continuous microtubule segments ≥ 3 µm in length share the same origin and initial microtubule orientation, the curvature appears to increase upon insulin stimulation (Figure 3.6B). We quantified curvature by calculating the cosine correlation function (CCF) along the contour of the microtubule (Figures 3.2B and 3.6C). The CCF of more highly curved microtubules decays toward 0 more quickly than straighter microtubules. We plotted the average CCF for microtubule segments at least 3 µm in length as a function of time, and found that curvature increased with time after insulin stimulation (Figure 3.6D).

Many curved microtubules appeared to be actively and abruptly displaced by forces that translocated them along the plane of the membrane or pulled them closer to

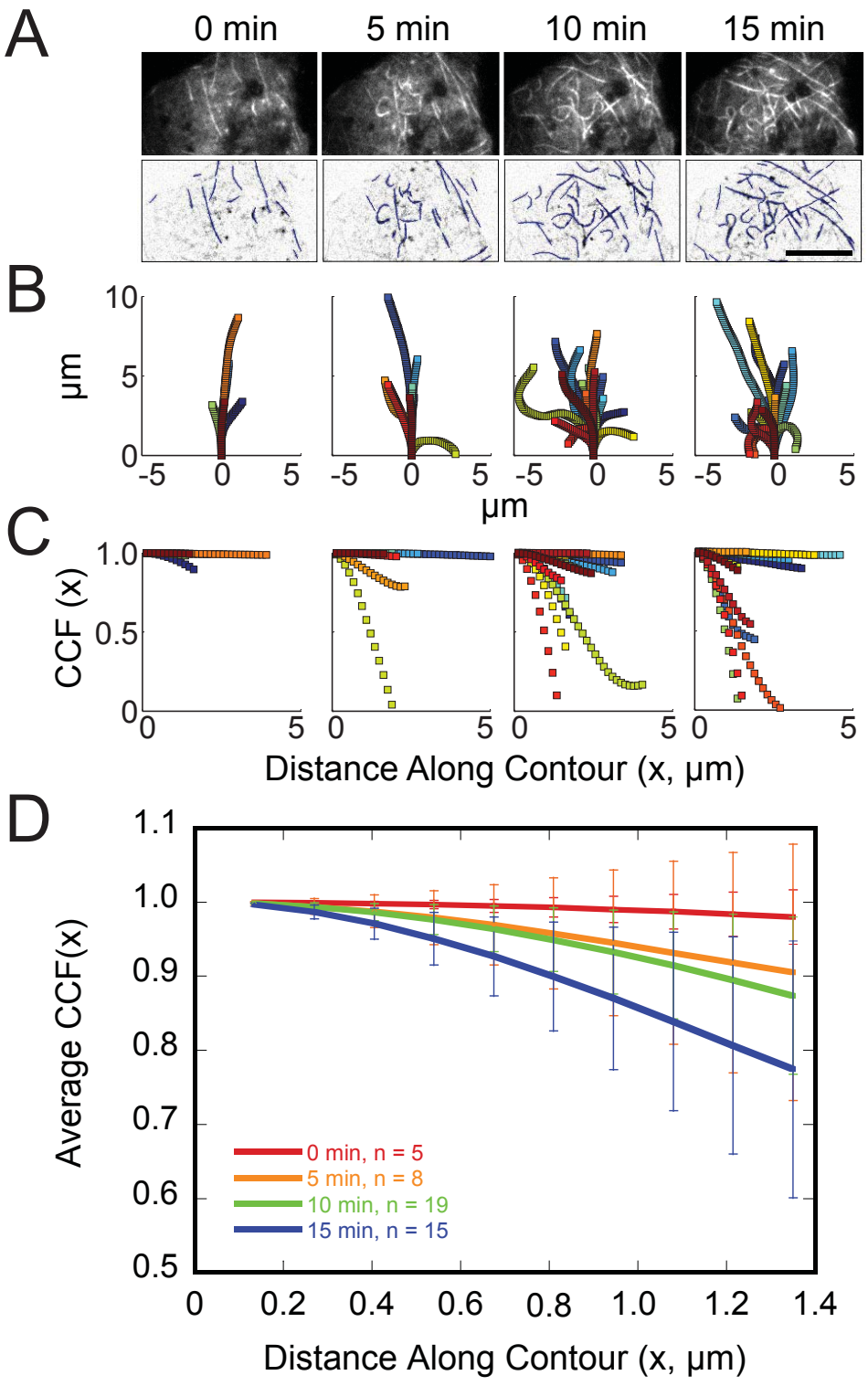

Figure 3.6 TIRF microscopy reveals a population of highly curved microtubules at the surface of 3T3-L1 adipocytes.

Figure 3.6 TIRF microscopy reveals a population of highly curved microtubules at the surface of 3T3-L1 adipocytes.

Adipocyte transfected with mCherry-tubulin was serum-starved prior to stimulation with 100 nM insulin at t = 0 min. Images were acquired using TIRF microscopy at 1 frame per 10 s. Elapsed time from insulin addition is indicated. See Movie 2.

(A) (Upper) Unprocessed and **(Lower)** background-subtracted, inverted contrast images. Microtubule contours are overlaid in blue. Scale bar is 10 μm.

(B) Contours for microtubules at least 3 μm in length were replotted to share the same origin (0 min, 5 contours; 5 min, 8 contours; 10 min, 19 contours; 15 min, 15 contours).

(C) Cosine correlation function (CCF) for microtubule contours shown in **(B)**, see Figure 3.2 for details.

(D) The average CCF up to the minimum contour length for microtubule contours shown in **(C)** are plotted at 0 (red), 5 (orange), 10 (green), and 15 (blue) minutes post-insulin. Error bars represent the 95% confidence interval.

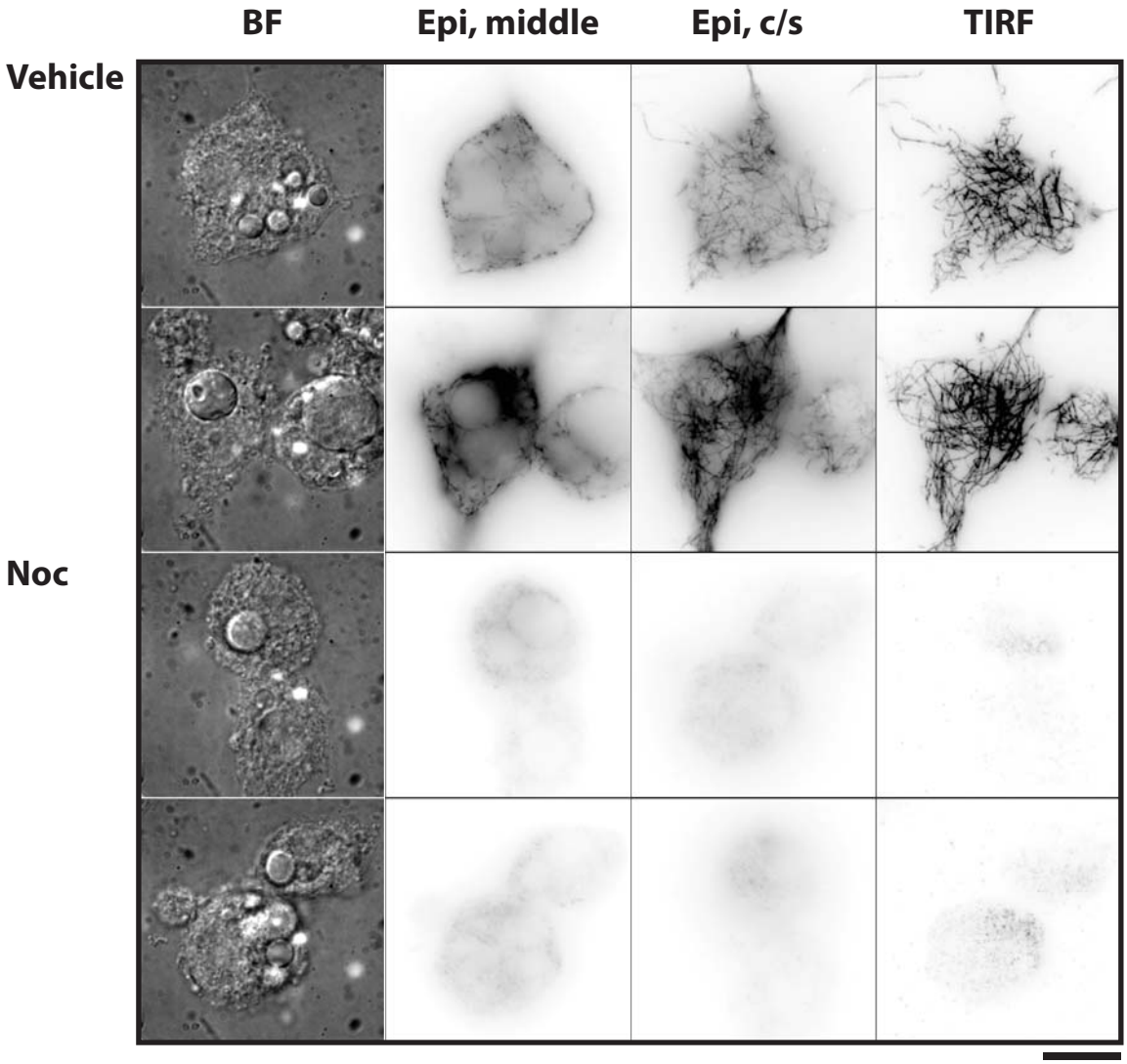

Figure 3.7 Nocodazole treatment disrupts the microtubule cytoskeleton.

3T3-L1 adipocytes were pre-treated with **(Vehicle)** DMSO or **(Noc)** 10 μM nocodazole for 10 min prior to fixation in methanol + 1 mM EGTA. **(BF)** Brightfield image.

Microtubules were immunostained for α-tubulin and visualized by using epifluoresence while focused **(Epi, middle)** in the center of the cell or **(Epi, c/s)** at the coverslip or by using **(TIRF)** TIRF microscopy. Scale bar is 15 μm.

or further from the cell surface (Figure 3.9, Movies 3 – 7). Several types of motion were observed. For example, microtubule loops often formed when an internal region of a microtubule moved parallel to the x-y plane. In some instances, the locations where the microtubule transitioned to visibility in TIRF appeared fixed, as if the microtubule was being threaded through these locations on the cell surface (Movie 3). Microtubules also appeared to move relative to or slide along a second, more stationary microtubule or microtubule segment (Movie 4). In other cases, straight segments of microtubules appeared to glide in a plane parallel to the coverslip (Movie 5). Three-dimensional time-lapse imaging using Parallax microscopy (Sun *et al.*, 2009) revealed abrupt, short duration z-displacements of microtubule regions as they moved toward and away from the plasma membrane (Movies 6 and 7).

To investigate whether microtubule polymerization could account for the observed microtubule bending, we treated adipocytes with a low dose of nocodazole (2 µM), and examined microtubule dynamics using TIRF microscopy. Under these conditions, tubulin heterodimers are sequestered resulting in microtubule depolymerization (Movie 8). However, substantial curvature and displacement dynamics remain even for depolymerizing microtubules (Figure 3.8B, Movie 8) suggesting that forces generated from polymerization are not driving curvature.

We next tested whether microtubule motor activity or actin-dependent motility is responsible for the observed microtubule dynamics. Over-expression of a dominant-negative construct of $p150^{Glued}$ (GFP-CC1) to disrupt dynein-dynactin function (Mentlik *et al.*, 2010; Quintyne *et al.*, 1999) did not abolish the microtubule curvature or the forces displacing the microtubules (Figure 3.8C), nor did treatment with either 2 µM cytochalasin D (cytoD) or 20 µM latrunculin B (latB) to disrupt the actin cytoskeleton (Figure 3.8D). These results suggest the involvement of a kinesin motor. In preliminary

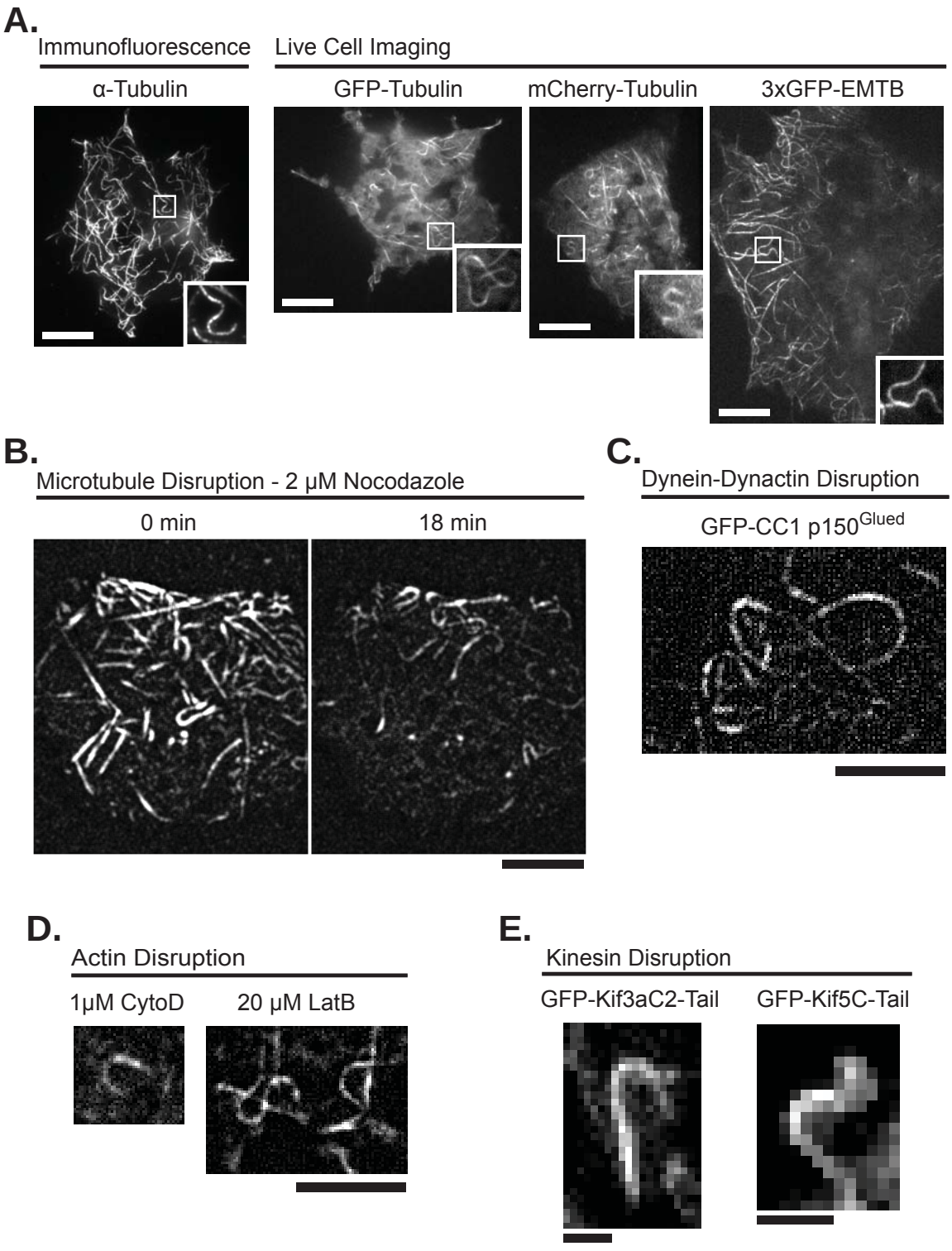

Figure 3.8 Microtubule curvature in 3T3-L1 adipocytes.

Figure 3.8 Microtubule curvature in 3T3-L1 adipocytes.

(A) Curved microtubules are seen when visualized by TIRF via immunofluorescence of endogenous tubulin (clone DM1A) in fixed cells, or by direct observation of adipocytes transfected with GFP-tubulin, mCherry-tubulin, or 3xGFP-EMTB. Scale bar is 10 µm. Inset is 5 µm x 5 µm.

(B) TIRF images of an adipocyte transfected with mCherry-tubulin and treated with 2 µM nocodazole (added at t = 0) show curved microtubules. Thus, forces from microtubule polymerization are not responsible for bending. TIRF images have been background-subtracted. Scale bar is 10 µm. See Movie 8.

(C) TIRF image of adipocyte co-transfected with mCherry-tubulin and GFP-CC1 p150Glued showing the presence of curved microtubules. Scale bar is 5 µm.

(D) TIRF image of adipocytes transfected with GFP-tubulin and treated with 1 µM cytoD or 20 µM latB for a minimum of 20 minutes showing curved microtubules. The treatment was sufficient to disrupt the actin cytoskeleton. TIRF images have been background-subtracted. Scale bar is 5 µm.

(E) TIRF images of curved microtubules in adipocytes co-transfected with mCherry-tubulin and the indicated dominant negative kinesin construct. Scale bars are 2 µm.

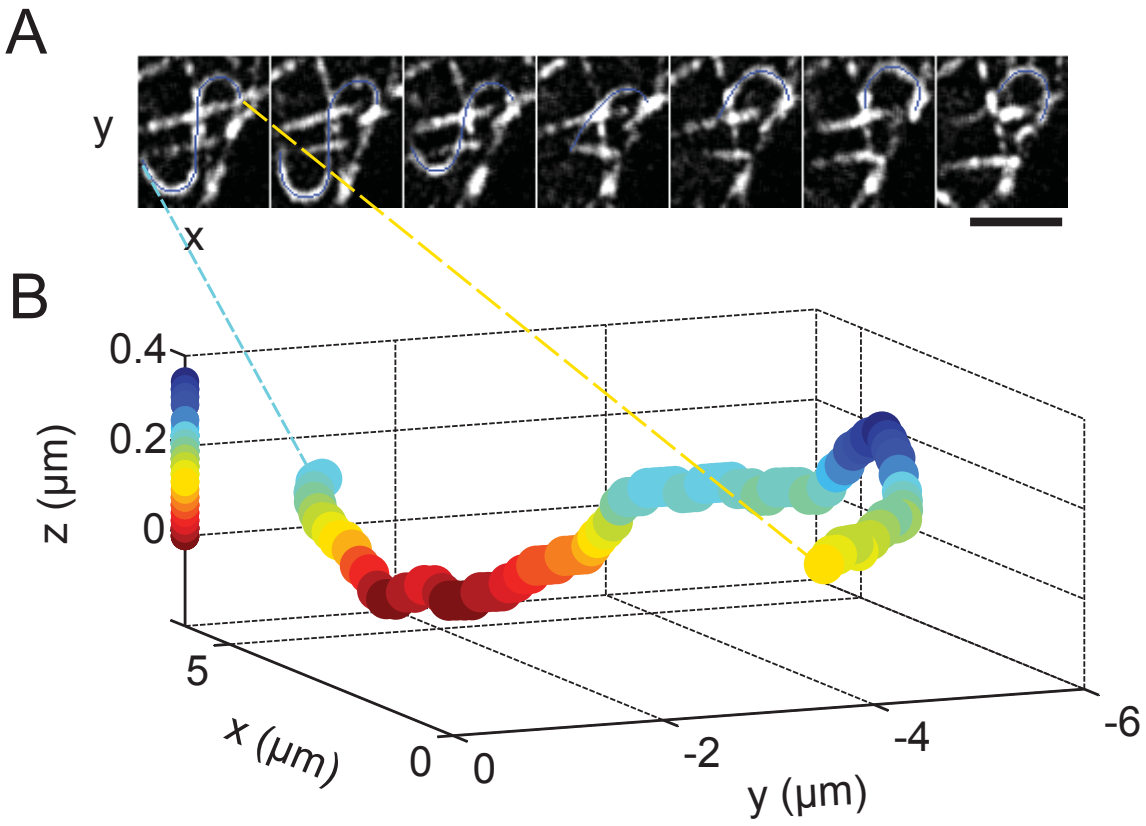

Figure 3.9 Curved regions of microtubules are actively displaced.

Adipocyte was transfected with 3xGFP-EMTB. Images were acquired using TIRF microscopy.

(A) Force-induced displacement of a microtubule. Images from a time course (Movie 6) have been background-subtracted. Frames are displayed at 30 s intervals. Microtubule contour is overlaid in blue. Scale bar is 3 µm.

(B) 3-Dimensional imaging of curved microtubule using Parallax and TIRF microscopies. The microtubule displayed in **(A)** is plotted as a series of (x,y,z) coordinates. A pair of 2-dimensional TIRF images (**A**: 1 of pair) was used to calculate relative z-depth. Warmer colors are closer to the coverslip. For an animation of the 3-dimensional time course see Movie 7.

experiments using dominant negative KIF3a and KIF5 constructs, we did not observe a disruption in microtubule curvature (Figure 3.8), although it is possible that we did not achieve sufficient disruption of endogenous kinesin. While we chose these kinesins because of their reported involvement in GLUT4 trafficking (Imamura *et al.*, 2003; Semiz *et al.*, 2003; Lalioti *et al.*, 2009; Huang *et al.*, 2005), another kinesin may instead be responsible.

Curvature is not correlated with microtubule acetylation (Figure 3.10A), in contrast to what has been found in other cell types (Friedman *et al.*, 2010). Although many curved microtubules are highly acetylated in 3T3-L1 adipocytes, many have low acetylation levels and, conversely, straight portions of microtubules are also highly acetylated. The primary observation is that more centrally-localized microtubules had higher acetylation levels than peripheral microtubules (Figure 3.10A-B), as reported previously in other cell types (Friedman *et al.*, 2010). Microtubules in adipocytes appeared to have greater levels of acetylation than microtubules in incompletely differentiated 3T3-L1 cells found on the same coverslip (Figure 3.10B).

3.3.4 Fusion events preferentially occur near microtubules

Both HA-GLUT4-eGFP-containing vesicles in proximity to the cell surface, and HA-GLUT4-eGFP inserted in the plasma membrane, contribute to the observed TIRF fluorescence intensity. To better detect vesicle fusions with the plasma membrane, we used an IRAP-pHluorin construct that fuses the pH-sensitive eGFP variant (pHluorin) (Miesenbock *et al.*, 1998) to the lumenal side of amino acids 1-393 of insulin-regulated aminopeptidase (IRAP) (Jiang *et al.*, 2008). This construct uses IRAP as a surrogate for

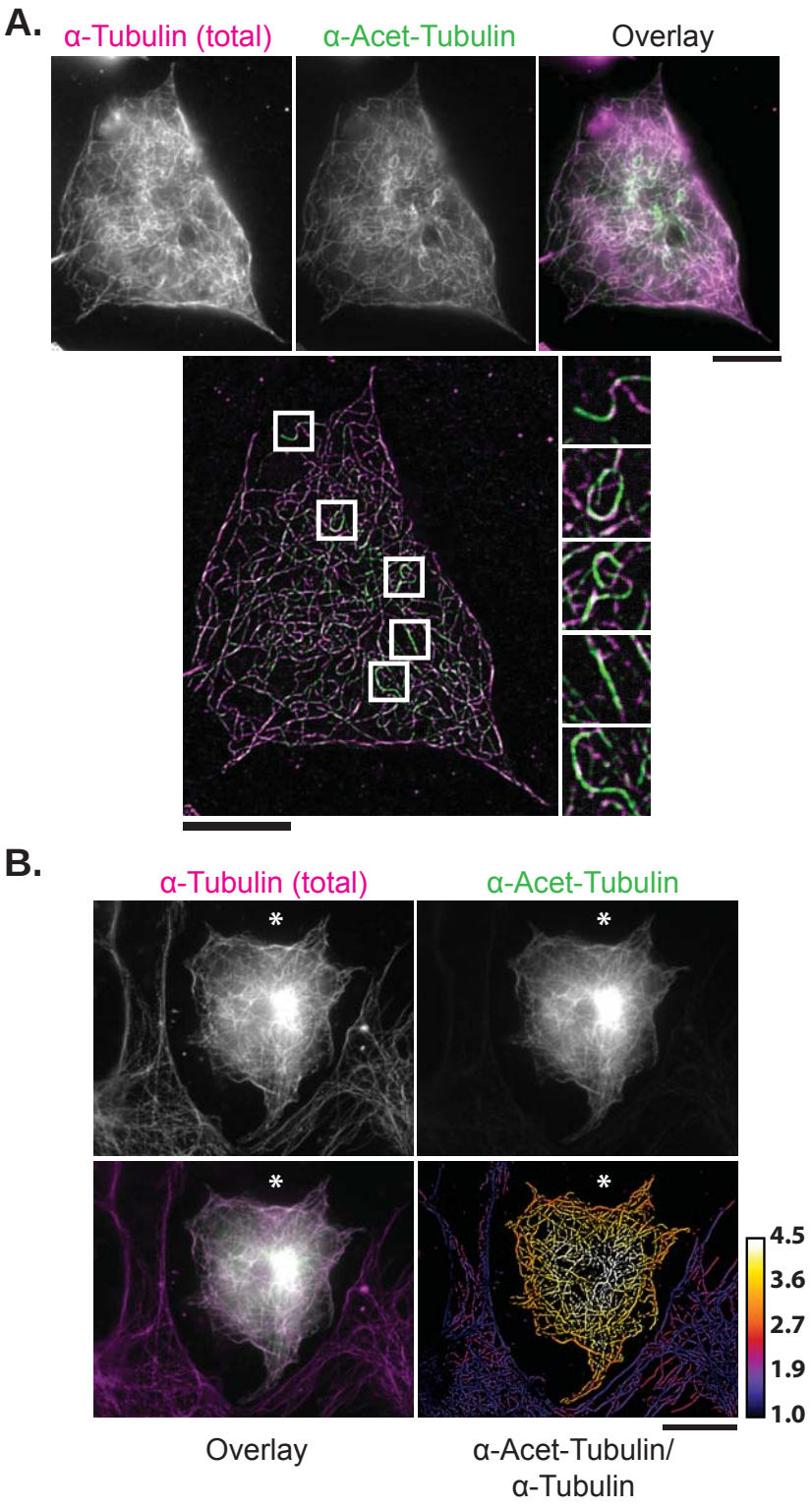

Figure 3.10 Microtubule curvature does not correlate with acetylation in 3T3-L1 adipocytes.

Figure 3.10 Microtubule curvature does not correlate with acetylation in 3T3-L1 adipocytes.

3T3-L1 cells were removed from culture dishes by trypsin treatment and replated in growth medium onto glass coverslips, fixed, and immunostained with α-tubulin (for visualization of total tubulin) and α-acetylated-tubulin antibodies.

(A, Top) Epifluorescence images of an adipocyte stained for total (magenta) and acetylated (green) tubulin. The overlay shows regions of colocalization (white). Scale bar is 15 μm.

(A, Bottom) Background-subtracted image of overlay with regions of interest highlighted in white boxes and expanded to the right. Scale bar is 15 μm. Expanded regions have dimensions of 5 μm x 5 μm.

(B) Epifluorescence images of an adipocyte (highlighted by an asterisk) flanked by two incompletely differentiated, fibroblast-like cells. **(Bottom Right)** The ratio of the background-subtracted image of α-acetylated-tubulin to the background-subtracted image of α-tubulin was calculated, and values were divided by the minimum value. White indicates the highest ratio of α-acetylated-tubulin to α-tubulin. Scale bar is 20 μm.

GLUT4 since both N- and C- termini of GLUT4 face the cytosol (Figure 2.4), and it is difficult to place fluorophores on a lumenal domain of GLUT4 without disrupting GLUT4 trafficking. IRAP is a transmembrane protein enriched in insulin-responsive vesicles that co-localizes and co-fractionates with GLUT4 (Kandror and Pilch, 1994; Ross *et al.*, 1996; Sumitani *et al.*, 1997; Martin *et al.*, 1997; Malide *et al.*, 1997) and traffics in a manner indistinguishable from GLUT4 (Garza and Birnbaum, 2000). The lumenal pH of GLUT4 vesicles, and, therefore, pHluorin fluorescence emission, is low. Upon fusion of GLUT4 vesicles with the plasma membrane, pHluorin is exposed to the neutral pH of the imaging medium, and the fluorescence emission increases. To demonstrate the improved fusion detection, we co-expressed HA-GLUT4-mCherry and IRAP-pHluorin and simultaneously excited the fluorophores. The time course of a single vesicle fusion event is shown (Figure 3.11A), beginning with the initial approach of the vesicle to the cell surface and ending with dispersal within the plasma membrane.

Sites of insulin-stimulated vesicle fusion appear to correlate spatially with microtubules in the TIRF-illumination zone. Simultaneously imaged mCherry-IRAP-pHluorin and 3xGFP-EMTB in adipocytes show that that many fusion events occur in proximity to microtubules (Figure 3.11B, Movie 9). To obtain a quantitative measure of proximity, we correlated the position of microtubules, visualized with mCherry-tubulin, with IRAP-pHluorin fusion sites. Because the probability that a fusion will occur near a microtubule depends on the microtubule density, proximity distances were determined as a function of cellular microtubule density. A cumulative distribution of the distance of fusion events in cells with low microtubule density shows that ~40% of fusions occur ≤ 200 nm (approximately the resolution of our measurement) from a microtubule (Figure 3.12). Similarly, at an intermediate microtubule density, the probability of a fusion

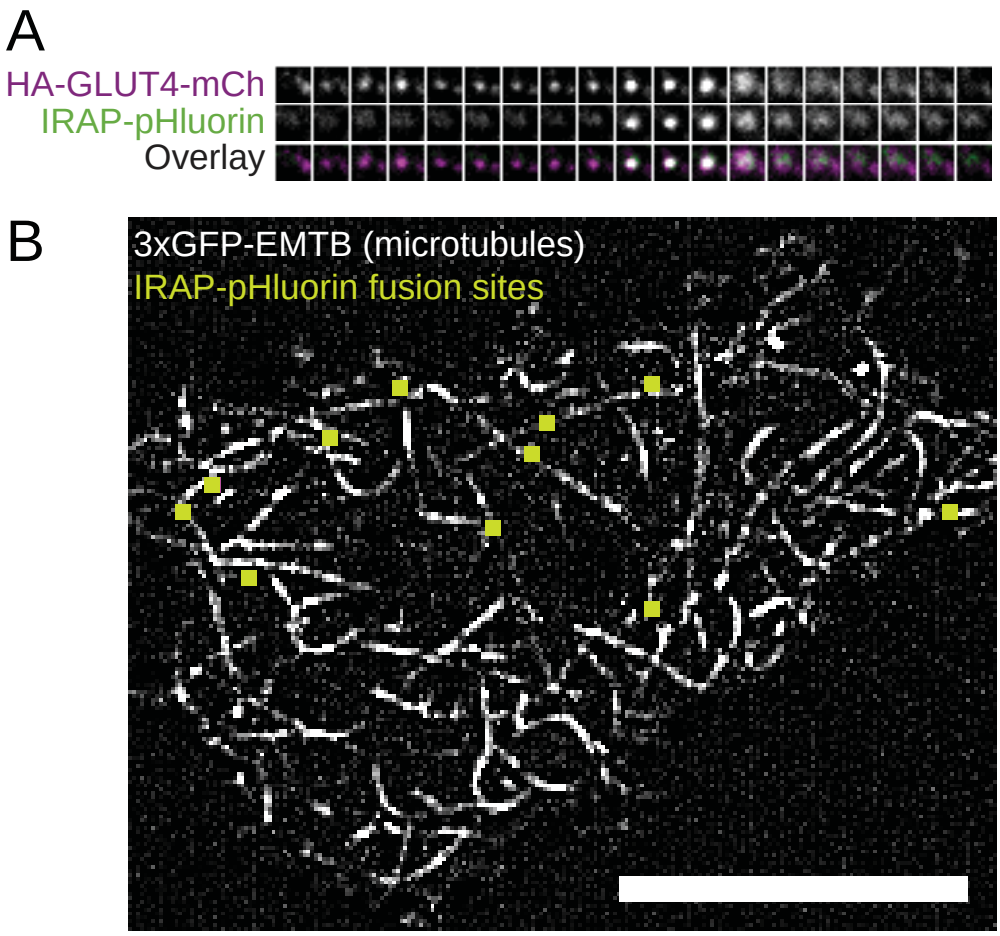

Figure 3.11 Sites of IRAP-pHluorin vesicle fusion with the plasma membrane occur in proximity to microtubules at the cell surface.

Adipocytes co-transfected with the indicated constructs were serum-starved prior to stimulation with 100 nM insulin. Images were acquired using TIRF microscopy at an acquisition rate of 20 Hz.

(A) Fusion of a single vesicle with the plasma membrane. Each panel displays a single frame of a Dual-View image: **(Top)** HA-GLUT4-mCherry, **(Middle)** IRAP-pHluorin, **(Bottom)** Overlay. Each box is 1.89 µm x 1.89 µm.

(B) Fusions occur in proximity to microtubules visible in TIRF microscopy. Displayed is a 50 frame (2.5 s) maximum intensity projection image of an adipocyte co-expressing mCherry-IRAP-pHluorin and 3xGFP-EMTB. The image has been background-subtracted. Sites of vesicle fusion during the 2.5 s are overlaid (green squares). Scale bar is 10 µm. See Movie 9.

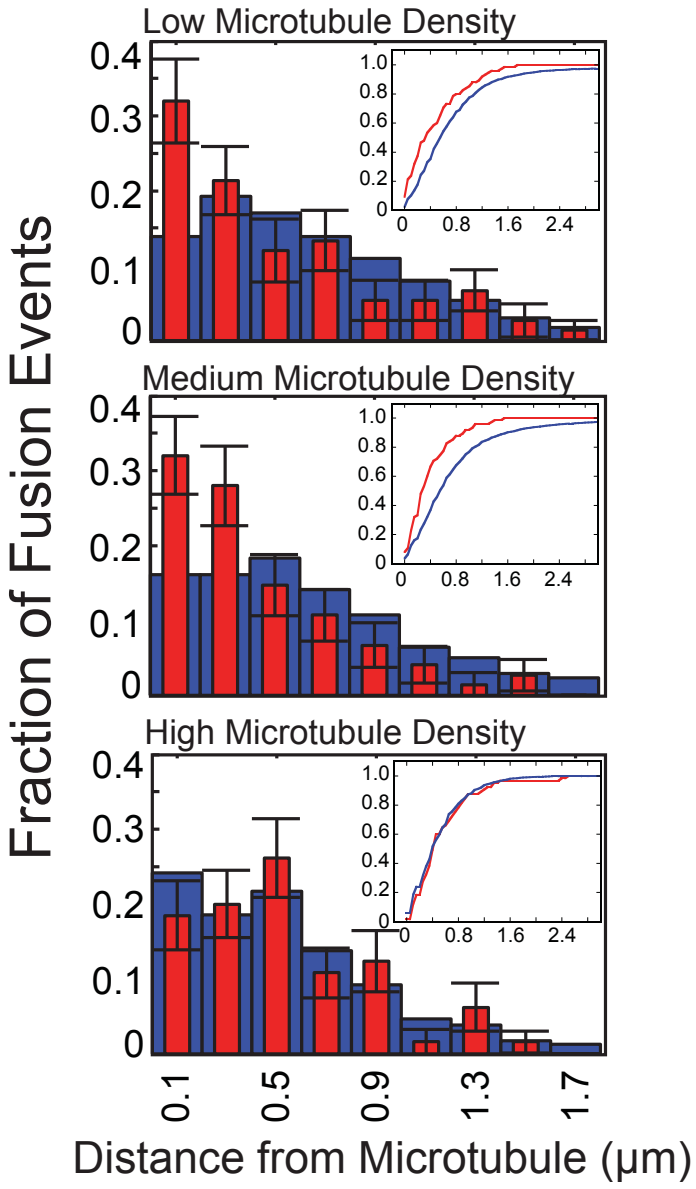

Figure 3.12 Sites of IRAP-pHluorin fusion are spatially correlated with microtubules present in the TIRF illumination zone.

Adipocytes co-transfected with IRAP-pHluorin and mCherry-tubulin were serum-starved prior to stimulation with 100 nM insulin. Histogram of distance of fusion events from a microtubule obtained using TIRF microscopy and a Dual-view insert at an acquisition rate of 20 Hz (**red**, fusions; **blue**, random locations). Center of bin (width = 0.2 μm) is indicated. Error bars represent the standard deviation resulting from bootstrapping (n = 100 repetitions) the fusion data. **(Inset)** Cumulative distributions of the data shown in the plots.

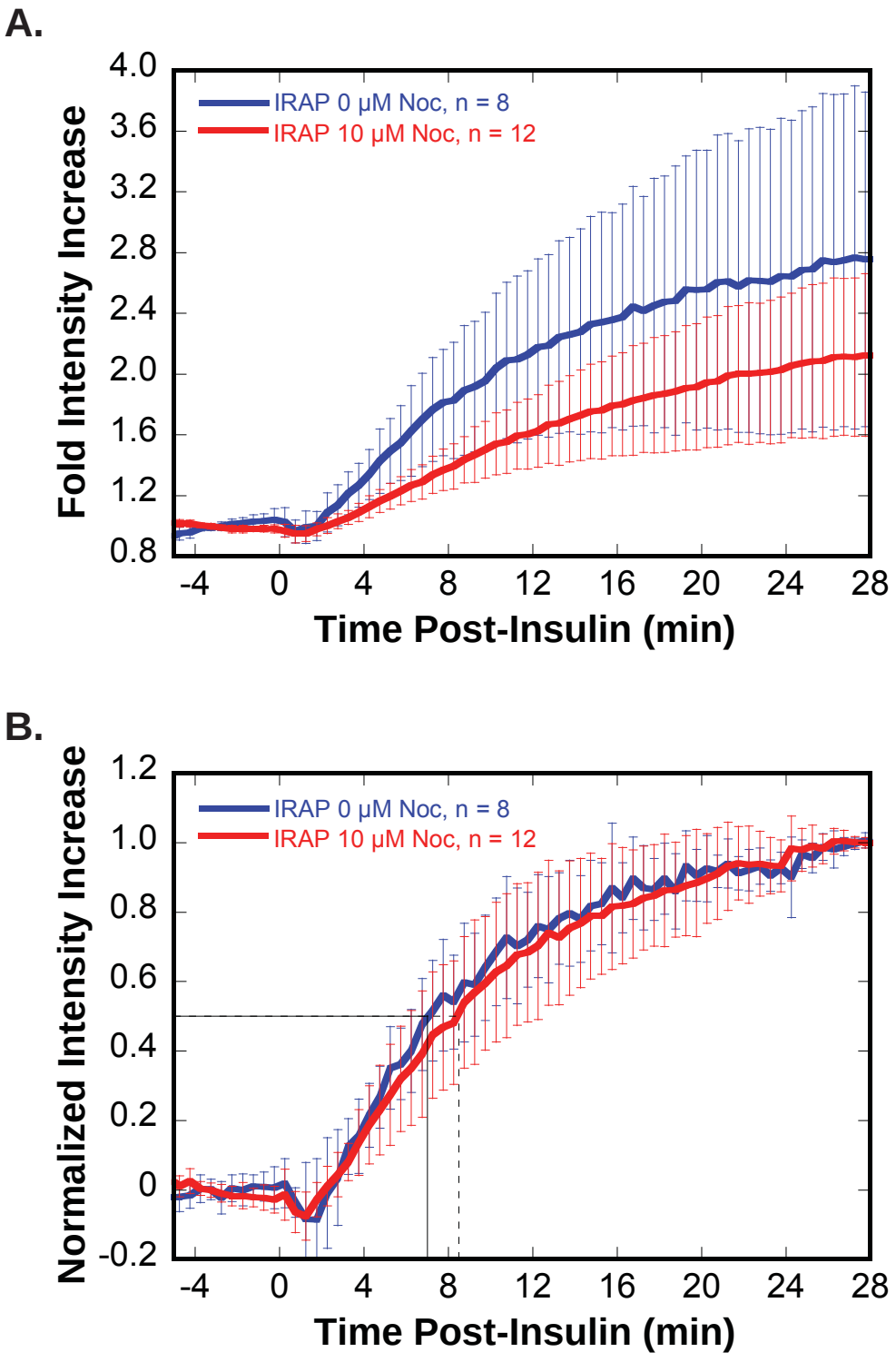

Figure 3.13 Insulin stimulation increases the intensity of IRAP-pHluorin in the TIRF illumination zone.

Figure 3.13 Insulin stimulation increases the intensity of IRAP-pHluorin in the TIRF illumination zone.

Adipocytes transfected with IRAP-pHluorin were serum-starved and pre-treated with 0 μM (blue, n = 8 cells) or 10 μM nocodazole (red, n = 12 cells) prior to stimulation with 100 nM insulin at t = 0 min. Images were acquired using TIRF microscopy at 1 frame per 10 s.

(A) Time course of the fold intensity increase. Plotted is the mean ± 95% confidence interval.

(B) Time course of the intensity increase normalized from 0 (average intensity prior to insulin addition) to 1 (intensity at last minute of time course). Plotted is the mean ± 95% confidence interval. Half-times are plotted (0 μM Noc, $t_{1/2}$ = 7 min, solid black line; 10 μM Noc, $t_{1/2}$ = 8.5 min, dashed black line).

occurring adjacent to a microtubule is substantially greater than random chance. At high densities, even random sites occur near microtubules (Figure 3.12).

We confirmed that IRAP-pHluorin TIRF intensity increases in response to insulin (Figure 3.13A, Table 3.1). IRAP-pHluorin intensity increases within the first few minutes of insulin addition with a $t_{1/2}$ = 7 min. The time to plateau is slightly longer than measured for HA-GLUT4-eGFP, which may reflect the selective detection of membrane fusion events, rather than proximity to the plasma membrane. Interestingly, 10 μM nocodazole treatment to disrupt microtubules did not markedly slow the time course of the IRAP-pHluorin fluorescence increase (Figure 3.13B, Table 3.1). Nocodazole treatment may also decrease the final fold intensity change in response to insulin (Figure 3.13B, Table 3.1). Although the error associated with this measurement is large and makes interpretation difficult, the reduction in intensity could indicate fewer GLUT4 vesicle fusion events with the plasma membrane.

3.3.5 Long-distance movement of mCherry-IRAP-pHluorin prior to vesicle fusion is only rarely detected

Given that exocytic events preferentially take place in proximity to microtubules visible at the cell surface, we asked whether vesicle movements prior to fusion were consistent with microtubule-based transport. In particular, we asked whether vesicles moved linearly distances on the order of a micrometer prior to fusion. Cells were transfected with mCherry-IRAP-pHluorin, a construct which allows us to both observe vesicles prior to fusion (mCherry) and detect fusions efficiently (pHluorin). We observed that long-distance movements detectable using TIRF microscopy (Figure 3.14) rarely precede vesicle fusion in untreated cells (Table 3.2) and could not be detected in

nocodazole-treated cells (data not shown). Most often, vesicles appeared to approach the cell surface vertically without appreciable directed lateral movement, although some vesicles appeared to change velocity and direction repeatedly and rapidly prior to immobilization and fusion. These movements occurred in both untreated and nocodazole-treated cells (data not shown). Since 3T3-L1 adipocytes are tens of micrometers thick, we cannot rule out that microtubule-based movement from deeper in the cell towards the cell surface is not relevant to GLUT4 trafficking. However, we do detect long-distance movement at the cell surface, but this movement rarely culminates in vesicle fusion (Movie 10).

We hypothesize that microtubules may play a role in specifying fusion site locations through the delivery, localization, or scaffolding of signaling components or fusion machinery. For instance, in primary adipocytes, Exo70, a component of the exocyst complex, has been proposed to tether GLUT4 vesicles at the plasma membrane prior to fusion, preventing GLUT4 vesicle translocation along surface-localized microtubules (Lizunov *et al.*, 2009). In preliminary experiments, however, I did not observe a spatial correlation of GFP-Exo70 puncta with either microtubules or mCherry-IRAP (Figure 3.15A-B).

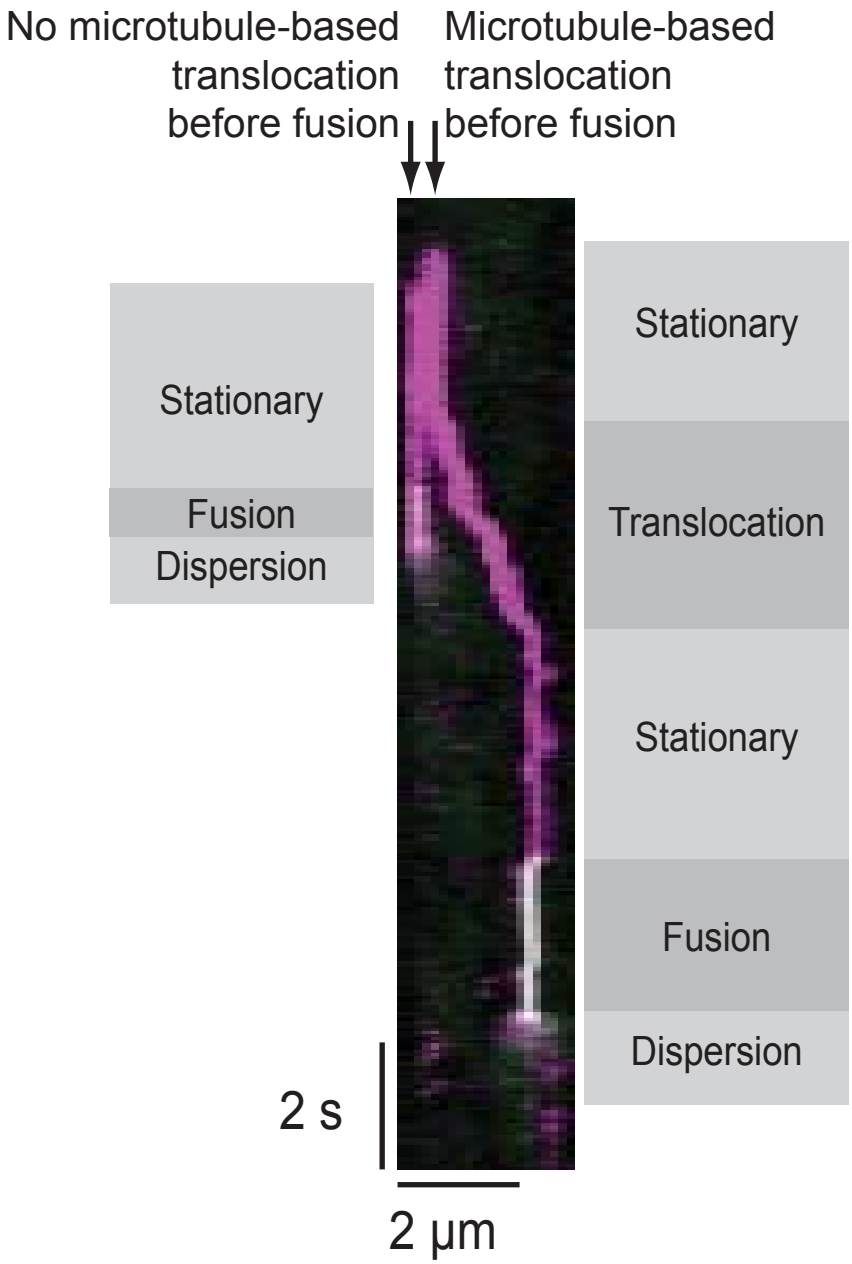

Figure 3.14 Movement of vesicles long distances prior to fusion is observed infrequently.

Adipocyte transfected with mCherry-IRAP-pHluorin was serum-starved prior to stimulation with 100 nM insulin. Images were acquired using TIRF microscopy at an acquisition rate of 20 Hz, and a kymograph was generated. A rare vesicle fusion event is preceded by a long-distance movement. A second vesicle approaches the surface in the same vicinity as the first but fuses without detected lateral movement.

Table 3.2 Vesicle movement prior to fusion with the plasma membrane

TOTAL	Unknown[a]	Fusions preceded by ~1 μm linear displacement	Fusions in which linear displacement was undetected[b]
221	47	4	170

Vesicle movements prior to fusion with the plasma membrane were determined in 3T3-L1 adipocytes (n = 4 cells) transfected with mCherry-IRAP-pHluorin and stimulated with 100 nM insulin.

[a]Vesicle movements were scored as unknown when high local vesicle density or low mCherry fluorescence intensity made determination of movement difficult.

[b]Linear displacement of ~1 μm or more was undetected prior to fusion of vesicle.

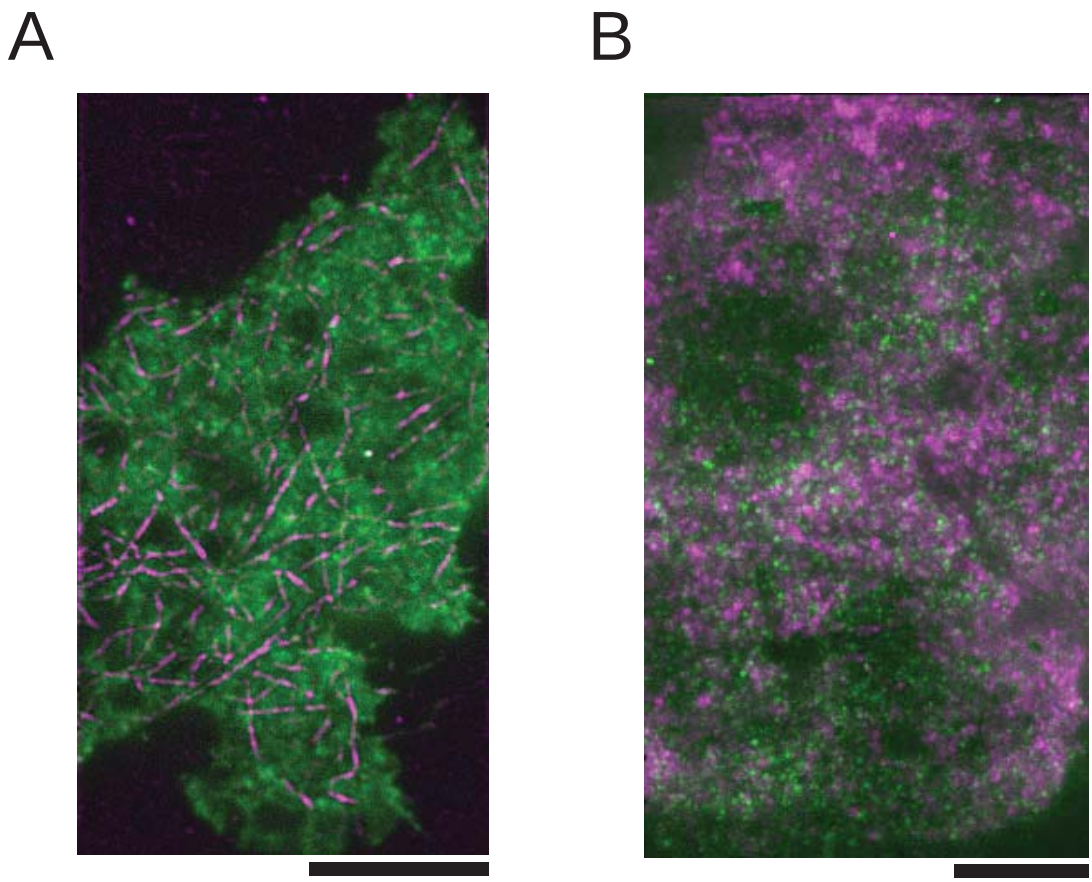

Figure 3.15 Exo70 puncta do not spatially correlate with either microtubules or IRAP at the cell surface.

Adipocytes were co-transfected with **(green)** GFP-rExo70 and either **(magenta) (A)** mCherry-tubulin or **(B)** mCherry-IRAP and TIRF images were acquired. Microtubules in **(A)** have been background-subtracted. The image in **(B)** is a maximum projection of 500 frames acquired at 5 frames per s. Scale bars are 10 μm.

3.4 DISCUSSION

3.4.1 Microtubule curvature and surface density increase may be mechanistically linked

The increases in microtubule density and bending in the TIRF illumination zone are striking down-stream effects of insulin signaling (Figures 3.4B and 3.5A). While it has been shown previously that the total amount of polymerized tubulin increases upon insulin stimulation (Olson *et al.*, 2003), the dramatic increase in concentration (Figure 3.5A) and bending (Figure 3.6) of the filaments we observed at the cell membrane was unexpected. The correlated increase in surface density and bending (Figure 3.6D) may be caused by related mechanisms. In support of this, microtubules appear to be forcibly pulled, often towards the cell surface (Figure 3.9, Movies 3 – 7, see below).

The high degree of microtubule curvature may result from these pulling forces. Cells treated with a nocodazole concentration that inhibits microtubule polymerization, but does not result in complete depolymerization, showed persistent microtubule curvature and pulling, indicating that the bending dynamics are not the result of polymerization-induced buckling (Figure 3.8B, Movie 8). Likewise, disruption of the actin cytoskeleton (Figure 3.8D) or dynein-dynactin function (Figure 3.8C) did not noticeably diminish the microtubule curvature or the microtubule displacements. Thus, kinesin motors are likely responsible for microtubule bending. One candidate motor that should be considered is kinesin-1 heavy chain, which is involved in microtubule-microtubule sliding in Xenopus and Ptk2 cells (Jolly *et al.*, 2010). At this time, it is unclear how microtubule curvature and force-induced displacement impact on GLUT4 vesicle trafficking.

As mentioned above, pulling of microtubule regions to the cell surface may contribute to the surface density. In addition, a net increase in microtubule polymerization also plays a role since the amount of polymerized tubulin throughout the cell increases in response to insulin (Olson *et al.*, 2003). It is unclear whether the increase in polymerized microtubules reflects an increase in polymerization, a decrease in depolymerization, an increase in nucleation, or some combination of the above mechanisms.

3.4.2 Microtubules are not required but may contribute to the efficiency of the GLUT4 insulin response

The increase in microtubule density ($t_{1/2}$ = 2.5 min) at the cell membrane preceded the increase in GLUT4 intensity ($t_{1/2}$ = 6.3 min) in the same region of the cell (Figure 3.5A, Table 3.1), so it is interesting to ask if microtubules have a role in the transport of GLUT4 to the cell surface or to the distribution of fusion sites. Nocodazole pre-treatment at a concentration and duration sufficient to disrupt the microtubule cytoskeleton (Figure 3.7) delayed the half-time for insulin-stimulated accumulation of GLUT4 at the cell surface from a $t_{1/2}$ = 6.3 min in the absence of nocodazole to a $t_{1/2}$ = 9.8 min at 10 µM nocodazole (Table 3.1) and introduced a time-lag in the intensity increase (Figure 3.5B inset, Table 3.1). GLUT4 vesicle trafficking is highly regulated so it is unlikely that microtubule stabilization is sufficient by itself to drive GLUT4 redistribution to the plasma membrane in the absence of insulin signaling. In support of this supposition, microtubule stabilization with taxol does not stimulate an increase in the basal level of GLUT4 at the cell surface (Molero *et al.*, 2001).

Nocodazole also modestly decreased the magnitude of GLUT4 translocation to the membrane (0 μM Noc, max fold = 1.8 ± 0.3; 10 μM Noc, max fold = 1.6 ± 0.3) (Figure 3.5B, Table 3.1). This result is consistent with several previous studies showing an approximate 20% – 40% reduction in translocation or plasma membrane insertion (Karylowski *et al.*, 2004; Liu *et al.*, 2003; Huang *et al.*, 2005; Olson *et al.*, 2003; Emoto *et al.*, 2001). One complication in assessing the contribution of microtubules in GLUT4 translocation is that microtubules are important in the appropriate sequestration of GLUT4 in the basal state (Huang *et al.*, 2005). Some of the effects of microtubule disruption on translocation might, therefore, be compensated for by basal GLUT4 redistribution to regions of the cell closer to the plasma membrane.

Taken together, our results suggest that microtubules are likely playing a role in the efficiency of mobilizing GLUT4 vesicles to the surface. They are also important for appropriate sequestering of GLUT4 in the basal state (Huang *et al.*, 2005). However, there appears to be no absolute requirement for microtubules in increasing the plasma membrane-insertion of GLUT4, as indicated by the increase in IRAP-pHluorin intensity in response to insulin in nocodazole-treated cells (Figure 3.13, Table 3.1). Therefore, microtubules do not appear to be required for transport of GLUT4 vesicles to the plasma membrane for fusion on the time scale of these experiments.

3.4.3 Microtubules may be specifying sites of GLUT4 vesicle fusion with the plasma membrane

This work represents the first quantitative evidence for a spatial correlation in 3T3-L1 adipocytes between sites of GLUT4 vesicle fusion with the plasma membrane and microtubules at the cell surface. Fusions of GLUT4 vesicles detected using IRAP-

pHluorin occur more closely to microtubules than would be expected for a random distribution (Figure 3.12). Most, though not all, fusions occur within ~ 0.5 µm from a microtubule (Figure 3.12). In part, detecting fusions occurring at greater distances from microtubules is due to a limitation in our ability to detect and segment microtubules, especially at high microtubule densities where the skeletonization process used to create the microtubule binary image tends to merge filaments that are close together.

Biologically, such an observation could also reflect that GLUT4-containing vesicles may belong either to the insulin-responsive pool of GLUT4 or the biochemically distinct pool of general endocytic vesicles that also contain GLUT4 (Martin *et al.*, 1996; Zeigerer *et al.*, 2002). These vesicle populations have different protein compositions, associated vSNAREs, and insulin sensitivities (Martin *et al.*, 1996; Zeigerer *et al.*, 2002). The IRAP-pHluorin construct used to detect fusions cannot distinguish between these populations of vesicles, and we cannot say whether there is a difference in the distribution of their fusions.

From our present work, it is clear that, although microtubules are not required for GLUT4 exocytosis, when microtubules are present, fusions of GLUT4 vesicles with the plasma membrane preferentially occur in proximity to them. Long-distance GLUT4 vesicle movements can readily be observed at the surface of 3T3-L1 adipocytes (Semiz *et al.*, 2003; Fujita *et al.*, 2010). However, we observed that only a small fraction of long-distance movements at the surface resulted in vesicle fusion (Movie 10). In addition, using TIRF microscopy, we rarely detected directed transport of GLUT4 vesicles that persisted for more than 1 µm along the filaments prior to fusion (Figure 3.14, Table 3.2). Long-distance movement on microtubules at the cell surface, therefore, does not appear to account for vesicle localization just prior to fusion in 3T3-L1 adipocytes. The situation

may be different in primary rat adipocytes where insulin halts GLUT4 vesicle trafficking along microtubules and promotes their fusion with the plasma membrane (Lizunov *et al.*, 2005). Differences are likely related to the fact that a large, centralized lipid droplet in primary adipocytes excludes the cytoplasm and confines it to a ~1-3 µm region between the plasma membrane and the lipid droplet (Lizunov *et al.*, 2005).

As microtubules at the membrane appear to be more important for specifying fusion site locations than for transporting GLUT4 vesicles (Figure 3.12, Table 3.2), they could be involved in the delivery, localization, or scaffolding of signaling components or fusion machinery. In support of this hypothesis, results from Eyster et al. suggesting that microtubule disruption inhibits Akt activation imply a role for microtubules in organizing the insulin signaling complex (Eyster *et al.*, 2006). Microtubules have also been proposed to regulate phosphatidylinositol 3-kinase activity during phagocytosis in macrophages (Khandani *et al.*, 2007), a process that shares with insulin-induced GLUT4 trafficking a requirement for Akt membrane recruitment and activation.

That microtubules could be playing a role in specifying fusion sites is an interesting possibility, and more work needs to be done to investigate this hypothesis. One potential approach is to examine whether a spatial correlation exists between microtubules and proteins involved in the initial interaction of GLUT4 vesicles with the plasma membrane. One potential candidate protein is Exo70, a component of the exocyst complex that has been proposed to tether GLUT4 vesicles at the plasma membrane prior to fusion (Lizunov *et al.*, 2009). Preliminary experiments, however, did not reveal a spatial correlation of GFP-Exo70 puncta with either microtubules or mCherry-IRAP (Figure 3.15A-B). For further discussion of why fusions might be occurring near microtubules, see section 3.5.2 [Question 5] below.

3.5 CONCLUDING REMARKS

For a discussion of the role of microtubules in GLUT4 vesicle trafficking and future directions for this work see section 4.2 [Microtubules in GLUT4 vesicle trafficking] below.

3.5.1 Acknowledgments

We thank Dr. Yujie Sun for assistance with Parallax microscopy, Drs. Yujie Sun and Adam Hendricks for assistance with the Nikon TIRF set-up, and Dr. Martin Pring for helpful discussions. For DNA constructs used in this paper, we thank: Dr. Samuel Cushman (HA-GLUT4-eGFP), Dr. David James (IRAP-pHluorin), Dr. Roger Tsien (mCherry-human-α-Tubulin), Dr. Chloë Bulinski (3xGFP-EMTB), and Dr. Erika Holzbaur (GFP-CC1 p150^{Glued}). We thank Dr. Morris Birnbaum for 3T3-L1 mouse fibroblasts. JMDM was supported by a training grant from the NIH (GM07229) and a pre-doctoral fellowship from the American Heart Association. This work was also supported through a program project grant from the NIH (P01 GM087253) to YEG and EMO.

Chapter 4. Concluding Remarks

4.1 Myo1c in GLUT4 vesicle trafficking

The recent finding that myo1c plays a role in the insulin-stimulated trafficking of GLUT4 vesicles (Bose *et al.*, 2002; Bose *et al.*, 2004) represents an important opportunity to understand in greater detail the function of myo1c in the cell. Section 1.1 [Specific Aims] enumerates several potential models for the involvement of myo1c (Figure 1.1). A major difference among these models is whether myo1c functions in short-range vesicle transport (Figure 1.1, (1 and 2)) or instead as an anchor or tether (Figure 1.1, (3)). A second open question is the site of action of myo1c. While there is evidence that myo1c is recruited to GLUT4 vesicles (Bose *et al.*, 2002), myo1c is also enriched at the plasma membrane and may act there to, for example, affect membrane tension (Figure 1.1, (4)).

Therefore, the first part of this thesis examined how membrane phosphoinositide and anionic composition influence myo1c membrane attachment lifetime. An understanding of myo1c attachment lifetime is important for a number of reasons. First, understanding how lipid composition influences the kinetics of myo1c membrane binding could give some indication of the sites of action for myo1c in the absence of protein-protein interactions since the phosphoinositide content of GLUT4 vesicles is expected to differ from that of the plasma membrane. Second, it will provide insight into the mechanism of myo1c recruitment to GLUT4 vesicle membranes. For example, as discussed in section 4.1.1 below, short attachment lifetimes could indicate that a protein-protein interaction functions to stabilize myo1c membrane attachment. Section 4.1.2,

meanwhile, discusses whether myo1c is capable of transporting cargo along actin filaments.

4.1.1 Potential anchoring of myo1c at the membrane through protein-protein interactions

In the absence of force, data from this thesis shows that the lifetime of myo1c attachment to physiological membranes (i.e., membrane containing PtdIns(4,5)P_2 and additional anionic charge) is long enough for myo1c to complete several catalytic cycles (Figure 2.4). In a continuation of the work described here, further investigations in the Ostap lab sought to address the question of how much force is required to detach myo1c from the membrane. Pyrpassopoulos et al. found that myo1c attachment to PtdIns(4,5)P_2-containing membranes can withstand 6 – 16 pN of force (Pyrpassopoulos *et al.*, 2010). To put this in perspective, the force required for membrane detachment is greater than the force needed to stall myosin-I motor activity (Laakso *et al.*, 2008; Laakso *et al.*, 2010), supporting the argument that myo1c is suitable from a mechanical point of view to act as a linkage to cell membranes. However, force significantly reduced the lifetime of the attachment of myo1c to PtdIns(4,5)P_2-containing membranes (Pyrpassopoulos *et al.*, 2010).

One question raised by this finding is whether myo1c interacts with proteins that could provide an additional membrane anchor for myo1c. A few protein-protein interactions involving myo1c have been suggested. Proposed myo1c-interacting proteins include NEMO, PHR1, RalA, and cadherin 23 (Chen *et al.*, 2007; Etournay *et al.*, 2005; Nakamori *et al.*, 2006; Phillips *et al.*, 2006). Interestingly, PHR1 and cadherin

23 are integral membrane proteins (Etournay *et al.*, 2005; Siemens *et al.*, 2004), and RalA is recruited to cellular membranes through the post-translational addition of an isoprenyl group to a cysteine in the C-terminus (Kinsella *et al.*, 1991).

RalA as a potential membrane anchor for myo1c

Myo1c was identified as a RalA-interacting protein through immunoprecipitation of RalA from adipocytes followed by mass spectroscopy (Chen *et al.*, 2007). Truncation mapping of myo1c identified the myo1c IQ motifs as important in mediating the interaction with RalA, which was reported to be calcium-sensitive and regulated by calmodulin binding (Chen *et al.*, 2007). What makes RalA, a small GTPase, an attractive candidate for study is that both RalA and myo1c have been reported to be important in the trafficking of GLUT4-containing vesicles in response to insulin (see section 1.1 [Specific Aims] for a review of the role of myo1c). Since RalA is activated in response to insulin and is localized to insulin-sensitive, GLUT4-containing vesicles, RalA has been proposed to serve as a cargo receptor for myo1c during GLUT4 vesicle trafficking (Chen *et al.*, 2007).

It remains an open question, however, whether interaction of myo1c with isoprenylated RalA could help to keep myo1c associated to GLUT4 vesicles under force. One caveat to this proposal is that it is not clear whether the interaction between RalA and myo1c is direct. The immunoprecipitations described above were carried out in adipocyte lysates (Chen *et al.*, 2007), raising the possibility that an unidentified cellular factor mediates the interaction. *In vitro* binding studies were performed with myo1c translated *in vitro* in the absence of calmodulin (Chen *et al.*, 2007), conditions that promote myo1c aggregation and non-specific binding.

In preliminary studies, I attempted to confirm a direct interaction *in vitro* using purified GST-RalA and either biotinylated-myo1c$^{motor\text{-}IQ}$ or His-myo1c$^{IQ\text{-}tail}$, both of which contain all three IQ motifs. Myo1c was purified from *Sf9* cells in the presence of calmodulin, conditions more appropriate for myo1c purification. I failed to detect an interaction (data not shown), although it remains possible that the interaction is direct but low affinity. Failure to detect a high affinity *in vitro* interaction does not rule out a biologically significant *in vivo* interaction between myo1c and isoprenylated-RalA that is potentially stabilized by myo1c membrane binding to GLUT4 vesicles. By providing multiple binding sites for myo1c, GLUT4 vesicles could in theory recruit multiple myo1c molecules, allowing vesicles to remain associated to actin filaments over longer periods of time (see below, *Myo1c in cargo transport*).

4.1.2 Myo1c in cargo transport

A second question regarding the role of myo1c as a molecular motor is whether myo1c is capable of transporting cargo along actin filaments. The question arises because myo1c is single-headed and spends only a small fraction of its ATPase cycle strongly-bound to actin in the absence of force. Individual myo1c molecules would dissociate from actin filaments rather than moving processively along them. One possibility is that multiple myosins bound to the same cargo, such as vesicles or protein complexes with multiple myo1c binding sites, could effectively increase the amount of time the cargo stays associated with actin. Dissociation from the actin filament would be based on the probability of all myosins being detached from actin at once. Called the effective duty ratio, this principle has been demonstrated by Spudich and others who have shown a myosin concentration dependence of actin gliding along a surface coated

with low duty ratio motors (Uyeda *et al.*, 1990). The ability of multiple low duty ratio motors to transport cargo, however, has not been directly demonstrated.

NEMO as a potential scaffold for recruitment of myo1c in cargo transport

Recently, myo1c has been reported to play a role in the insulin-induced translocation of NEMO, a component of the IκB kinase (IKK) complex (Rothwarf *et al.*, 1998), from the cytosol to membrane ruffles in 3T3-L1 adipocytes (Nakamori *et al.*, 2006). Translocation is dependent upon intact actin filaments but not microtubules, as latrunculin B but not nocodazole treatment of cells disrupted translocation (Nakamori *et al.*, 2006). In addition, siRNA of myo1c and expression of a myo1c protein lacking the motor domain inhibited NEMO translocation (Nakamori *et al.*, 2006).

Pull-down assays using cell lysates demonstrate that myo1c and NEMO interact *in vivo*, and insulin increases this interaction. *In vitro* binding of recombinant proteins suggests that the interaction is direct. Interestingly, NEMO possesses coiled-coil domains important for homo-oligomerization into trimers (Agou *et al.*, 2004) or tetramers ((Tegethoff *et al.*, 2003)). Oligomerization of NEMO could generate multiple myo1c binding sites on the same complex, raising the question of whether NEMO could act as a scaffold for the recruitment of multiple myo1c molecules to transport NEMO as cargo.

While this is an interesting proposal, the evidence of a direct interaction is compromised by the fact that the myo1c used in the study was expressed in bacteria (Nakamori *et al.*, 2006), which is not an appropriate expression system for this myosin. As with RalA, my preliminary *in vitro* pull-down studies attempting to confirm a direct interaction between NEMO and myo1c purified from *Sf9* cells failed (data not shown).

Again, my pull-down experiments would likely not have detected a low-affinity, direct interaction. It remains possible that oligomerization of NEMO could recruit multiple myo1c molecules in cells, where other potential protein-protein interactions could stabilize the interaction of myo1c with NEMO. However, the NEMO-myo1c interaction is not an ideal *in vitro* system to investigate whether an increase in the effective duty ratio could enable myo1c to transport cargo.

4.2 Microtubules in GLUT4 vesicle trafficking

In preparation for understanding the role of myo1c in GLUT4 vesicle trafficking, the second part of this thesis examined microtubule localization and dynamics in adipocytes and the spatial relationship between microtubules and GLUT4 vesicle fusions with the plasma membrane. Such information is important since it is clear that GLUT4 vesicles move long-distances on microtubules (Figure 3.14, Movie 10), and, due to the arrangement of the microtubule cytoskeleton in 3T3-L1 adipocytes, such movements could displace GLUT4 vesicles from potential fusion sites at the cell surface. One potential role for myo1c, therefore, is to inhibit microtubule-dependent displacement of GLUT4 vesicles away from the cell surface by tethering the vesicle to cortical actin (Figure 1.1 (2 and 3)).

4.2.1 Model for the role of microtubules in GLUT4 trafficking

Microtubules may be contributing to the efficiency of GLUT4 vesicle mobilization in response to insulin, and the preceding increase in microtubule density (Figure 3.5A, Table 3.1) could possibly enhance this contribution. In support of such a role, we (Figure 3.5B, Table 3.1) and others (Karylowski *et al.*, 2004; Liu *et al.*, 2003; Huang *et al.*, 2005; Olson *et al.*, 2003; Emoto *et al.*, 2001) observe a modest reduction in GLUT4 surface accumulation in cells pre-treated with nocodazole. In addition, we also report a delay in the GLUT4 time course and the introduction of a time-lag upon microtubule disruption (Figure 3.5B inset, Table 3.1). It is worth noting that the reduction in GLUT4 accumulation at the surface might be offset to some degree by the dispersal of

perinuclear GLUT4 compartments when microtubules are disrupted (Guilherme *et al.*, 2000; Shigematsu *et al.*, 2002).

In contributing to the efficiency of GLUT4 vesicle mobilization to the cell surface, we can speculate that microtubules centrally located within the adipocyte, which can be several tens of micrometers thick, may serve as tracks for vesicle movement. However, the contribution of microtubules to the increase in GLUT4 at the cell surface appears to be modest (Figure 3.5, Table 3.1), and we hypothesize that the long-distance movement of GLUT4 vesicles from the center of the cell to the periphery is not the main role for microtubules in GLUT4 trafficking. Our results also suggest that the primary function of surface-localized microtubules is not to serve as transport filaments along which GLUT4 vesicles translocate prior to fusion. While we observe long-distance movements along microtubules using TIRF microscopy, for example, few of these movements end with vesicle fusion (Movie 10). In addition, while GLUT4 vesicle fusions preferentially occur near microtubules (Figure 3.12), very few of the fusions are preceded by observed displacements of more than 1 µm (Table 3.2).

Instead, we hypothesize that microtubules may be important in specifying sites of GLUT4 vesicle fusion with the plasma membrane. For example, microtubules could be serving as scaffolds for the organization of signaling or fusion machinery. Such a possibility is interesting, especially given that the primary site of insulin regulation is now thought to occur at the plasma membrane (Lizunov *et al.*, 2005; Huang *et al.*, 2007; Bai *et al.*, 2007) (reviewed in (Eyster and Olson, 2009)). In primary adipocytes, Exo70, a component of the exocyst complex, has been proposed to tether GLUT4 vesicles at the plasma membrane prior to fusion in a manner that prevents GLUT4 vesicle translocation along surface-localized microtubules (Lizunov *et al.*, 2009). It will be interesting to examine whether a spatial correlation exists between microtubules and proteins involved

in the initial interaction of GLUT4 vesicles with the plasma membrane, such as Exo70. For further discussion, see section 4.2.2 [Question 5] below.

Once GLUT4 vesicles have reached the plasma membrane, microtubules are clearly not required for GLUT4 externalization since fusions take place in the presence of nocodazole (Figure 3.13). Vesicle fusion is a SNARE-dependent process (reviewed in (Bryant and Gould, 2011)), and there is some evidence that GLUT4 vesicle tethering is mediated through the exocyst complex (Inoue *et al.*, 2003; Ewart *et al.*, 2005; Lizunov *et al.*, 2009).

However, while microtubules are not required for the process of exocytosis itself, it is interesting to speculate that the increased microtubule curvature and density at the cell surface following insulin stimulation contributes to the increase in GLUT4 inserted into the plasma membrane. This could result from an increase in the number of potential fusion sites itself. Alternatively, microtubules may be important for increasing the fraction of GLUT4 vesicles in proximity to fusion-competent sites at the plasma membrane.

The increase in microtubule curvature may also reflect an increase in the number of motors engaged on GLUT4 vesicles as discussed in section 4.2.2 [Question 3] below. It is of note that microtubules in 3T3-L1 adipocytes often appear to slide in relation to each other (Movie 4) or to the plasma membrane (Movie 5). Additionally, microtubules appear to be threaded through fixed locations on the cell surface to form loops that translocate relative to the cell membrane (Movie 3). One intriguing possibility is that motors act at these nodal points or function to cross-link microtubules. Such dynamics may serve to prolong or enhance the localization of microtubules at the cell surface, as discussed in section 4.2.2 [Question 3] below, which could in turn have an influence on GLUT4 vesicle localization to the cell surface. Furthermore, fusions, at least in some

cells, appear to occur frequently at microtubule-microtubule intersections (Movie 9), which could indicate a tug-of-war of motors engaged on the same vesicle (Ross *et al.*, 2008). One possibility is that such intersections could prevent the movement of GLUT4 vesicles away from the plasma membrane. Microtubule dynamics, therefore, might be tuned in 3T3-L1 adipocytes to facilitate an increase in GLUT4 at the plasma membrane.

4.2.2 Future Directions

There are several interesting questions arising from this work that will be of interest to both the GLUT4 and the cytoskeletal fields. In this section, I discuss these questions and briefly propose experiments to address several of them. I conclude with some recommendations for optimizing the adipocyte system I have been using.

Question 1: How does insulin signaling lead to an increase in microtubule surface density? What are the targets of insulin signaling to microtubules?

As a first approach to dissecting signaling leading to increased microtubule polymerization, chemical inhibitors could be used to target different proteins involved in the insulin signaling pathway. For example, wortmannin inhibits PI3K and is useful in distinguishing PI3K-dependent and independent events. Next, proteins downstream of PI3K-dependent or independent signaling could be targeted. Once chemical inhibition has identified potential candidates, follow-up experiments would involve inactivation of the candidate proteins at a genetic level through siRNA. Mechanistically, insulin signaling could lead to an increase in microtubule density through an increase in microtubule polymerization, a decrease in depolymerization, or an increased number of microtubule plus ends through an increase in nucleation sites. It is not clear at this time which of these mechanisms insulin targets.

Identifying signaling pathways leading to microtubule density increase may prove to be impractical at the single cell level given the low throughput nature of single cell imaging, especially if the degree of cell heterogeneity is high. An alternative method is to assay the amount of polymerized tubulin across entire monolayers of 3T3-L1 adipocytes through differential extraction of monomeric and polymerized tubulin, as has

been previously described (Olson *et al.*, 2003). While this method would permit the assessment of many cells in parallel, a disadvantage is that information about microtubule polymerization at the cell surface would be lost.

Question 2: What mechanism is responsible for the observed microtubule bending dynamics?

A striking feature of microtubules in 3T3-L1 adipocytes is that a population of them is highly curved (Figures 3.6A and 3.8A, Movie 2) and that forces act on them, displacing microtubules relative to the membrane (Figure 3.9, Movies 3 – 7). We have ruled out polymerization-induced buckling, dynein-dynactin activity, and actin-dependent processes (Figure 3.8B-D, Movie 8) as potential mechanisms. An obvious remaining alternative is that a kinesin is responsible. Two kinesins in particular have been previously reported to play a role in GLUT4 vesicle trafficking: a kinesin II (KIF3) and kinesin I (KIF5B). In addition, kinesin-1 heavy chain mediates microtubule-microtubule sliding and is responsible for observed microtubule looping in other cell types (Jolly *et al.*, 2010).

siRNA or dominant-negative constructs could be used to target these kinesins. Because of the low efficiency of transfection in 3T3-L1 adipocytes, oligos or constructs would need to be tagged with a fluorophore to identify successfully transfected cells. In preliminary experiments, we have co-transfected adipocytes with mCherry-Tubulin and GFP-labeled dominant negative KIF3a and KIF5 constructs. In cells positive for GFP expression, we did not observe a disruption in microtubule curvature (Figure 3.8). To rule out involvement of these kinesins, however, it will be important to first confirm their

disruption in GFP-positive cells. It is also possible that another kinesin may instead be responsible.

Question 3: Are the increase in microtubule surface density and the increased microtubule bending linked mechanistically?

Section 3.4.1 [Microtubule curvature and surface density may be mechanistically linked] proposes that there could be a relationship between the observed increase in surface density and bending of microtubules. Pulling of microtubules toward the cell surface could be a potential mechanism linking the two processes. As mentioned above, this could be mediated through a kinesin.

Such a mechanism raises the question of whether an increase in motor recruitment to GLUT4 vesicles or activation leads to increased pulling following insulin stimulation or whether this simply reflects the availability of more microtubules on which motors act. The microtubule curvature increase following insulin stimulation (Figure 3.6), suggests more than an increase in microtubules alone. Additionally, there is some evidence for an increase in recruitment of microtubule motors to GLUT4 vesicles (Imamura *et al.*, 2003; Semiz *et al.*, 2003; Lalioti *et al.*, 2009).

Even if there is an increase in motor recruitment or activation, a question remains about whether a separate mechanism is required to maintain, stabilize, or anchor microtubules at the plasma membrane following microtubule pulling to the cell surface. For example, stromal interacting molecule 1 (STIM1), an endoplasmic reticulum transmembrane protein, has been proposed to play a role in microtubule reorganization following activation of mast cells, presumably through its interaction with EB1 (Hájková *et al.*, 2011). Similarly, a membrane-localized protein could interact with microtubules or

a microtubule-interacting protein to maintain microtubules at the cell surface following insulin stimulation in 3T3-L1 adipocytes.

Question 4: Is the microtubule density increase in response to insulin important for mobilizing GLUT4?

We observed that microtubule density increased in response to insulin stimulation and the increase preceded the accumulation of GLUT4 at the cell surface (Figure 3.5A, Table 3.1). This raises the question of whether microtubule density increase is relevant to GLUT4 trafficking. There are several possibilities, including: (1) density increase is a by-product of insulin signaling with no consequence for GLUT4 cell surface increase; (2) density increase may be important in retrieval of vesicles following GLUT4 endocytosis; (3) density increase may be relevant at the level of GLUT4 vesicle docking or fusion; (4) density increase assists in mobilizing GLUT4 vesicles to the plasma membrane; (5) density increase is important in the context of the native, 3-dimensional environment of adipocytes where the lipid is organized into a single, centralized droplet, a feature that our experimental system does not replicate.

The fourth suggestion- that the availability of more tracks could contribute to an increase in vesicle motility and mobilization of GLUT4 to the membrane- is an intriguing possibility, especially in light of work in 3T3-L1 adipocytes showing an increase in the fraction of mobile vesicles (Fujita *et al.*, 2010). Of course, release of vesicles from a retention mechanism (Bogan *et al.*, 2003), activation, or recruitment of motors (Imamura *et al.*, 2003; Semiz *et al.*, 2003; Lalioti *et al.*, 2009) could also be important. These mechanisms are not mutually exclusive.

Addressing this question will require some way of uncoupling the two insulin-dependent processes. It would be informative to stimulate GLUT4 translocation without affecting microtubule density, and ask how the time course of the GLUT4 intensity increase was affected. To accomplish this, however, additional information about how insulin signals to the microtubule cytoskeleton will be required. Existing evidence suggests that microtubule density increase occurs through a PI3K-independent, actin-dependent pathway (Olson *et al.*, 2003).

Question 5: Why are fusions taking place in proximity to microtubules in the absence of long-distance transport at the surface?

While GLUT4 vesicle fusions occur closer to microtubules than would be expected for a random distribution (Figure 3.12), very few long-distance movements observed at the cell surface result in fusion (Table 3.2 and Movie 10). This surprising finding raises the question of why fusions preferentially occur near microtubules. In terms of insulin-stimulated GLUT4 trafficking, this is the major question raised by the present work. One hypothesis is that not all of the plasma membrane may be equally permissive for vesicle fusion to take place, and the membrane in the vicinity around microtubules may have specialized features. For example, microtubules may be important in organizing the insulin signaling machinery, as suggested by Eyster et al., who report deficient Akt phosphorylation when microtubules are depolymerized (Eyster *et al.*, 2006). Alternatively, microtubules may be important for the localization of vesicle tethering or fusion machinery.

To examine whether a spatial correlation exists between microtubules and Exo70, I have co-expressed GFP-Exo70 and either mCherry-tubulin or mCherry-IRAP in

3T3-L1 adipocytes in preliminary experiments. I did not observe a spatial correlation of Exo70 puncta with either microtubules or with mCherry-IRAP, which was used to visualize GLUT4 vesicles (Figure 3.15A-B). Fusions could be detected with the mCherry-IRAP construct, although not as easily as with the IRAP-pHluorin construct since there is no increase in mCherry intensity upon vesicle fusion. Still, there was no obvious spatial correlation between GLUT4 vesicles that fused with the plasma membrane and GFP-Exo70 (Figure 3.15B). My findings do not rule out a transitory interaction of Exo70 with GLUT4 vesicles that ultimately fuse, which I might have failed to detect.

An alternate explanation is that the spatial distribution of microtubules at the plasma membrane is somehow restricted or that microtubule localization is stabilized in areas where vesicle fusions take place, possibly through localization of membrane-associated microtubule-interacting proteins. It is also worth noting that GLUT4 vesicles display what could be interpreted as an affinity for microtubules. Using TIRF microscopy, for example, many vesicles appear to be immobilized at microtubules without any translocation during the acquisition. In addition, some vesicles appeared to change velocity and direction repeatedly and rapidly. Upon approach to a microtubule visible in TIRF microscopy, however, the vesicles often ceased moving for some period of time before continuing this motion and moving away from the microtubule.

Recommendations for optimization

Higher resolution imaging of individual living cells provides advantages over fixed cell imaging or live cell imaging at lower resolution. Information about vesicle dynamics and positional correlation of vesicles with cell structures cannot be obtained from these

other methods. There is clearly value to using higher resolution approaches, and without this approach I could not have produced several of my major findings.

One experiment that could benefit from lower resolution, however, is the comparison of the GLUT4 and IRAP time courses with and without drug treatment. Part of the problem is the large cell-cell variability. As a result, the errors associated with these time courses are large; increasing the number of observations may decrease the uncertainty in these measurements. Experiments were conducted on an objective-based TIRF system. The high numerical aperture objective required for this system also had a high magnification, limiting the field of view to a single cell. A prism-based TIRF system with a low magnification objective could provide an alternative approach and increase the throughput of the system. Such a system has previously been used to study the insulin response of many 3T3-L1 adipocytes in parallel (Tengholm *et al.*, 2003).

A second difficulty I encountered was low transfection efficiency. Electroporation typically resulted in a very small percentage of cells transfected, in keeping with the efficiency found by others working with this cell type. While this method is the field standard- other methods such as Lipofectamine produce even poorer results- such low transfection efficiency makes finding appropriate cells difficult. Alternatives to transient transfection include the use of viruses such as adenovirus. I have avoided this method because of concern about the effects of viral delivery on the cytoskeleton. Another option is creation of stable cell lines. While there are drawbacks associated with this method- the long period of selection results in increased passage number and the process must be repeated for each construct of interest- cell lines expressing a fluorescently-tagged GLUT4 have been created (Shi *et al.*, 2008).

An alternative would be to use primary rat adipocytes. While these cells may not be easier to transfect, they have been reported to be less variable than cultured 3T3-L1 adipocytes. Also, the organization of their lipid is different. Instead of disperse, smaller droplets found in 3T3-L1 adipocytes, primary adipocytes have a single, large, centrally-located lipid droplet. The cell architecture confines the cytoplasm to a region within ~1-3 µm of the plasma membrane (Lizunov *et al.*, 2005) and necessitates a different arrangement of the cytoskeleton.

APPENDICES

Movie Legends

Movie 1. Insulin stimulation increases the intensity of HA-GLUT4-eGFP at the cell surface.

Adipocyte transfected with HA-GLUT4-eGFP was serum-starved prior to stimulation with 100 nM insulin at t = 0 min. TIRF images were acquired at 1 frame per 10 s. Scale bar is 15 µm. Movie corresponds to Figure 3.3A.

Movie 2. Microtubule density increases upon insulin stimulation.

Adipocyte transfected with mCherry-tubulin was serum-starved prior to stimulation with 100 nM insulin at t = 0 min. TIRF images were acquired at 1 frame per 10 s. Scale bar is 10 µm. Movie corresponds to Figure 3.6.

Movie 3. Microtubule loops are formed in 3T3-L1 adipocytes.

Adipocyte was transfected with mCherry-tubulin. TIRF images were acquired at 1 frame per 10 s. Elapsed time is indicated in min:sec. Scale bar is 2 µm.

Movie 4. Microtubule sliding occurs relative to other microtubules in 3T3-L1 adipocytes.

Adipocyte transfected with 3xGFP-EMTB was serum-starved prior to stimulation with 100 nM insulin. TIRF images were acquired ~5 min following insulin stimulation at an acquisition rate of 20 frames per 1 s. Background-subtraction was performed. Elapsed time is indicated in min:sec. Scale bar is 2 µm.

Movie 5. Microtubule gliding can be observed at the surface of 3T3-L1 adipocytes.

Adipocyte transfected with GFP-tubulin was starved prior to stimulation with 100 nM insulin. TIRF images were acquired ~10 minutes following insulin stimulation at 1 frame per s. Elapsed time is indicated in min:sec. Background-subtraction and smoothing were performed. Scale bar is 5 µm.

Movie 6. 2-Dimensional view of microtubule dynamics.

Adipocyte transfected with 3xGFP-EMTB was imaged using Parallax microscopy. One of a pair of 2-dimensional images is shown. TIRF images were acquired at 1 frame per 10 s. Background-subtraction was performed. Elapsed time is indicated in min:sec. Scale bar is 2 µm. Movie corresponds to Figure 3.9.

Movie 7. 3-Dimensional view of microtubule dynamics.

Microtubule from Figure 3.9 and Movie 6 is plotted as a series of (x,y,z) coordinates. Relative z-depth is color-coded with 0 (deep red) being the closest approach of the microtubule to the coverslip. For ease of viewing microtubule movements, frames have been interpolated in time. Elapsed time is 3 min 20 s.

Movie 8. Microtubule curvature and displacement dynamics at the cell surface remain following initial treatment with a low dose of nocodazole.

Adipocyte transfected with mCherry-tubulin was treated with 2 µM nocodazole at t = 0 min. TIRF images were acquired at 1 frame per 20 s. Scale bar is 10 µm. Movie corresponds to Figure 3.8.

Movie 9. IRAP-pHluorin fusions with the plasma membrane occur in proximity to microtubules.

Adipocyte transfected with mCherry-IRAP-pHluorin and 3xGFP-EMTB was serum-starved prior to stimulation with 100 nM insulin. TIRF images were acquired ~4 minutes following insulin stimulation at an acquisition rate of 9 frames per 1 s with 488 nm excitation and a 530df30 BP filter. Elapsed time is indicated in min:sec. Scale bar is 5 µm. Movie corresponds to Figure 3.11.

Movie 10. Long-distance movements of GLUT4 vesicles at the cell surface rarely culminate in fusion with the plasma membrane.

Adipocyte transfected with mCherry-IRAP-pHluorin was serum-starved prior to stimulation with 100 nM insulin. TIRF images were acquired ~4 minutes following insulin stimulation at an acquisition rate of 20 frames per 1 s. GLUT4 vesicles are visible as magenta puncta. An increase in pHluorin fluorescence (green) indicates vesicle fusion with the plasma membrane. The fusing vesicle briefly appears white (magenta + green) before the fluorescence becomes diffuse as mCherry-IRAP-pHluorin disperses within the membrane. Elapsed time is 50 s. Scale bar is 10 µm.

Abbreviations

AEDANS-PLCδ-PH, PLCδ-PH labeled with IAEDANS

ARNO, ADP-ribosylation factor nucleotide-binding site opener

AS160, Akt substrate of 160 kDa

CaBP1, calcium-binding protein 1

CCF, cosine correlation function

CIB1, calcium- and integrin-binding protein 1

CytoD, cytochalasin D

DLS, Dynamic Light Scattering

DOPC, phosphatidylcholine

DOPS, phosphatidylserine

EMTB, ensconsin microtubule-binding domain

FBS, fetal bovine serum

GAP, GTPase activating protein

GLUT4, glucose transporter-4

GRP1, glycine-rich protein 1

HNa100, 10 mM HEPES, pH7, 100 mM NaCl, 1 mM EGTA, and 1 mM DTT

IAEDANS, 5-((((2-iodoacetyl)amino)ethyl)amino)naphthalene-1-sulfonic acid

IKK, IκB kinase

$InsP_3$, inositol 1,4,5-trisphophate

$InsP_6$, phytic acid

IR, insulin receptor

IRAP, insulin-regulated aminopeptidase

IRS1/2, insulin receptor substrate 1/2

LatB, latrunculin B

LRP1, lipoprotein receptor-related protein 1

LUVs, large unilamellar vesicles

MARCKS, myristoylated alanine-rich protein kinase C substrate

MT, microtubule

NEMO, NF-κB essential modulator

Noc, nocodazole

PBS, phosphate-buffered saline

PC, phosphatidylcholine

PE, phosphatidylethanolamine

PH, pleckstrin homology

pHluorin, a pH-sensitive GFP variant

PHR1, pleckstrin homology domain retinal protein 1

PI, phosphatidylinositol

PI3K, phosphatidylinositol-3 kinase

PLCδ, phospholipase-Cδ

POPC, phosphatidylcholine

POPE, phosphatidylethanolamine

POPS, phosphatidylserine

PS, phosphatidylserine

PtdIns(3,4,5)P_3, phosphatidylinositol-3,4,5-trisphosphate

PtdIns(4,5)P_2, phosphatidylinositol 4,5-bisphosphate

RIA-BSA, radioimmuno assay-grade bovine serum albumin

SM, sphingomyelin

SNARE, soluble *N*-ethylmaleimide-sensitive factor attachment protein receptors

STIM1, stromal interacting molecule 1

Tf-R, transferrin receptor

TH, tail homology domain

TIRF, Total Internal Reflection Fluorescence microscopy

VAMP, vesicle-associated membrane protein

vSNARE, vesicle SNARE

BIBLIOGRAPHY

Adams, R. J. and Pollard, T. D. (1989). Binding of myosin I to membrane lipids. Nature *6234*, 565-8.

Agou, F., Traincard, F., Vinolo, E., Courtois, G., Yamaoka, S., Israel, A. and Veron, M. (2004). The trimerization domain of NEMO is composed of the interacting C-terminal CC2 and LZ coiled-coil subdomains. J. Biol. Chem. *27*, 27861-27869.

Bai, L., Wang, Y., Fan, J., Chen, Y., Ji, W., Qu, A., Xu, P., James, D. E. and Xu, T. (2007). Dissecting Multiple Steps of GLUT4 Trafficking and Identifying the Sites of Insulin Action. Cell Metabolism *1*, 47-57.

Basu, R. and Chang, F. (2007). Shaping the actin cytoskeleton using microtubule tips. Curr. Opin. Cell Biol. *1*, 88-94.

Bell, G. I., Burant, C. F., Takeda, J. and Gould, G. W. (1993). Structure and function of mammalian facilitative sugar transporters. Journal of Biological Chemistry *26*, 19161-19164.

Berg, J. S., Powell, B. C. and Cheney, R. E. (2001). A millennial myosin census. Mol. Biol. Cell *4*, 780-794.

Bogan, J. S., Hendon, N., McKee, A. E., Tsao, T. S. and Lodish, H. F. (2003). Functional cloning of TUG as a regulator of GLUT4 glucose transporter trafficking. Nature *6959*, 727-733.

Bogan, J. S. and Kandror, K. V. (2010). Biogenesis and regulation of insulin-responsive vesicles containing GLUT4. Curr. Opin. Cell Biol. *4*, 506-512.

Bose, A., Guilherme, A., Robida, S. I., Nicoloro, S. M., Zhou, Q. L., Jiang, Z. Y., Pomerleau, D. P. and Czech, M. P. (2002). Glucose transporter recycling in response to insulin is facilitated by myosin Myo1c. Nature *6917*, 821-824.

Bose, A., Robida, S., Furcinitti, P. S., Chawla, A., Fogarty, K., Corvera, S. and Czech, M. P. (2004). Unconventional myosin Myo1c promotes membrane fusion in a regulated exocytic pathway. Mol. Cell. Biol. *12*, 5447-5458.

Bryant, N. J. and Gould, G. W. (2011). SNARE proteins underpin insulin-regulated GLUT4 traffic. Traffic *6*, 657-664.

Brzeska, H., Hwang, K. and Korn, E. D. (2008). Acanthamoeba Myosin IC Colocalizes with Phosphatidylinositol 4,5-Bisphosphate at the Plasma Membrane Due to the High Concentration of Negative Charge. Journal of Biological Chemistry *46*, 32014-32023.

Cain, C. C., Trimble, W. S. and Lienhard, G. E. (1992). Members of the VAMP family of synaptic vesicle proteins are components of glucose transporter-containing vesicles from rat adipocytes. Journal of Biological Chemistry *17*, 11681-11684.

Chen, X. W., Leto, D., Chiang, S. H., Wang, Q. and Saltiel, A. R. (2007). Activation of RalA is required for insulin-stimulated Glut4 trafficking to the plasma membrane via the exocyst and the motor protein Myo1c. Dev Cell *3*, 391-404.

Chen, Y., Wang, Y., Ji, W., Xu, P. and Xu, T. (2008). A pre-docking role for microtubules in insulin-stimulated glucose transporter 4 translocation. FEBS J. *4*, 705-712.

Chiu, T. T., Patel, N., Shaw, A. E., Bamburg, J. R. and Klip, A. (2010). Arp2/3- and Cofilin-coordinated Actin Dynamics Is Required for Insulin-mediated GLUT4 Translocation to the Surface of Muscle Cells. Molecular Biology of the Cell *20*, 3529-3539.

Chung le, T. K., Hosaka, T., Harada, N., Jambaldorj, B., Fukunaga, K., Nishiwaki, Y., Teshigawara, K., Sakai, T., Nakaya, Y. and Funaki, M. (2010). Myosin IIA participates in docking of Glut4 storage vesicles with the plasma membrane in 3T3-L1 adipocytes. Biochem. Biophys. Res. Commun. *1*, 995-999.

Collins, J. H. and Swanljung-Collins, H. (1992). Calcium regulation of myosin I--a motor for membrane movement. Adv Exp Med Biol, 159-63.

Corbin, J. A., Dirkx, R. A. and Falke, J. J. (2004). GRP1 pleckstrin homology domain: activation parameters and novel search mechanism for rare target lipid. Biochemistry *51*, 16161-73.

Cushman, S. W. and Wardzala, L. J. (1980). Potential mechanism of insulin action on glucose transport in the isolated rat adipose cell. Apparent translocation of intracellular transport systems to the plasma membrane. Journal of Biological Chemistry *10*, 4758-4762.

Dawson, K., Aviles-Hernandez, A., Cushman, S. W. and Malide, D. (2001). Insulin-regulated trafficking of dual-labeled glucose transporter 4 in primary rat adipose cells. Biochem Biophys Res Commun *2*, 445-54.

De La Cruz, E. M. and Ostap, E. M. (2004). Relating biochemistry and function in the myosin superfamily. Curr. Opin. Cell Biol. *1*, 61-67.

Dove, S. K. *et al.* (2004). Svp1p defines a family of phosphatidylinositol 3,5-bisphosphate effectors. EMBO J *9*, 1922-33.

Emoto, M., Langille, S. E. and Czech, M. P. (2001). A role for kinesin in insulin-stimulated GLUT4 glucose transporter translocation in 3T3-L1 adipocytes. J Biol Chem *14*, 10677-82.

Espreafico, E. M., Cheney, R. E., Matteoli, M., Nascimento, A. A., De Camilli, P. V., Larson, R. E. and Mooseker, M. S. (1992). Primary structure and cellular localization of chicken brain myosin-V (p190), an unconventional myosin with calmodulin light chains. J Cell Biol *6*, 1541-57.

Etournay, R. *et al.* (2005). PHR1, an integral membrane protein of the inner ear sensory cells, directly interacts with myosin 1c and myosin VIIa. J Cell Sci *Pt 13*, 2891-9.

Ewart, M., Clarke, M., Kane, S., Chamberlain, L. H. and Gould, G. W. (2005). Evidence for a Role of the Exocyst in Insulin-stimulated Glut4 Trafficking in 3T3-L1 Adipocytes. Journal of Biological Chemistry *5*, 3812-3816.

Eyster, C. A., Duggins, Q. S., Gorbsky, G. J. and Olson, A. L. (2006). Microtubule network is required for insulin signaling through activation of Akt/protein kinase B: evidence that insulin stimulates vesicle docking/fusion but not intracellular mobility. J. Biol. Chem. *51*, 39719-39727.

Eyster, C. A., Duggins, Q. S. and Olson, A. L. (2005). Expression of constitutively active Akt/protein kinase B signals GLUT4 translocation in the absence of an intact actin cytoskeleton. J. Biol. Chem. *18*, 17978-17985.

Eyster, C. A. and Olson, A. L. (2009). Compartmentalization and regulation of insulin signaling to GLUT4 by the cytoskeleton. Vitam. Horm., 193-215.

Faire, K., Waterman-Storer, C. M., Gruber, D., Masson, D., Salmon, E. D. and Bulinski, J. C. (1999). E-MAP-115 (ensconsin) associates dynamically with microtubules in vivo and is not a physiological modulator of microtubule dynamics. J. Cell. Sci. *Pt 23*, 4243-4255.

Feeser, E. A., Ignacio, C. M., Krendel, M. and Ostap, E. M. (2010). Myo1e binds anionic phospholipids with high affinity. Biochemistry *43*, 9353-9360.

Ferguson, K. M., Lemmon, M. A., Schlessinger, J. and Sigler, P. B. (1995). Structure of the high affinity complex of inositol trisphosphate with a phospholipase C pleckstrin homology domain. Cell *6*, 1037-46.

Ferguson, K. M., Lemmon, M. A., Schlessinger, J. and Sigler, P. B. (1994). Crystal structure at 2.2 A resolution of the pleckstrin homology domain from human dynamin. Cell *2*, 199-209.

Fletcher, L. M., Welsh, G. I., Oatey, P. B. and Tavare, J. M. (2000). Role for the microtubule cytoskeleton in GLUT4 vesicle trafficking and in the regulation of insulin-stimulated glucose uptake. Biochem. J., 267-276.

Friedman, J. R., Webster, B. M., Mastronarde, D. N., Verhey, K. J. and Voeltz, G. K. (2010). ER sliding dynamics and ER-mitochondrial contacts occur on acetylated microtubules. J. Cell Biol. *3*, 363-375.

Fujita, H., Hatakeyama, H., Watanabe, T. M., Sato, M., Higuchi, H. and Kanzaki, M. (2010). Identification of three distinct functional sites of insulin-mediated GLUT4 trafficking in adipocytes using quantitative single molecule imaging. Mol. Biol. Cell *15*, 2721-2731.

Fulcher, F. K., Smith, B. T., Russ, M. and Patel, Y. M. (2008). Dual role for myosin II in GLUT4-mediated glucose uptake in 3T3-L1 adipocytes. Exp. Cell Res. *17*, 3264-3274.

Gambhir, A., Hangyas-Mihalyne, G., Zaitseva, I., Cafiso, D. S., Wang, J., Murray, D., Pentyala, S. N., Smith, S. O. and McLaughlin, S. (2004). Electrostatic sequestration of PIP2 on phospholipid membranes by basic/aromatic regions of proteins. Biophys J *4*, 2188-207.

Garza, L. A. and Birnbaum, M. J. (2000). Insulin-responsive aminopeptidase trafficking in 3T3-L1 adipocytes. J. Biol. Chem. *4*, 2560-2567.

Geeves, M. A., Fedorov, R. and Manstein, D. J. (2005). Molecular mechanism of actomyosin-based motility. Cell Mol Life Sci *13*, 1462-77.

Gifford, J. L., Walsh, M. P. and Vogel, H. J. (2007). Structures and metal-ion-binding properties of the Ca2+-binding helix-loop-helix EF-hand motifs. Biochem. J. *2*, 199-221.

Gonzalez, E. and McGraw, T. E. (2006). Insulin signaling diverges into Akt-dependent and -independent signals to regulate the recruitment/docking and the fusion of GLUT4 vesicles to the plasma membrane. Mol. Biol. Cell *10*, 4484-4493.

Guilherme, A., Emoto, M., Buxton, J. M., Bose, S., Sabini, R., Theurkauf, W. E., Leszyk, J. and Czech, M. P. (2000). Perinuclear localization and insulin responsiveness of GLUT4 requires cytoskeletal integrity in 3T3-L1 adipocytes. J. Biol. Chem. *49*, 38151-38159.

Hájková, Z., Bugajev, V., Dráberová, E., Vinopal, S., Dráberová, L., Janáček, J., Dráber, P. and Dráber, P. (2011). STIM1-Directed Reorganization of Microtubules in Activated Mast Cells. The Journal of Immunology *2*, 913-923.

Hayden, S. M., Wolenski, J. S. and Mooseker, M. S. (1990). Binding of brush border myosin I to phospholipid vesicles. J Cell Biol *2*, 443-51.

Hirono, M., Denis, C. S., Richardson, G. P. and Gillespie, P. G. (2004). Hair cells require phosphatidylinositol 4,5-bisphosphate for mechanical transduction and adaptation. Neuron *2*, 309-20.

Hokanson, D. E., Laakso, J. M., Lin, T., Sept, D. and Ostap, E. M. (2006). Myo1c binds phosphoinositides through a putative pleckstrin homology domain. Mol. Biol. Cell *11*, 4856-4865.

Hokanson, D. E. and Ostap, E. M. (2006). Myo1c binds tightly and specifically to phosphatidylinositol 4,5-bisphosphate and inositol 1,4,5-trisphosphate. Proc. Natl. Acad. Sci. U. S. A. *9*, 3118-3123.

Holman, G. D. and Cushman, S. W. (1994). Subcellular localization and trafficking of the GLUT4 glucose transporter isoform in insulin-responsive cells. Bioessays *10*, 753-759.

Holt, J. R., Gillespie, S. K., Provance, D. W., Shah, K., Shokat, K. M., Corey, D. P., Mercer, J. A. and Gillespie, P. G. (2002). A chemical-genetic strategy implicates myosin-1c in adaptation by hair cells. Cell *3*, 371-81.

Hou, J. C. and Pessin, J. E. (2007). Ins (endocytosis) and outs (exocytosis) of GLUT4 trafficking. Curr Opin Cell Biol *4*, 466-73.

Huang, J., Imamura, T., Babendure, J. L., Lu, J. C. and Olefsky, J. M. (2005). Disruption of microtubules ablates the specificity of insulin signaling to GLUT4 translocation in 3T3-L1 adipocytes. J. Biol. Chem. *51*, 42300-42306.

Huang, J., Imamura, T. and Olefsky, J. M. (2001). Insulin can regulate GLUT4 internalization by signaling to Rab5 and the motor protein dynein. Proc. Natl. Acad. Sci. U. S. A. *23*, 13084-13089.

Huang, S. and Czech, M. P. (2007). The GLUT4 glucose transporter. Cell Metab *4*, 237-52.

Huang, S., Lifshitz, L., Patki-Kamath, V., Tuft, R., Fogarty, K. and Czech, M. P. (2004). Phosphatidylinositol-4,5-bisphosphate-rich plasma membrane patches organize active zones of endocytosis and ruffling in cultured adipocytes. Mol Cell Biol *20*, 9102-23.

Huang, S., Lifshitz, L. M., Jones, C., Bellve, K. D., Standley, C., Fonseca, S., Corvera, S., Fogarty, K. E. and Czech, M. P. (2007). Insulin stimulates membrane fusion and GLUT4 accumulation in clathrin coats on adipocyte plasma membranes. Mol Cell Biol *9*, 3456-69.

Imamura, T., Huang, J., Usui, I., Satoh, H., Bever, J. and Olefsky, J. M. (2003). Insulin-induced GLUT4 translocation involves protein kinase C-lambda-mediated functional coupling between Rab4 and the motor protein kinesin. Mol. Cell. Biol. *14*, 4892-4900.

Inoue, M., Chang, L., Hwang, J., Chiang, S. H. and Saltiel, A. R. (2003). The exocyst complex is required for targeting of Glut4 to the plasma membrane by insulin. Nature *6932*, 629-633.

Insall, R. H. and Weiner, O. D. (2001). PIP3, PIP2, and cell movement--similar messages, different meanings?. Dev Cell *6*, 743-7.

Ishikura, S. and Klip, A. (2008). Muscle cells engage Rab8A and myosin Vb in insulin-dependent GLUT4 translocation. Am. J. Physiol. Cell. Physiol. *4*, C1016-25.

James, D. E., Brown, R., Navarro, J. and Pilch, P. F. (1988). Insulin-regulatable tissues express a unique insulin-sensitive glucose transport protein. Nature *6169*, 183-185.

James, D. E., Strube, M. and Mueckler, M. (1989). Molecular cloning and characterization of an insulin-regulatable glucose transporter. Nature *6210*, 83-87.

Jedrychowski, M. P., Gartner, C. A., Gygi, S. P., Zhou, L., Herz, J., Kandror, K. V. and Pilch, P. F. (2010). Proteomic Analysis of GLUT4 Storage Vesicles Reveals LRP1 to Be an Important Vesicle Component and Target of Insulin Signaling. Journal of Biological Chemistry *1*, 104-114.

Jhun, B. H., Rampal, A. L., Liu, H., Lachaal, M. and Jung, C. Y. (1992). Effects of insulin on steady state kinetics of GLUT4 subcellular distribution in rat adipocytes. Evidence of constitutive GLUT4 recycling. J. Biol. Chem. *25*, 17710-17715.

Jiang, L., Fan, J., Bai, L., Wang, Y., Chen, Y., Yang, L., Chen, L. and Xu, T. (2008). Direct quantification of fusion rate reveals a distal role for AS160 in insulin-stimulated fusion of GLUT4 storage vesicles. J. Biol. Chem. *13*, 8508-8516.

Jiang, Z. Y., Chawla, A., Bose, A., Way, M. and Czech, M. P. (2002). A Phosphatidylinositol 3-Kinase-independent Insulin Signaling Pathway to N-WASP/Arp2/3/F-actin Required for GLUT4 Glucose Transporter Recycling. Journal of Biological Chemistry *1*, 509-515.

Jolly, A. L., Kim, H., Srinivasan, D., Lakonishok, M., Larson, A. G. and Gelfand, V. I. (2010). Kinesin-1 heavy chain mediates microtubule sliding to drive changes in cell shape. Proc. Natl. Acad. Sci. U. S. A. *27*, 12151-12156.

Jontes, J. D., Ostap, E. M., Pollard, T. D. and Milligan, R. A. (1998). Three-dimensional structure of Acanthamoeba castellanii myosin-IB (MIB) determined by cryoelectron microscopy of decorated actin filaments. J Cell Biol *1*, 155-62.

Jontes, J. D. and Milligan, R. A. (1997). Brush Border Myosin–I Structure and ADP-dependent Conformational Changes Revealed by Cryoelectron Microscopy and Image Analysis. The Journal of Cell Biology *3*, 683-693.

Kandror, K. V. and Pilch, P. F. (1994). Gp160, a Tissue-Specific Marker for Insulin-Activated Glucose Transport. Proc. Natl. Acad. Sci. U. S. A. *17*, 8017-8021.

Kanzaki, M. and Pessin, J. E. (2001). Insulin-stimulated GLUT4 translocation in adipocytes is dependent upon cortical actin remodeling. J Biol Chem *45*, 42436-44.

Kanzaki, M., Watson, R. T., Hou, J. C., Stamnes, M., Saltiel, A. R. and Pessin, J. E. (2002). Small GTP-binding protein TC10 differentially regulates two distinct populations of filamentous actin in 3T3L1 adipocytes. Mol Biol Cell *7*, 2334-46.

Karylowski, O., Zeigerer, A., Cohen, A. and McGraw, T. E. (2004). GLUT4 is retained by an intracellular cycle of vesicle formation and fusion with endosomes. Mol. Biol. Cell *2*, 870-882.

Khandani, A., Eng, E., Jongstra-Bilen, J., Schreiber, A. D., Douda, D., Samavarchi-Tehrani, P. and Harrison, R. E. (2007). Microtubules regulate PI-3K activity and recruitment to the phagocytic cup during Fcgamma receptor-mediated phagocytosis in nonelicited macrophages. J. Leukoc. Biol. *2*, 417-428.

Kiehart, D. P., Kaiser, D. A. and Pollard, T. D. (1984). Direct localization of monoclonal antibody-binding sites on Acanthamoeba myosin-II and inhibition of filament formation by antibodies that bind to specific sites on the myosin-II tail. The Journal of Cell Biology *3*, 1015-1023.

Kinsella, B. T., Erdman, R. A. and Maltese, W. A. (1991). Carboxyl-terminal isoprenylation of ras-related GTP-binding proteins encoded by rac1, rac2, and ralA. Journal of Biological Chemistry *15*, 9786-9794.

Kolsch, V., Charest, P. G. and Firtel, R. A. (2008). The regulation of cell motility and chemotaxis by phospholipid signaling. J Cell Sci *Pt 5*, 551-9.

Komaba, S. and Coluccio, L. M. (2010). Localization of Myosin 1b to Actin Protrusions Requires Phosphoinositide Binding. Journal of Biological Chemistry *36*, 27686-27693.

Kramer, H. F., Witczak, C. A., Taylor, E. B., Fujii, N., Hirshman, M. F. and Goodyear, L. J. (2006). AS160 Regulates Insulin- and Contraction-stimulated Glucose Uptake in Mouse Skeletal Muscle. Journal of Biological Chemistry *42*, 31478-31485.

Kupriyanova, T. A. and Kandror, K. V. (2000). Cellugyrin Is a Marker for a Distinct Population of Intracellular Glut4-containing Vesicles. Journal of Biological Chemistry *46*, 36263-36268.

Kupriyanova, T. A., Kandror, V. and Kandror, K. V. (2002). Isolation and Characterization of the Two Major Intracellular Glut4 Storage Compartments. Journal of Biological Chemistry *11*, 9133-9138.

Laakso, J. M., Lewis, J. H., Shuman, H. and Ostap, E. M. (2008). Myosin I can act as a molecular force sensor. Science *5885*, 133-136.

Laakso, J. M., Lewis, J. H., Shuman, H. and Ostap, E. M. (2010). Control of myosin-I force sensing by alternative splicing. Proceedings of the National Academy of Sciences *2*, 698-702.

Lakowicz, J. R. (1999). Principles of Fluorescence Spectroscopy, New York: Kluwer Academic/Plenum Publishers.

Lalioti, V. S., Vergarajauregui, S., Tsuchiya, Y., Hernandez-Tiedra, S. and Sandoval, I. V. (2009). Daxx functions as a scaffold of a protein assembly constituted by GLUT4, JNK1 and KIF5B. J. Cell. Physiol. *2*, 416-426.

Larance, M. *et al.* (2005). Characterization of the role of the Rab GTPase-activating protein AS160 in insulin-regulated GLUT4 trafficking. J Biol Chem *45*, 37803-13.

Lauritzen, H. P. M. M., Galbo, H., Brandauer, J., Goodyear, L. J. and Ploug, T. (February 2008). Large GLUT4 Vesicles Are Stationary While Locally and Reversibly Depleted During Transient Insulin Stimulation of Skeletal Muscle of Living Mice. Diabetes *2*, 315-324.

Laux, T., Fukami, K., Thelen, M., Golub, T., Frey, D. and Caroni, P. (2000). GAP43, MARCKS, and CAP23 modulate PI(4,5)P(2) at plasmalemmal rafts, and regulate cell cortex actin dynamics through a common mechanism. J Cell Biol *7*, 1455-72.

Lemmon, M. A. and Ferguson, K. M. (2001). Molecular determinants in pleckstrin homology domains that allow specific recognition of phosphoinositides. Biochem Soc Trans *Pt 4*, 377-84.

Lemmon, M. A., Ferguson, K. M., O'Brien, R., Sigler, P. B. and Schlessinger, J. (1995). Specific and high-affinity binding of inositol phosphates to an isolated pleckstrin homology domain. Proc Natl Acad Sci U S A *23*, 10472-6.

Leventis, P. A. and Grinstein, S. (2010). The distribution and function of phosphatidylserine in cellular membranes. Annu. Rev. Biophys., 407-427.

Lewis, J. H., Lin, T., Hokanson, D. E. and Ostap, E. M. (2006). Temperature dependence of nucleotide association and kinetic characterization of myo1b. Biochemistry *38*, 11589-11597.

Lin, B., Pilch, P. F. and Kandror, K. V. (1997). Sortilin Is a Major Protein Component of Glut4-containing Vesicles. Journal of Biological Chemistry *39*, 24145-24147.

Liu, L. B., Omata, W., Kojima, I. and Shibata, H. (2003). Insulin recruits GLUT4 from distinct compartments via distinct traffic pathways with differential microtubule dependence in rat adipocytes. J. Biol. Chem. *32*, 30157-30169.

Livingstone, C., James, D. E., Rice, J. E., Hanpeter, D. and Gould, G. W. (1996). Compartment ablation analysis of the insulin-responsive glucose transporter (GLUT4) in 3T3-L1 adipocytes. Biochem. J. *Pt 2*, 487-495.

Lizunov, V. A., Matsumoto, H., Zimmerberg, J., Cushman, S. W. and Frolov, V. A. (2005). Insulin stimulates the halting, tethering, and fusion of mobile GLUT4 vesicles in rat adipose cells. J. Cell Biol. *3*, 481-489.

Lizunov, V. A., Lisinski, I., Stenkula, K., Zimmerberg, J. and Cushman, S. W. (2009). Insulin Regulates Fusion of GLUT4 Vesicles Independent of Exo70-mediated Tethering. Journal of Biological Chemistry *12*, 7914-7919.

Lopez, J. A., Burchfield, J. G., Blair, D. H., Mele, K., Ng, Y., Vallotton, P., James, D. E. and Hughes, W. E. (2009). Identification of a distal GLUT4 trafficking event controlled by actin polymerization. Mol. Biol. Cell *17*, 3918-3929.

Lu, Y. and Nelsestuen, G. L. (1996). Dynamic features of prothrombin interaction with phospholipid vesicles of different size and composition: implications for protein--membrane contact. Biochemistry *25*, 8193-200.

Macia, E., Paris, S. and Chabre, M. (2000). Binding of the PH and polybasic C-terminal domains of ARNO to phosphoinositides and to acidic lipids. Biochemistry *19*, 5893-901.

Malide, D., Ramm, G., Cushman, S. W. and Slot, J. W. (2000). Immunoelectron microscopic evidence that GLUT4 translocation explains the stimulation of glucose transport in isolated rat white adipose cells. J Cell Sci, 4203-10.

Malide, D., St-Denis, J., Keller, S. R. and Cushman, S. W. (1997). Vp165 and GLUT4 share similar vesicle pools along their trafficking pathways in rat adipose cells. FEBS Lett. *3*, 461-468.

Manceva, S., Lin, T., Pham, H., Lewis, J. H., Goldman, Y. E. and Ostap, E. M. (2007). Calcium regulation of calmodulin binding to and dissociation from the myo1c regulatory domain. Biochemistry *42*, 11718-11726.

Martin, S., Rice, J. E., Gould, G. W., Keller, S. R., Slot, J. W. and James, D. E. (1997). The glucose transporter GLUT4 and the aminopeptidase vp165 colocalise in tubulo-vesicular elements in adipocytes and cardiomyocytes. J. Cell. Sci. *Pt 18*, 2281-2291.

Martin, S., Tellam, J., Livingstone, C., Slot, J. W., Gould, G. W. and James, D. E. (1996). The glucose transporter (GLUT-4) and vesicle-associated membrane protein-2 (VAMP-2) are segregated from recycling endosomes in insulin-sensitive cells. J. Cell Biol. *3*, 625-635.

McLaughlin, S. and Murray, D. (2005). Plasma membrane phosphoinositide organization by protein electrostatics. Nature *7068*, 605-11.

McLaughlin, S., Wang, J., Gambhir, A. and Murray, D. (2002). PIP(2) and proteins: interactions, organization, and information flow. Annu. Rev. Biophys. Biomol. Struct., 151-175.

Meijering, E., Jacob, M., Sarria, J. C., Steiner, P., Hirling, H. and Unser, M. (2004). Design and validation of a tool for neurite tracing and analysis in fluorescence microscopy images. Cytometry A. *2*, 167-176.

Mentlik, A. N., Sanborn, K. B., Holzbaur, E. L. and Orange, J. S. (2010). Rapid Lytic Granule Convergence to the MTOC in Natural Killer Cells Is Dependent on Dynein But Not Cytolytic Commitment. Molecular Biology of the Cell *13*, 2241-2256.

Miesenbock, G., De Angelis, D. A. and Rothman, J. E. (1998). Visualizing secretion and synaptic transmission with pH-sensitive green fluorescent proteins. Nature *6689*, 192-195.

Miinea, C. P., Sano, H., Kane, S., Sano, E., Fukuda, M., Peranen, J., Lane, W. S. and Lienhard, G. E. (2005). AS160, the Akt substrate regulating GLUT4 translocation, has a functional Rab GTPase-activating protein domain. Biochem. J. *Pt 1*, 87-93.

Miyata, H., Bowers, B. and Korn, E. D. (1989). Plasma membrane association of Acanthamoeba myosin I. J Cell Biol *4 Pt 1*, 1519-28.

Molero, J. C., Whitehead, J. P., Meerloo, T. and James, D. E. (2001). Nocodazole inhibits insulin-stimulated glucose transport in 3T3-L1 adipocytes via a microtubule-independent mechanism. J. Biol. Chem. *47*, 43829-43835.

Mooseker, M. S. and Cheney, R. E. (1995). Unconventional myosins. Annu Rev Cell Dev Biol, 633-75.

Mueckler, M., Caruso, C., Baldwin, S. A., Panico, M., Blench, I., Morris, H. R., Allard, W. J., Lienhard, G. E. and Lodish, H. F. (1985). Sequence and structure of a human glucose transporter. Science *4717*, 941-945.

Nakamori, Y., Emoto, M., Fukuda, N., Taguchi, A., Okuya, S., Tajiri, M., Miyagishi, M., Taira, K., Wada, Y. and Tanizawa, Y. (2006). Myosin motor Myo1c and its receptor NEMO/IKK-gamma promote TNF-alpha-induced serine307 phosphorylation of IRS-1. J Cell Biol *5*, 665-71.

Novak, K. D., Peterson, M. D., Reedy, M. C. and Titus, M. A. (1995). Dictyostelium myosin I double mutants exhibit conditional defects in pinocytosis. J Cell Biol *5*, 1205-21.

Ohki, S., Ikura, M. and Zhang, M. (1997). Identification of Mg2+-binding sites and the role of Mg2+ on target recognition by calmodulin. Biochemistry *14*, 4309-4316.

Olety, B., Walte, M., Honnert, U., Schillers, H. and Bahler, M. (2010). Myosin 1G (Myo1G) is a haematopoietic specific myosin that localises to the plasma membrane and regulates cell elasticity. FEBS Lett. *3*, 493-499.

Olson, A. L., Eyster, C. A., Duggins, Q. S. and Knight, J. B. (2003). Insulin promotes formation of polymerized microtubules by a phosphatidylinositol 3-kinase-independent, actin-dependent pathway in 3T3-L1 adipocytes. Endocrinology *11*, 5030-5039.

Patino-Lopez, G., Aravind, L., Dong, X., Kruhlak, M. J., Ostap, E. M. and Shaw, S. (2010). Myosin 1G Is an Abundant Class I Myosin in Lymphocytes Whose Localization

at the Plasma Membrane Depends on Its Ancient Divergent Pleckstrin Homology (PH) Domain (Myo1PH). Journal of Biological Chemistry *12*, 8675-8686.

Phillips, K. R., Tong, S., Goodyear, R., Richardson, G. P. and Cyr, J. L. (2006). Stereociliary myosin-1c receptors are sensitive to calcium chelation and absent from cadherin 23 mutant mice. J Neurosci *42*, 10777-88.

Pyrpassopoulos, S., Shuman, H. and Ostap, E. M. (2010). Single-Molecule Adhesion Forces and Attachment Lifetimes of Myosin-I Phosphoinositide Interactions. Biophys. J. *12*, 3916-3922.

Quintyne, N. J., Gill, S. R., Eckley, D. M., Crego, C. L., Compton, D. A. and Schroer, T. A. (1999). Dynactin is required for microtubule anchoring at centrosomes. J. Cell Biol. *2*, 321-334.

Rayment, I., Holden, H. M., Whittaker, M., Yohn, C. B., Lorenz, M., Holmes, K. C. and Milligan, R. A. (1993). Structure of the actin-myosin complex and its implications for muscle contraction. Science *5117*, 58-65.

Ross, J. L., Shuman, H., Holzbaur, E. L. and Goldman, Y. E. (2008). Kinesin and dynein-dynactin at intersecting microtubules: motor density affects dynein function. Biophys J *8*, 3115-25.

Ross, S. A., Scott, H. M., Morris, N. J., Leung, W. Y., Mao, F., Lienhard, G. E. and Keller, S. R. (1996). Characterization of the insulin-regulated membrane aminopeptidase in 3T3-L1 adipocytes. J. Biol. Chem. *6*, 3328-3332.

Rothwarf, D. M., Zandi, E., Natoli, G. and Karin, M. (1998). IKK-gamma is an essential regulatory subunit of the IkappaB kinase complex. Nature *6699*, 297-300.

Ruppert, C., Godel, J., Muller, R. T., Kroschewski, R., Reinhard, J. and Bahler, M. (1995). Localization of the rat myosin I molecules myr 1 and myr 2 and in vivo targeting of their tail domains. J Cell Sci, 3775-86.

Satoh, S., Nishimura, H., Clark, A. E., Kozka, I. J., Vannucci, S. J., Simpson, I. A., Quon, M. J., Cushman, S. W. and Holman, G. D. (1993). Use of bismannose photolabel to elucidate insulin-regulated GLUT4 subcellular trafficking kinetics in rat adipose cells. Evidence that exocytosis is a critical site of hormone action. J. Biol. Chem. *24*, 17820-17829.

Semiz, S., Park, J. G., Nicoloro, S. M., Furcinitti, P., Zhang, C., Chawla, A., Leszyk, J. and Czech, M. P. (2003). Conventional kinesin KIF5B mediates insulin-stimulated GLUT4 movements on microtubules. EMBO J *10*, 2387-99.

Shaner, N. C., Campbell, R. E., Steinbach, P. A., Giepmans, B. N., Palmer, A. E. and Tsien, R. Y. (2004). Improved monomeric red, orange and yellow fluorescent proteins derived from Discosoma sp. red fluorescent protein. Nat. Biotechnol. *12*, 1567-1572.

Sherr, E. H., Joyce, M. P. and Greene, L. A. (1993). Mammalian myosin I alpha, I beta, and I gamma: new widely expressed genes of the myosin I family. J. Cell Biol. *6*, 1405-1416.

Shi, J., Huang, G. and Kandror, K. V. (2008). Self-assembly of Glut4 Storage Vesicles during Differentiation of 3T3-L1 Adipocytes. Journal of Biological Chemistry *44*, 30311-30321.

Shigematsu, S., Khan, A. H., Kanzaki, M. and Pessin, J. E. (2002). Intracellular insulin-responsive glucose transporter (GLUT4) distribution but not insulin-stimulated GLUT4 exocytosis and recycling are microtubule dependent. Mol Endocrinol *5*, 1060-8.

Siemens, J., Lillo, C., Dumont, R. A., Reynolds, A., Williams, D. S., Gillespie, P. G. and Muller, U. (2004). Cadherin 23 is a component of the tip link in hair-cell stereocilia. Nature *6986*, 950-5.

Slot, J. W., Geuze, H. J., Gigengack, S., Lienhard, G. E. and James, D. E. (1991). Immuno-localization of the insulin regulatable glucose transporter in brown adipose tissue of the rat. J. Cell Biol. *1*, 123-135.

Sokac, A. M., Schietroma, C., Gundersen, C. B. and Bement, W. M. (2006). Myosin-1c couples assembling actin to membranes to drive compensatory endocytosis. Dev Cell *5*, 629-40.

Steimle, P. A., Fulcher, F. K. and Patel, Y. M. (2005). A novel role for myosin II in insulin-stimulated glucose uptake in 3T3-L1 adipocytes. Biochem. Biophys. Res. Commun. *4*, 1560-1565.

Sumitani, S., Ramlal, T., Somwar, R., Keller, S. R. and Klip, A. (1997). Insulin Regulation and Selective Segregation with Glucose Transporter-4 of the Membrane Aminopeptidase vp165 in Rat Skeletal Muscle Cells. Endocrinology *3*, 1029-1034.

Sun, Y., McKenna, J. D., Murray, J. M., Ostap, E. M. and Goldman, Y. E. (2009). Parallax: high accuracy three-dimensional single molecule tracking using split images. Nano Lett. *7*, 2676-2682.

Suzuki, K. and Kono, T. (1980). Evidence that insulin causes translocation of glucose transport activity to the plasma membrane from an intracellular storage site. Proc. Natl. Acad. Sci. U. S. A. *5*, 2542-2545.

Swanljung-Collins, H. and Collins, J. H. (1994). Brush border myosin I has a calmodulin/phosphatidylserine switch and tail actin-binding. Adv Exp Med Biol, 205-13.

T., B. J.,Jr, Berkemeier, B. A. and Elmendorf, J. S. (2007). "Actin"g on GLUT4: membrane & cytoskeletal components of insulin action. Curr Diabetes Rev *2*, 111-22.

Tang, N., Lin, T. and Ostap, E. M. (2002). Dynamics of myo1c (myosin-ibeta) lipid binding and dissociation. J. Biol. Chem. *45*, 42763-42768.

Tang, N., Lin, T., Yang, J., Foskett, J. K. and Ostap, E. M. (2007). CIB1 and CaBP1 bind to the myo1c regulatory domain. J. Muscle Res. Cell. Motil. *6*, 285-291.

Tang, N. and Ostap, E. M. (2001). Motor domain-dependent localization of myo1b (myr-1). Curr. Biol. *14*, 1131-1135.

Tegethoff, S., Behlke, J. and Scheidereit, C. (2003). Tetrameric oligomerization of IkappaB kinase gamma (IKKgamma) is obligatory for IKK complex activity and NF-kappaB activation. Mol. Cell. Biol. *6*, 2029-2041.

Tengholm, A., Teruel, M. N. and Meyer, T. (2003). Single cell imaging of PI3K activity and glucose transporter insertion into the plasma membrane by dual color evanescent wave microscopy. Sci. STKE *169*, PL4.

TerBush, D. R., Maurice, T., Roth, D. and Novick, P. (1996). The Exocyst is a multiprotein complex required for exocytosis in Saccharomyces cerevisiae. EMBO J. *23*, 6483-6494.

TerBush, D. R. and Novick, P. (1995). Sec6, Sec8, and Sec15 are components of a multisubunit complex which localizes to small bud tips in Saccharomyces cerevisiae. J. Cell Biol. *2*, 299-312.

Thurmond, D. C. and Pessin, J. E. (2001). Molecular machinery involved in the insulin-regulated fusion of GLUT4-containing vesicles with the plasma membrane (review). Mol Membr Biol *4*, 237-45.

Toner, M., Vaio, G., McLaughlin, A. and McLaughlin, S. (1988). Adsorption of cations to phosphatidylinositol 4,5-bisphosphate. Biochemistry *19*, 7435-43.

Tong, P., Khayat, Z. A., Huang, C., Patel, N., Ueyama, A. and Klip, A. (2001). Insulin-induced cortical actin remodeling promotes GLUT4 insertion at muscle cell membrane ruffles. J. Clin. Invest. *3*, 371-381.

Toyoda, T., An, D., Witczak, C. A., Koh, H. J., Hirshman, M. F., Fujii, N. and Goodyear, L. J. (2011). Myo1c regulates glucose uptake in mouse skeletal muscle. J. Biol. Chem. *6*, 4133-4140.

Tsakiridis, T., Vranic, M. and Klip, A. (1994). Disassembly of the actin network inhibits insulin-dependent stimulation of glucose transport and prevents recruitment of glucose transporters to the plasma membrane. Journal of Biological Chemistry *47*, 29934-29942.

Tyska, M. J. and Mooseker, M. S. (2004). A role for myosin-1A in the localization of a brush border disaccharidase. J Cell Biol *3*, 395-405.

Uyeda, T. Q., Kron, S. J. and Spudich, J. A. (1990). Myosin step size. Estimation from slow sliding movement of actin over low densities of heavy meromyosin. J Mol Biol *3*, 699-710.

Veigel, C., Coluccio, L. M., Jontes, J. D., Sparrow, J. C., Milligan, R. A. and Molloy, J. E. (1999). The motor protein myosin-I produces its working stroke in two steps. Nature *6727*, 530-3.

Voigt, H., Olivo, J. C., Sansonetti, P. and Guillen, N. (1999). Myosin IB from Entamoeba histolytica is involved in phagocytosis of human erythrocytes. J. Cell. Sci. *Pt 8*, 1191-1201.

Watson, R. T. and Pessin, J. E. (2007). GLUT4 translocation: the last 200 nanometers. Cell Signal *11*, 2209-17.

Watson, R. T. and Pessin, J. E. (2006). Bridging the GAP between insulin signaling and GLUT4 translocation. Trends Biochem Sci *4*, 215-22.

Yang, J. and Holman, G. D. (1993). Comparison of GLUT4 and GLUT1 subcellular trafficking in basal and insulin-stimulated 3T3-L1 cells. J. Biol. Chem. *7*, 4600-4603.

Yin, H. L. and Janmey, P. A. (2003). Phosphoinositide regulation of the actin cytoskeleton. Annu Rev Physiol, 761-89.

Yip, M. F., Ramm, G., Larance, M., Hoehn, K. L., Wagner, M. C., Guilhaus, M. and James, D. E. (2008). CaMKII-mediated phosphorylation of the myosin motor Myo1c is required for insulin-stimulated GLUT4 translocation in adipocytes. Cell. Metab. *5*, 384-398.

Yoshizaki, T., Imamura, T., Babendure, J. L., Lu, J. C., Sonoda, N. and Olefsky, J. M. (2007). Myosin 5a is an insulin-stimulated Akt2 (protein kinase Bbeta) substrate modulating GLUT4 vesicle translocation. Mol Cell Biol *14*, 5172-83.

Zaid, H., Antonescu, C. N., Randhawa, V. K. and Klip, A. (2008). Insulin action on glucose transporters through molecular switches, tracks and tethers. Biochem. J. *2*, 201-215.

Zeigerer, A., Lampson, M. A., Karylowski, O., Sabatini, D. D., Adesnik, M., Ren, M. and McGraw, T. E. (2002). GLUT4 retention in adipocytes requires two intracellular insulin-regulated transport steps. Mol. Biol. Cell *7*, 2421-2435.

Zerial, M. and McBride, H. (2001). Rab proteins as membrane organizers. Nat. Rev. Mol. Cell Biol. *2*, 107-117.